ABSTRACT

DESAI, PRAGNASHRI SUDHIRBHAI. An Analytical Method to Evaluate Laminar Convective Heating Rates for Paraboloids with Perfect Gas Chemistry. (Under the direction of Dr. Fred R. DeJarnette).

The design of a hypersonic vehicle requires a detailed study of the surrounding aerodynamic heating environment. In a high speed flow, the flow interacting with the surface comes to rest as it passes over the vehicle due to viscosity effects. This results in kinetic to thermal energy conversion and extremely large temperatures at the surface. Thus, one of the most critical design criteria for a spacecraft is to survive the surface heating rates imparted on the vehicle during the atmospheric re-entry phase of the mission. Currently, there exist Navier-Stokes based computational fluid dynamics (CFD) codes and experimental analysis as ways to examine and predict the flow properties including surface heating rates. Ground experimental testing cannot simultaneously simulate characteristics of a hypersonic flowfield, thus requiring the usage of CFD codes to generate numerical approximations. These complex CFD methods involve significant run times, and therefore are not cost effective during the early phases of design when numerous combinations of trajectories and geometries are tested. It is necessary to establish and utilize an approximate method that can provide both accuracy and efficiency when evaluating aerothermodynamic properties during the preliminary stage of design.

The researcher was assigned to develop an analytical method to determine the surface heating distribution over a body in hypersonic flow. A set of correlations are derived in this research to evaluate the laminar convective heating rate at any location on the surface of a parabolic-shaped geometry for an ideal gas model. The surface heating rates are non-dimensionalized by the stagnation point heating rate, where maximum heating occurs, to simplify the relations.

The accuracy of this newly developed approach is validated using approximate engineering codes BLUNT2D and SABLE for a set of freestream conditions. Additionally, a fourth order polynomial curve fit equation is generated based on the results of the analytical method. Results from both the analytical correlations and the curve fit are valid within 15% error accuracy for velocities of 10,000 ft/s to 26,000 ft/s, altitudes ranging from 150,000 ft to 250,000 ft, and nose radius lengths between 0.5 ft and 10 ft. This approach is deemed as a valuable tool to rapidly generate aerothermodynamic conditions during the early stages of a hypersonic vehicle design.

An Analytical Method to Evaluate Laminar Convective Heating Rates for Paraboloids with Perfect Gas Chemistry

by
Pragnashri Sudhirbhai Desai

A thesis submitted to the Graduate Faculty of
North Carolina State University
in partial fulfillment of the
requirements for the degree of
Master of Science

Aerospace Engineering

Raleigh, North Carolina

2014

APPROVED BY:

_____	_____
Dr. Andre Mazzoleni	Dr. Ashok Gopalarathnam

_____
Dr. Fred R. DeJarnette
Committee Chair

Dedication

Dedicated to my lovely parents, Hema and Sudhir Desai, for providing me with love and endless support to reach my dreams. Also dedicated to my wonderful brother, Harsh Desai, whose brilliance I aspire to achieve one day. Thank you for always encouraging me.

Biography

Pragnashri Sudhirbhai Desai was born in Baroda, Gujarat, India on May 5th, 1990. All of her family and friends refer to her as Payal. She was raised in India until the age of 9, when her family immigrated to the United States. Since moving to the US, her family has lived in Charlotte, North Carolina. After graduating from Myers Park High School in 2007, Payal attended North Carolina State University. During her undergraduate career, she majored in aerospace engineering and pursued two minors: art & design and Hindi. Along with her interests in math and science, Payal is fascinated with anything art related (drawing, painting, photography, etc.). She also enjoys cooking, exercising, and spending time with her dear family.

During her senior year of high school, Payal had the opportunity to participate in an engineering internship. The internship exposed her to many different engineering fields. She became particularly interested in aerospace engineering when she visited Charlotte Douglas International Airport to speak to aerospace and mechanical engineers. This led her to apply and attend NC State University to pursue her aerospace engineering degree. She completed an undergraduate research project in the field of aerothermodynamics during her last year of undergraduate studies with Dr. Fred DeJarnette, who encouraged her to enroll in the master's program within the Mechanical and Aerospace Engineering department at NC State.

Currently, Payal is working on her master's degree under the direction of Dr. DeJarnette. While working on her master's degree, Payal interned at Applied Research Associates as a weapons effects engineer. After completing her Masters of Science in Aerospace Engineering, she will work for a company focusing on hypersonic flow and space systems research. She also hopes to teach calculus at the high school level in the future, encouraging students (particularly women) to pursue careers in STEM fields.

Acknowledgements

I would like to acknowledge and extend appreciation to my advisor and mentor Dr. Fred R. DeJarnette for his immense guidance throughout my graduate research project. His enthusiasm towards the field of aerospace, and particularly aerothermodynamics, has been very inspiring. Dr. DeJarnette served as the chairman of my advisory committee. I would also like to thank two of my other committee members, Dr. Ashok Gopalarathnam and Dr. Andre Mazzoleni, who have been very helpful and sincere during this entire process.

Additionally, I would like to express my deepest appreciation to H. Harris Hamilton at the Aerothermodynamics branch at the NASA Langley Research Center. Mr. Hamilton's expert guidance served to make this research and investigation a success.

Table of Contents

List of Tables

List of Figures

Nomenclature

a	parameter used to describe ogive geometry, *ft*
alt	altitude, *ft*
c_p	specific heat at constant pressure, *(ft·lb)/(slugs·°R)*
h	enthalpy per unit mass of mixture, *(ft·lb)/slugs*
k	coefficient for body, *dimensionless*
l	reference length, *ft*
Le	Lewis number, *dimensionless*
M	Mach number, *dimensionless*
p	pressure, *lb/ft^2*
Pr	Prandtl number, *dimensionless*
$\dot{q}_w$	heat transfer rate per unit area, *BTU/(ft^2·s)*
$\mathbb{R}$	specific gas constant, *(ft·lb)/(slugs·°R)*
R_o *(or* R_n*)*	nose radius, *ft*
s	distance along the surface of the body (measured from the forward stagnation point), *ft*
s'	distance along the surface of a cone (measured from the tip of equivalent sharp cone), *ft*
T	temperature, *°R*
u	velocity in x-direction, *ft/s*
V	total velocity, *ft/s*
V_{sound}	speed of sound, *ft/s*
x	distance from the leading edge, *ft*
x_T	distance from transition point, *ft*
α	angle of attack, *degrees*
γ	heat capacity ratio, *dimensionless*

μ	viscosity, *(lb·s)/ft^2*
ρ	density, *slugs/ft^3*
θ	angle between line tangential to the surface and the radius vector, *degrees*
θ_c	cone half angle, *degrees*

Subscripts

D	diffusion
e	at the edge of the boundary layer
SL	at sea-level
w	at the wall
∞	freestream condition
0	stagnation point
2	behind the shock wave

Superscripts

'	behind the shock wave

Chapter 1

Introduction

Aerodynamic heating can be described as the heating of a solid body due to the passage of fluid over the surface of the body. The prediction of aerodynamic heating on trans-atmospheric vehicles traveling at supersonic and hypersonic speeds is of particular interest in the field of aerodynamics. This section of aerodynamics is known as aerothermodynamics. As the hypersonic flow passes over the surface of a vehicle, the flow interacting with the surface comes to rest due to viscosity effects. This decrease in velocity causes kinetic energy to be converted into thermal energy, resulting in an increase in the temperature of the air. Heat is transferred from the air onto the surface of the vehicle. With high speed flows, the effects of energy conversion and temperature rise at the surface can become extremely large.

Thus, the design of hypersonic vehicles must account for the aerodynamic heating environment, which can be determined by simultaneous solution of the continuity equation, momentum equation, and the energy equation. Hypersonic vehicles have been designed and constructed by engineers and scientists since the 1950's. Many of the designs over the years have revealed issues that were not predicted through flight tests or computational analysis. These problems present very unique challenges for the designers working on hypersonic vehicles. One of the most critical design criteria requires the spacecraft to survive the surface heating rates that are caused due to the hypersonic environment during atmospheric re-entry[1]. A Thermal Protection System (TPS) has to be implemented to survive these conditions. The TPS operates as an effective insulator to protect the surface of the spacecraft during

atmospheric re-entry heating caused by compression of the air ahead of the hypersonic vehicle. The TPS shields the outer layer of the spacecraft from searing through the extreme temperatures experienced due to aerodynamic heating. The protection system must remain intact during all phases of the flight and sustain the loads imposed during the ascending and descending phases of the flight[2].

On February 1st, 2003, the disaster of the Space Shuttle Columbia occurred during re-entry due to the failure of the TPS. After investigation, it was concluded that the Space Shuttle disintegrated as a result of a piece of foam damaging a Reinforced Carbon-Carbon material on the leading edge of left wing during launch, allowing hot gases to enter the wing structure during re-entry. This led to the destruction of the Space Shuttle and the death of all seven crew members. This accident proves the importance of developing a TPS that can withstand the severe aerothermodynamic environment experienced by hypersonic vehicles during flight.

In Bertin's *Hypersonic Aerothermodynamics*, emphasis is placed on both the numerical methods in forms of computational fluid dynamics (CFD) and experimental analysis as ways to examine and study hypersonic flow. Experimental programs were relied on heavily when hypersonic vehicles were first being developed in the 1950's. However, since experimental programs could only model partial simulations of the hypersonic environment, computational methods based on theoretical models and empirical correlations were being utilized more and more over time. By the 1990's, researchers based considerable reliance on computational methods to predict the aerothermodynamic environment [1]. Flight testing and ground testing cannot simulate various characteristics of an aerothermodynamics atmosphere simultaneously, thus requiring the usage of CFD codes to generate numerical approximations. These computational solutions evaluate flowfields and heating rates using Navier-Stokes based solvers. While they generate the most accurate solutions, these CFD codes require a substantial amount of run-time. These complex solvers are, thus, not cost

effective when running hundreds or thousands of simulations during the conceptual phase of the design process. Although Navier-Stokes solvers can assist with the design analysis stage, it is necessary to develop approximate methods that can provide both accuracy and efficiency when evaluating properties of an aerothermodynamic environment.

1.1 Research Objectives

Lester Lees published an article in the *Journal of Jet Propulsion* in 1956 regarding heat transfer rates over blunt-nosed bodies in hypersonic flow. Within this publication, he derives mathematical correlations to describe the laminar convective heating distribution over various blunt-nosed bodies in hypersonic flowfields, including a hemisphere and a sphere cone. Perfect gas chemistry is assumed within his derivations[3]. The objective of this research is to develop a correlation that describes the heating distribution over an ogive shaped parabolic curve using the concepts presented by Lees.

Additionally, the accuracy of these newly developed relations will be validated using approximate engineering codes[4]. The codes will compare the correlations for a perfect gas chemistry model. The results of this research will enable scientists and engineers to use a more simplified analytical method than CFD or approximate engineering codes during the early phase of the design when considering a parabolic shaped geometry in a hypersonic flowfield. The utilization of the analytical method will significantly reduce both computational cost and time.

1.2 Laminar Convective Heating Relations for Parabolic Curved Blunt-Nosed Bodies

This report presents a new method of evaluating laminar convective heating rates for a parabolic shaped geometrical configuration in a hypersonic flowfield. The approach approximated the aerothermodynamic properties of the environment surrounding the vehicle using an ideal gas chemistry model. Once the correlations were derived, the method was implemented in MATLAB, a numerical computation programming language, to compute the non-dimensional heating rates at various locations along the surface of the parabola. The non-dimensional surface heating rates were then validated using approximate engineering codes BLUNT2D and SABLE[4]. The analytical method was validated for a range of freestream velocities, altitudes, and geometrical parameters by selecting and generating various test scenarios.

Chapter 2

Background Theory

A variety of vehicles have travelled at hypersonic speeds, each with different design specifications based on the mission purpose. Vehicles have flown to hypersonic speeds to launch objects in space, cruise through the atmosphere, and conduct missions to and from space. Some of the design criteria include performance, safety, cost, and compatibility with the environment. For vehicles flying at hypersonic speeds, several critical parameters must be considered to ensure the safety of the spacecraft during re-entry. Designers must consider the trajectory of the re-entry vehicle, aerothermodynamic constraints, high temperature effects, as well as geometry specifications. This chapter will discuss background theory and relevant information regarding these parameters.

2.1 Re-entry Trajectories

Re-entry trajectory design involves considering the re-entry initial conditions. These are defined by the velocity at which the spacecraft is entering the atmosphere and the re-entry flight-path angle. A three-dimensional re-entry corridor defines the constrained space that a re-entry vehicle must pass through to avoid burning up or re-entering back into space. The size of this corridor is dependent on three parameters – deceleration, heating, and accuracy. If the spacecraft strays below the lower boundary (within the undershoot region in Figure

2.1), it will experience too much drag and decelerate rapidly, leading the vehicle to heat up too quickly. Alternately, if the entry angle is too shallow and the spacecraft enters the upper boundary (the overshoot region in Figure 2.1), it will not undergo enough drag to be captured by the Earth's gravitational pull and will return back into outer space. This boundary is referred to as the "skip out" boundary[5].

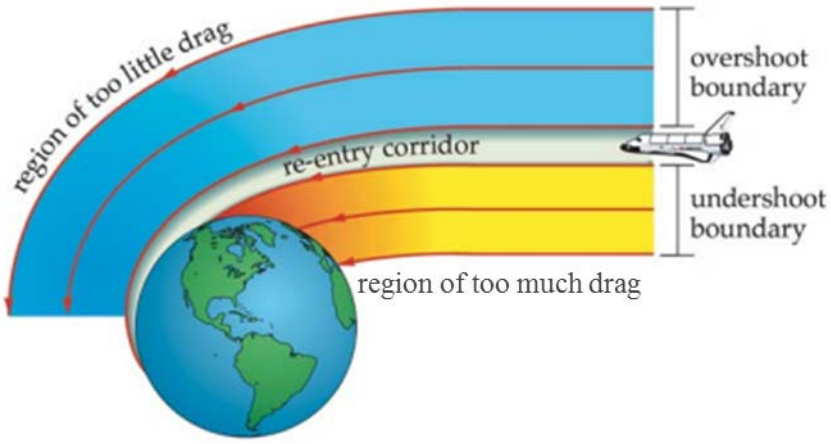

Figure 2.1 - Depiction of the Re-entry Corridor

The two parameters that define the undershoot boundary are maximum deceleration and maximum heating rate. Both of these parameters will increase with higher re-entry velocity or larger re-entry flight-path angle, causing steeper re-entry. On the other hand, the trajectory along the overshoot boundary will cause the largest heat load. The table below describes the advantages and disadvantages of re-entry trajectory design, as discussed above[5]. Both boundaries influence the selection of the Thermal Protection System (TPS) to protect the spacecraft during re-entry.

Table 2.1 - Re-entry Trajectory Design Trade-offs

Parameter		Maximum Deceleration	Maximum Heating Rate	Corridor Width
Re-entry velocity, $V_{re\text{-}entry}$ (with constant γ)	High	High	High	Narrow
	Low	Low	Low	Wide
Re-entry flight-path angle, γ (with constant $V_{re\text{-}entry}$)	High	High	High	Narrow
	Low	Low	Low	Wide

Adding lifting force will expand the size of the corridor, allow a larger margin of error for re-entry trajectories, and improve landing accuracy. By increasing the angle of attack of the vehicle, lift can be added. This will enable the spacecraft to operate similar to an airplane, allowing the onboard pilot to guide the vehicle for a controlled landing. The Space Shuttle utilizes this type of lifting re-entry maneuver to enter Earth's atmosphere after completing a mission at the International Space Station. The Shuttle will complete a deorbit burn to establish a -1° to -2° re-entry flight path angle, rotate its nose to a 40° angle of attack, and finally begin the re-entry phase[5]. This method of re-entry is referred to as a gliding trajectory.

Vehicles in Low Earth Orbit (LEO), such as the Space Shuttle, will re-enter at an altitude of 122 km and a speed of 7.9 km/s (approximately Mach 25). This is known as orbital or satellite velocity, where the maximum deceleration will be well under 2 g. The re-entry altitude and velocity profile for the Space Shuttle can be seen below in Figure 2.2[5]. On the other hand, both Apollo and Gemini capsules re-entered the Earth's atmosphere with minimal lifting ability at an entry speed of 11.2 km/s (greater than Mach 35). This is referred to as escape velocity, where the re-entering bodies withstand up to 12 g[5].

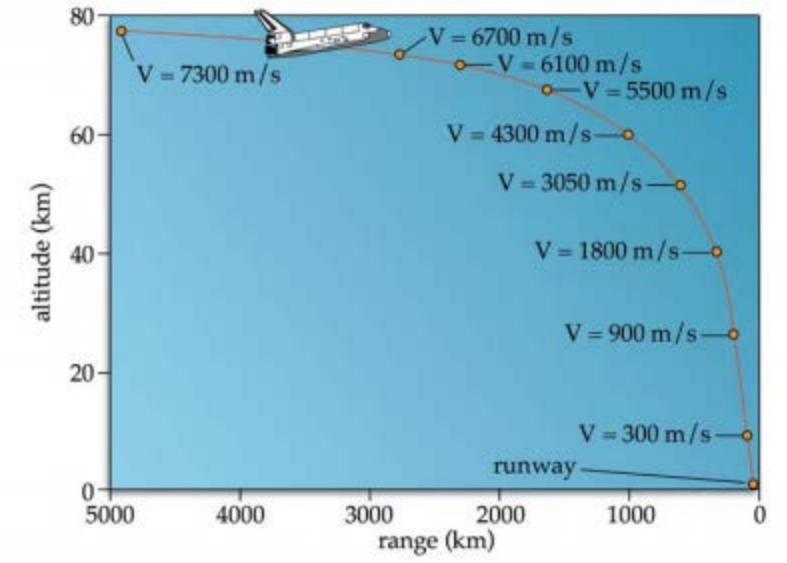

Figure 2.2 - Space Shuttle Re-entry Profile

Alternately, a ballistic trajectory is a more simple approach to re-entry. This method assumes that zero lift force is generated by the body, allowing the vehicle to drop into the atmosphere without control. The primary design parameter for a ballistic re-entry is the ballistic coefficient β,

$$\beta = \frac{W}{C_D A} \tag{2.1}$$

where W is the weight of the vehicle, C_D is the drag coefficient, and A is the reference area used to determine the drag coefficient. Heating and deceleration are not as extreme for a lower value of β as they are for a higher β value. Prior to the Space Shuttle, ballistic re-entry method was utilized for almost all vehicles returning to Earth, including for some of the early Inter-Continental Ballistic Missiles (ICBM). Additionally, the manned Mercury spacecraft by

the United States and the unmanned Discoverer, Pioneer Venus, and Galileo spacecraft used a ballistic trajectory during atmospheric re-entry[6].

A skip re-entry trajectory utilizes features of both ballistic and gliding re-entry methods. The vehicle skims through the outer edges of the atmosphere to generate drag and decelerate the vehicle. Simultaneously, the vehicle produces a lift-to-drag ratio between one and four and consumes the generated lift to pitch the spacecraft upwards and exit the atmosphere again. After repeating this process several times and depleting a substantial amount of kinetic energy, the spacecraft gradually slows down and safely re-enters the Earth's atmosphere. Lastly, the vehicle uses a ballistic path to land. This method of re-entry is depicted in Figure 2.3[6]. A skip entry is useful when the range of trajectory needs to be controlled, allowing the vehicle to land in locations that are not possible with a single entry trajectory (such as those discussed above). However, due to the higher maximum heating rates resulting from the increasing friction heat during the skips, this method has never been utilized to land a manned spacecraft[7].

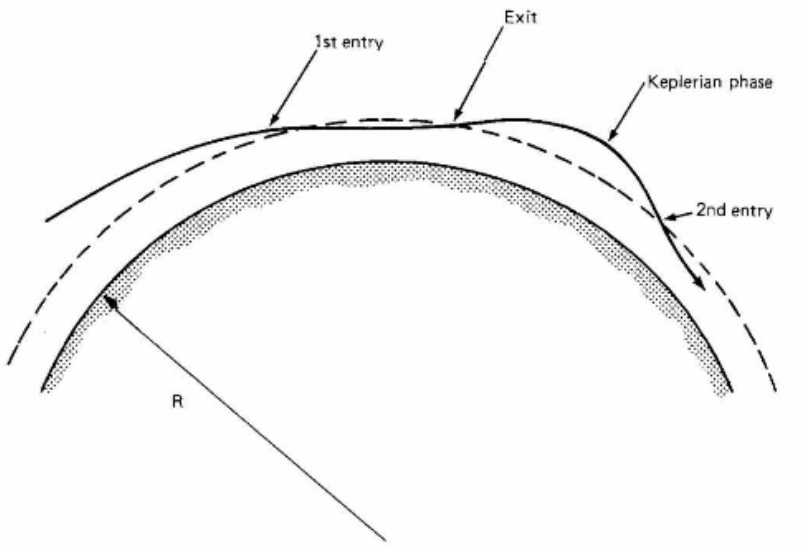

Figure 2.3 - Skip Re-entry Trajectory

2.2 Re-entry Temperatures

A spacecraft traveling at hypersonic speeds during the re-entry phase of the flight suffers from extremely high temperatures. A strong shock is formed ahead of the body, transforming a large amount of kinetic energy into thermal and chemical energy. This produces very high temperatures in the shock layer near the nose of the body. Additionally, downstream of the nose, the frictional dissipation within the hypersonic boundary layer around the surface of the body creates extremely high temperatures. An illustration of the high temperature regions in a hypersonic flowfield around a blunt-nosed body is shown below[8].

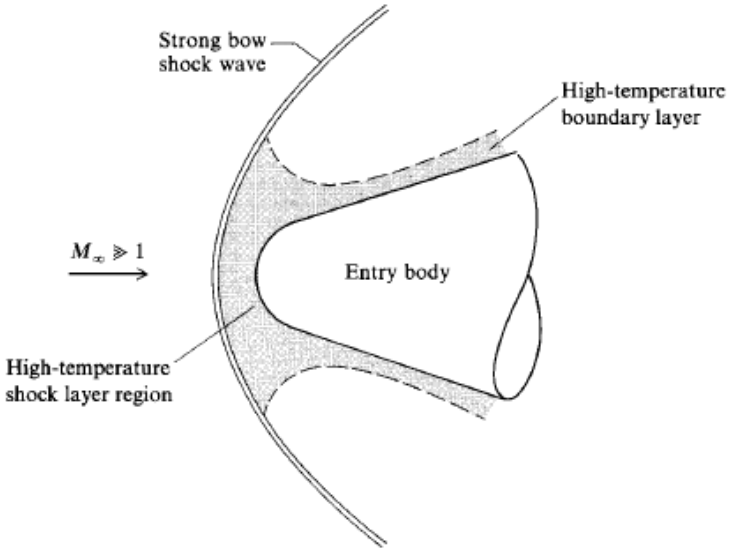

Figure 2.4 - High Temperature Regions around a Blunt-nosed Entry Body

The bottom portion of the Space Shuttle experiences re-entry temperatures of up to 3,150 degrees Rankine[5]. While these temperatures are extreme, some of the earlier spacecraft suffered from far worse temperatures during the re-entry phase of the mission. The shock layer in the nose region of the Apollo capsule, designed to complete missions to the Moon,

reached temperatures of 20,000 °R during re-entry onto Earth's atmosphere[8]. The maximum temperatures that the Apollo capsule sees are hotter than the surface of the sun.

High-temperature flows are modeled differently than the flow of a gas with a constant specific heat value. When gases are below the temperatures of 3,600 °R, the flow can be modeled with the assumption of a constant specific heat value. However when modeling flows beyond those temperatures, real-gas effects begin to occur. The effects cause the flow to become chemically reactive and the gas becomes partially ionized plasma as a result of ionization. The thermodynamic properties become completely different and heat-transfer rates become significantly higher when dealing with any aspect of high-temperature application. An illustration is shown below to specifically describe when chemically reacting effects become dominant for high-temperature flows. The figure illustrates dissociation and ionization in air at a pressure of 1 atmosphere[8].

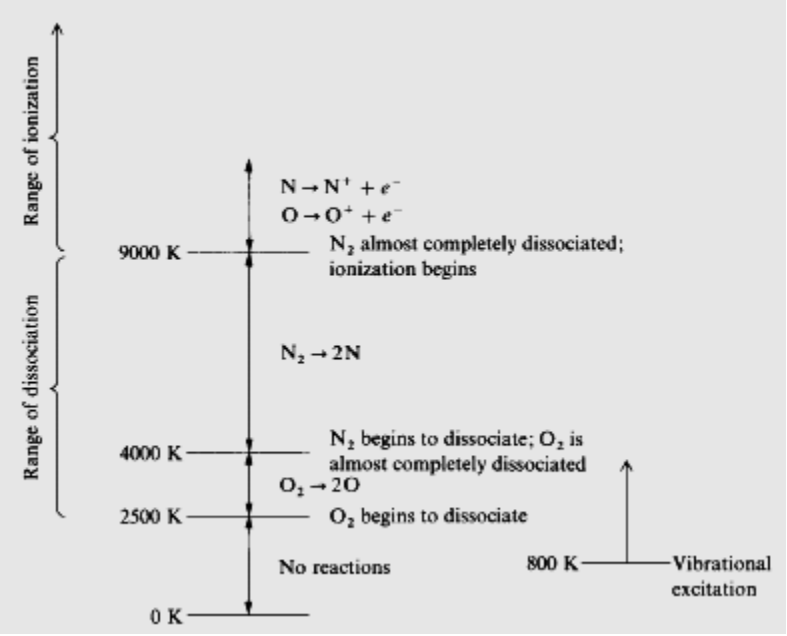

Figure 2.5 - Illustration of Dissociation and Ionization for Air at a Pressure of 1 atm

The Earth's atmosphere consists of a combination of diatomic nitrogen and oxygen molecules. At temperatures greater than 3,600 °R (2,000 K), these diatomic molecules dissociate into oxygen and nitrogen atoms and ionize into O^+ and N^+ ions and electrons. This causes the air to behave as a chemically reacting gas. This can be seen in the figure above. During atmospheric re-entry at hypersonic speeds, the entry vehicle will undergo these changes and experience large heat inputs due to the high temperatures. Thus, a key objective in the design of an entry vehicle is to deflect the high-temperature gases away from the surface and to shield the vehicle from these severe conditions[9].

2.3 Aerodynamic Heating

The thermal loads imposed on a spacecraft create one of the largest limitations in the design process of an entry vehicle. The two types of thermal loads are the total heat load and the instantaneous aerodynamic heating rate. Aerodynamic heating represents the heat transferred into the body due to the movement of the surrounding gas. The maximum or peak aerodynamic heating usually occurs in the stagnation point regions of the body. The surface of the blunted nose and the leading edge of a wing are examples of stagnation point regions[6]. Both of these thermal loads are important in the design of a thermal protection system (TPS). The total heat load impacts the thickness of the TPS while the maximum heating rate will influence the material type selected for the TPS.

Aerodynamic heating occurs in the form of convective heating and radiative heating. Convective heating within the boundary layer surrounding the body results from the frictional forces that cause viscous dissipation. Viscous dissipation converts the kinetic energy of the flow into internal energy. This occurs when the vehicle passes through the fluid during atmospheric re-entry and transfers heat from the fluid to the body. The fluid is heated

by passage through a strong bow shock ahead of the vehicle[6]. As the air becomes very hot and the wall temperatures increase, thermal radiation begins to occur.

Thermal radiation heating is generated from the radiating shock layer gases that are present from dissociation and ionization of the gas molecules at high temperatures. Radiative heating transfers energy between two points by usage of electromagnetic waves. Thermal radiation becomes a significant source of aerodynamic heating when the entry velocity is greater than 10 km/s[5] and the gas temperatures are high enough that the fluid radiates energy in all directions. For air, the onset of thermal radiation occurs when temperatures have reached 10,000 K. Figure 2.6 depicts radiative heating due to high temperature shock layer on a blunt-nosed body[9].

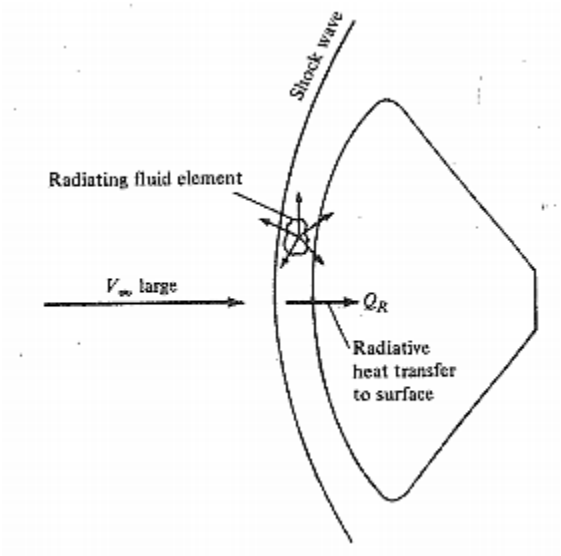

Figure 2.6 - Effects of Radiative Heating

Additionally, Figure 2.7 shows the effects of convective heating and radiative heating for increasing velocities. From the figure, it can be seen that radiative heating becomes more

dominant at higher free-stream entry velocities. The Apollo capsule that completed missions to the Moon experienced entry velocities of 11 km/s (36,000 ft/s), exhibiting mostly convective heating and little radiative heating (approximately 30%). However, for possible future manned missions to other planets with an entry velocity of 15.2 km/s (50,000 ft/s), 95% of total heating will be due to radiative heating[9]. This can be attributed to the fact that as entry velocities escalate, shock layer temperatures will increase.

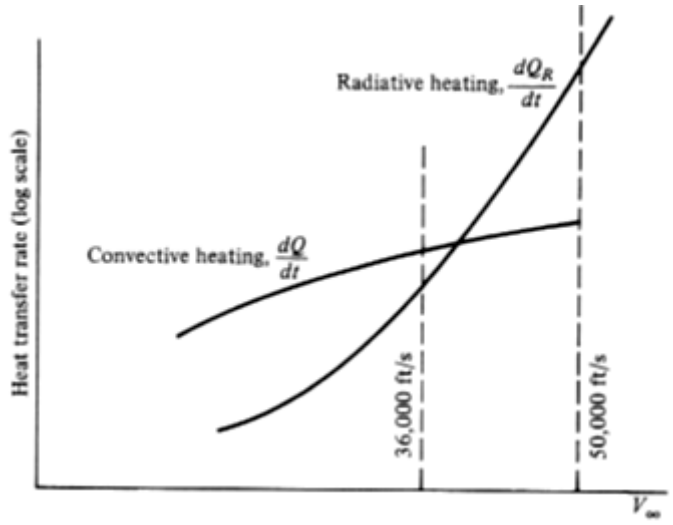

Figure 2.7 - Convective and Radiative Heating Rates with Increasing Velocities

This research will study trajectories from Low Earth Orbit (such as from the International Space Station) that generate velocities lower than required for radiative heating to become dominant. Therefore, this research will focus only on convective radiative heating rates.

2.4 Re-entry Geometries

When designing an atmospheric entry vehicle that can withstand hypersonic speeds, it is important to quantify the impact of body geometry on the vehicle performance through the aerothermodynamic environment. The geometric configuration of the vehicle affects the total amount of energy transferred to the spacecraft from the beginning to the end of the mission. Since it is desired to minimize the total heating experienced during re-entry, it is vital to study and select the appropriate geometry according to mission requirements.

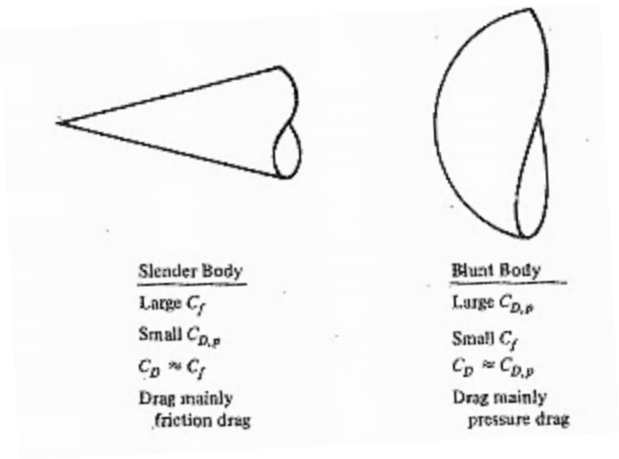

Figure 2.8 - Sharp-nosed Cone and Blunt-nosed Bodies

The two extreme aerodynamic configurations utilized for hypersonic flow are a sharp-nosed cone body and a blunt-nosed body. A sharp-nosed cone slender body generates a much larger skin friction drag than pressure drag. Alternatively, a slender body produces a much larger pressure drag than the skin friction drag. An illustration of both body types are shown in the figure above[9]. In *Introduction to Flight*, Anderson concludes "to minimize entry heating, the vehicle must have a blunt nose". A blunt-nosed body will create a strong detached bow shock wave ahead of the nose (shown in Fig 2.9)[5]. This indicates that a considerable portion of the shock wave will be normal to the nose region and most of the high-temperature air around the front of the vehicle will simply flow past the body without touching the surface. For this

shape, the heat generated during entry will be spread over a large volume. Consequently, the blunt-nosed body will transfer most of the initial kinetic energy and potential energy onto the surrounding air, instead of utilizing the energy to heat the surface of the body. Therefore, a blunt-nosed body will minimize the total heat imparted on the vehicle[9].

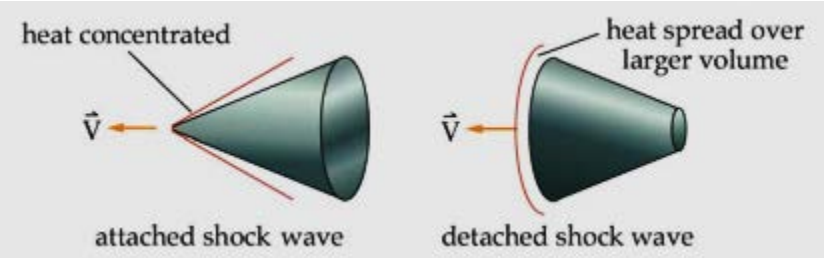

Figure 2.9 - Shock Waves and Heat Concentration

On the other hand, streamlined vehicles undergo attached shock wave during re-entry. Sharp-nosed cone body is an example of a streamlined geometry. This configuration for the geometry will generate concentrated heat near the sharp tip of the cone. This causes the nosed cone tip to reach extremely high temperatures. Most material types will melt through due to their inability to withstand these temperatures. As noticed in the figure above, a nosed cone body forces the heat to remain within a small volume, resulting in poor heat transfer to the air flow and higher heating rates[5]. Thus, sharp-nosed cone bodies are not practical to use for space flight. For this research, a blunt-nosed geometry with a parabolic shape will be studied.

Chapter 3

Aerothermodynamic Analysis and Methods

An aerothermodynamic environment can be described as the forces, moments, and heating distributions of a vehicle traveling at hypersonic speeds. There are many factors involved in determining the aerothermodynamic properties of a vehicle. Some of these include boundary-layer transition, turbulence, viscous/inviscid interactions, separated flow, and equilibrium/non-equilibrium chemistry. The design process of a hypersonic vehicle can, thus, be very complicated. Consequently, the analysis of hypersonic aerothermodynamic environment requires the usage of experimental measurements (flight tests and ground-based tests), numerical solutions, and analytical methods. All of these methods have advantages and disadvantages associated with them. This chapter will provide literature search on these various methods as well as detail the challenges related to them.

3.1 In-flight Tests

In-flight simulations at hypersonic speeds can be performed to determine aerothermodynamic phenomena. Flight tests are utilized to provide information regarding the aerothermodynamic environment that cannot be obtained using any other types of testing. Additionally, flight tests can verify the accuracy of results acquired using ground test simulations. However,

flight tests are generally very expensive and require a great deal of planning to successfully run and generate results. The measurements taken during in-flight testing must provide data that cover all test conditions with sufficient accuracy. While this is difficult to achieve, it is important to note that ground-based tests or CFD numerical solutions cannot replace in-flight tests.

In *Critical Hypersonic Aerothermodynamic Phenomena**, Bertin and Cummings describe the following reasons (suggested by Buck et al. in 1963 and Neumann in 1989) for conducting in-flight tests: assess currently developed technologies and recognize unexpected issues with them, evaluate the reliability of technology for other larger-scale applications, validate ground-based tests and identify differences and similarities between flight and ground-based tests, and gain an understanding of hypersonic flight and overall performance of the vehicle. The three main groups of measurements that are taken during in-flight testing are atmospheric properties, sensor data collected from the external of the vehicle, onboard data from the vehicle[10].

Numerous in-flight test programs in the 1960s focused on gathering information on boundary layer transition for a hypersonic flowfield. Reentry-F vehicle was utilized to obtain in-flight test data for hypersonic boundary layer transition for Mach numbers up to 20. Most of the information learned from using this flight vehicle is still used today. Furthermore, flight test data have also been collected by the unmanned Apollo Command Module missions (017 and 020) and by the Space Shuttle Orbiter vehicle. The Space Shuttle provided information on aerothermodynamic parameters by the usage of thermocouples that were embedded in the TPS of the vehicle. This test on the Space Shuttle led to the creation of a larger flight envelope for the Orbiter[10]. Due to the costs associated with each flight test, it is vital to make as many measurements as possible during each experimental test.

3.2 Ground-based Tests

For many decades, the only operational reused hypersonic flight vehicle was the Space Shuttle. The space shuttle was primarily designed and developed by the usage of some approximate methods and ground-based facilities. When the Space Shuttle development first began under the Space Transportation System program, the capabilities of numerical solutions of aerothermodynamics were very restricted[11]. When a few critical "return-to-flight" issues were recognized within the aerothermodynamic environment experienced by the Space Shuttle, wind tunnel facilities were utilized. These concerns were related to the heating in the bipod section during launch and aerodynamic forces and moments during re-entry[10]. Wind tunnel tests provided information on the aerothermal conditions regarding these issues.

Ground-based testing facilities are critical for the recreation of the aerothermodynamic properties experienced by hypersonic vehicles during flight. However, no single testing facility exists that can simulate a hypersonic environment entirely. For this reason, multiple ground-based facilities are utilized to generate the various aspects of a vehicle traveling through a hypersonic flowfield. Measurements regarding the aerothermodynamic properties, such as aerodynamic forces and moments, surface pressure distribution, heat transfer distribution, are acquired using conventional and shock-heated wind tunnels, shock tubes, and arc-heated testing locations. Some of the particular parameters that these ground-based facilities can replicate are free-stream Mach number, Reynolds number, velocity, total enthalpy of the flow, temperature ratio, and density across the shock wave ahead of the vehicle[10]. All of these parameters cannot be simulated simultaneously.

It is important to note that the wall to total temperature ratio measured during a hypersonic flight cannot be modeled exactly using wind tunnel simulations. During a ground-based test, the temperature measurements taken to calculate heat transfer rates are recorded during the

early phase of the run. This indicates that the temperature of the model tested remains relatively low. However, this is not the case during re-entry. As the surface of the vehicle is exposed to the high-temperature environment during re-entry, the wall temperatures increase significantly[10]. From this example, it can be seen that flight conditions during hypersonic flight and re-entry cannot be modeled exactly.

Nevertheless, there are many advantages to performing ground-based tests. For some very complex flowfields, computational modeling cannot replicate the aerodynamic forces, moments, and heat transfer distributions. Ground-based testing can help define some of these parameters that cannot be achieved using computer generated simulations. Partial configurations of elements used on a spacecraft can also be examined to study the behavior of the local flow. Some of the components that are observed individually are hypersonic air-breathing engines and deflected control surfaces. Additionally, ground-based testing can obtain data utilized for developing empirical relations to describe phenomena that is not discovered in analytical and computational modeling (e.g. boundary layer transition and turbulence). Lastly, approximate numerical solutions are validated and calibrated by conducting ground-based experiments.

3.3 Analytical Approaches

Some of the first analytical techniques were developed by researchers interested in describing the characteristics of hypersonic flight nearly 60 years ago. Analytical methods are utilized during the early phases of hypersonic vehicle design. These techniques generate necessary approximations for relatively simple shapes and geometries. While these analytical methods do not provide as accurate solutions as numerical methods provide, they are still used by designers today. Simple capsule geometries are particularly of interest when considering missions requiring suborbital velocities. For example, the lower surface of the Space Shuttle

Orbiter was represented by empirical relations developed by analytical methods. By separating the Orbiter into an assortment of shapes (such as cones, cylinders, flat plates, spheres, and wedges), each section of the Shuttle can be examined using analytical solutions. The figure below illustrates the flow models used to represent the Space Shuttle. The leading edge of the wing is denoted by a swept cylinder, to evaluate the leading edge heating rates[10].

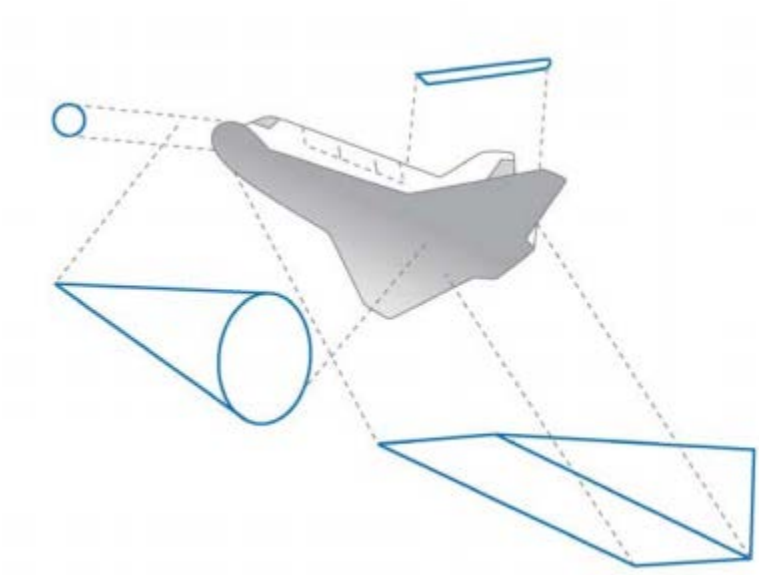

Figure 3.1 - Analytical Representation of the Space Shuttle

The purpose of this research is to develop simple heating relations for an axisymmetric ogive-shaped parabolic geometry. This chapter is intended to provide the reader with some background material on this subject. The following sections will cover various analytical techniques that have been previously developed to compute heating rates for various geometrical configurations.

3.3.1 Fay and Riddell

In a journal article titled *Theory of Stagnation Point Heat Transfer in Dissociated Air*[13], Fay and Riddell examined and developed boundary layer equations for very high flight speeds where the flowfield interacts with dissociated air. The effects of diffusion and recombination of atoms and ions are included within the boundary layer analysis. The derived correlation for stagnation point heat transfer through equilibrium boundary layer can be seen below,

$$q_{w,0} = 0.57\left(\frac{4}{3}\right)^{j} \mathrm{Pr}^{-0.6}\left(\rho_e \mu_e\right)^{0.4}\left(\rho_w \mu_w\right)^{0.1}\sqrt{\left(\frac{du_e}{dx}\right)}\cdot \ldots \\ \left(h_0 - h_w\right)\cdot\left[1-\left(Le^{0.52}-1\right)\left(\frac{h_D}{h_0}\right)\right] \tag{3.1}$$

where j = 0 for a two-dimensional flow and j = 1 for an axisymmetric flow. Additionally, Pr represents the Prandtl number, ρ signifies the density, μ denotes the absolute viscosity, h represents the enthalpy per unit mass of mixture, and Le describes the Lewis number. The subscripts (D- diffusion, e- edge of the boundary layer, w- wall, 0- stagnation point) describe the flow conditions at specific locations of the flowfield. Various parameters used in the above equation are detailed below,

$$\mathrm{Pr} = \frac{\mu c_p}{k} \tag{3.2}$$

$$Le = \frac{\rho D_{12} c_P}{k} \tag{3.3}$$

$$h_D = \sum_{i=1}^{n} c_i \cdot \Delta h_{f,i} \tag{3.4}$$

The last term in Equation 3.1 describes impact of the chemical reactions. For air, this term is approximated to be one and can be neglected from further calculations. Additionally, the derivation in Equation 3.1 is valid for velocities of 5,800 ft/s to 22,800 ft/s and wall temperatures of 540 °R to 5400 °R[8]. It is important to note that the correlation above (Eq. 3.1) is valid for a stagnation point in chemical equilibrium. While this relation was developed by Fay and Riddell in 1957, it is still used as an accurate method to estimating convective stagnation point heating rates for bodies in a hypersonic flowfield today.

3.3.2 Lester Lees

Lester Lees published a scholarly article in the journal *Jet Propulsion* in 1956, in which he developed two limiting cases of laminar heat transfer rates over blunt-nosed geometries traveling at hypersonic speeds[3]. He discusses that in order to decrease heat transfer to the vehicle, all bodies flying at hypersonic flight speeds must be, in some measure, blunt-nosed. The two geometries that he examined and developed non-dimensionalized laminar convective heating rate correlations for are a hemispherical nose and a blunt-nosed cone. Lees establishes an analytical representation of the heat transfer rate in terms of the distance away from the stagnation point for the blunt-nosed body. He uses the stagnation point heat transfer rate as a reference point to non-dimensionalize the quantity. This method of expressing the heat transfer rate parameter dates back to the design of the Mercury spacecraft in 1961. The reference stagnation point for a blunt-nosed geometrical configuration occurs at zero angle of attack[9]. Lees developed a limiting approximation for the heat transfer rate, q_w, by dividing the laminar boundary layer heat transfer rate along the surface of the geometry by the stagnation point heat transfer rate, $q_{w,o}$.

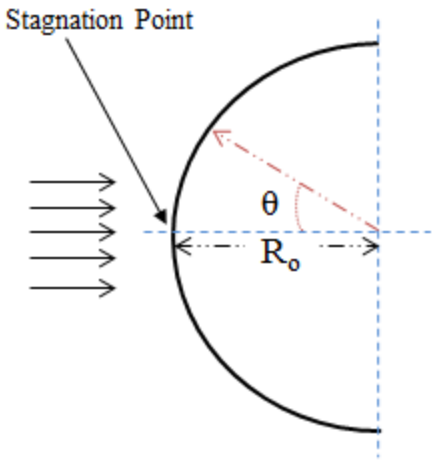

Figure 3.2 - Geometrical Illustration of a Hemispherical Nose

Figure 3.2 depicts the geometrical representation of a hemispherical nose in a hypersonic flowfield. The angle between the nose radius vector (R_o) and flight direction is denoted by θ. The convective heating rates for a laminar boundary layer, assuming perfect gas chemistry, for this geometry can be seen below[3]. Note that the correlation is strictly in terms of three parameters: γ_∞, M_∞, and θ.

$$\frac{\dot{q}_w(\theta)}{\dot{q}_{w,o}} = \left[D(\theta)\right]^{-0.5}\left[2\theta\sin\theta\left\{\left[1-\left(\frac{1}{\gamma_\infty M_\infty^2}\right)\right]\cos^2\theta+\left(\frac{1}{\gamma_\infty M_\infty^2}\right)\right\}\right] \tag{3.5}$$

where D(θ) is,

$$D(\theta)=\left(1-\frac{1}{\gamma_\infty M_\infty^2}\right)\left(\theta^2-\frac{\theta\sin 4\theta}{2}+\frac{1-\cos 4\theta}{8}\right)+\ \ldots \\ \frac{4}{\gamma_\infty M_\infty^2}\left(\theta^2-\theta\sin 2\theta+\frac{1-\cos 2\theta}{2}\right) \tag{3.6}$$

This method developed by Lees is valid for Mach numbers greater than two. However in reality, these correlations are not an accurate representation at very high Mach numbers with the assumption of perfect gas chemistry. The other geometrical configuration examined by Lees is shown below.

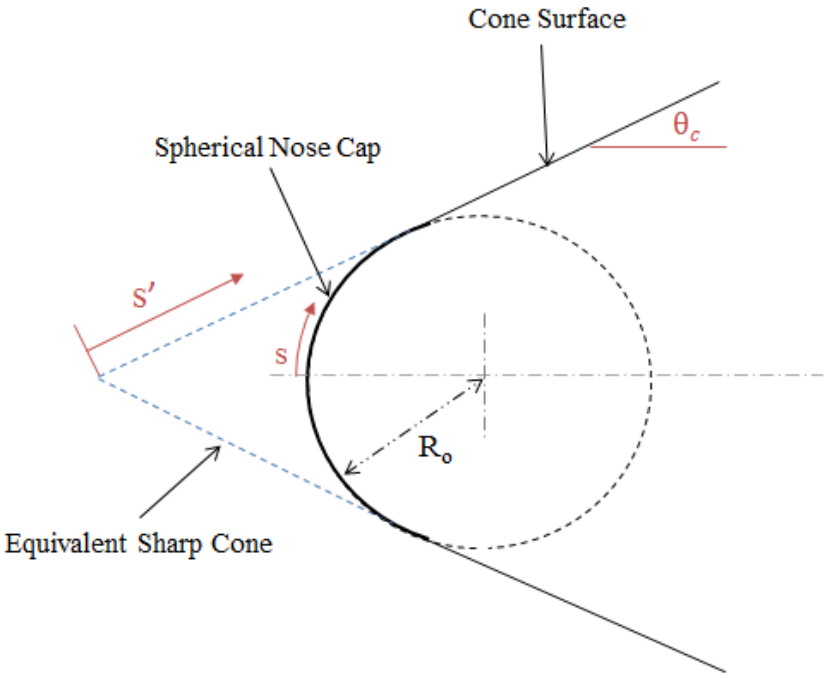

Figure 3.3 - Blunt-nosed Cone Geometry

In the figure, R_o represents the nose radius, θ_c denotes the equivalent sharp cone half angle, and s' represents the distance from the tip of the equivalent sharp cone to points along the surface of the cone. The distance from the tip of the spherical nose cap to locations along the surface, s, can be related to s' by the following equation[3],

$$\frac{s'}{R_o} = \cot\theta_c + \left[\frac{x}{R_o} - \left(\frac{\pi}{2} - \theta_c\right)\right] \tag{3.7}$$

Now the laminar convective heat transfer ratio for a blunt-nosed cone with a spherical cap can be expressed in terms of the above quantity, s'/R_o. The expression for the heating rate at any point along the surface in relation to the stagnation point is detailed below[3],

$$\frac{\dot{q}_w(s')}{\dot{q}_{w,0}} = \frac{A(\theta_c)\left(s'/R_o\right)}{\left(B(\theta_c)+\left(s'/R_o\right)^3\right)^{1/2}} \tag{3.8}$$

The above equation is valid for when $\frac{s'}{R_o} \geq \cot\theta_c$. The relations for $A(\theta_c)$ and $B(\theta_c)$ are provided by Lees for all Mach numbers. However, he simplifies these relations for high Mach numbers ($M_\infty \sin\theta_c \gg 1$) as the following[3],

$$A(\theta_c) \cong \frac{\sqrt{3}}{2}\sin\theta_c\sqrt{\frac{\pi}{2}-\theta_c} \tag{3.9}$$

$$B(\theta_c) \cong \frac{3}{16}\frac{1}{\sin^4\theta_c}\left[\frac{D(\theta)}{\theta}\right]_{\theta=\frac{\pi}{2}-\theta_c} - \cot^3\theta_c \tag{3.10}$$

$$D(\theta) \cong \theta^2 - \frac{1}{2}\theta\sin 4\theta + \frac{1}{8}(1-\cos 4\theta) \tag{3.11}$$

Since the scope of this research considers hypersonic flight speeds ($M \gg 1$), the simplified correlations will be utilized. By using the method described by Lester Lees, an analytical solution for an axisymmetric geometry can be determined. The technique required to evaluate the heating rates along the surface of a body are relatively simple but provide an approximation that can be utilized during the early phase of the design process. It is important to note that Lees considers only a sphere and a blunt-nosed sphere cone for his calculations. Other geometrical configurations can also be studied with the technique he

developed. Some limitations with his approach are that the approximation for computing heating rates are valid for a laminar flow and requires the assumption of perfect gas chemistry.

3.3.3 Generalized Heating Relations

Another method has been examined and developed by many researchers to compute aerodynamic heating of a body in a hypersonic flowfield. This approach is referred to as the generalized heating equations. These relations attempt to model convective stagnation point heating in terms of body nose radius and other flow parameters. In addition, these correlations can evaluate laminar and turbulent flow over a flat plate at an angle of attack[12]. The generalized heating equations can be written in the following simple form,

$$q_w = \rho_\infty^N V_\infty^M C \tag{3.12}$$

where q_w quantifies the total heat flux at the wall, ρ_∞ represents the freestream density, V_∞ denotes the freestream velocity, C signifies an expression specific to the body geometry, and N and M are numerical constants based on the flowfield. The values and expressions for N, M, and C are detailed in the tables below for several flow types[8]. It is important to note that all of the formulations below are to be used with SI units only. The heat flux results will be in units of W/cm^2.

Table 3.1 - Coefficients for Stagnation Point Flow

Coefficient	Value
N	0.5
M	3.0
C	$1.83x10^{-8} \cdot R_n^{-0.5} \cdot \left(1 - \frac{h_w}{h_0}\right)$

Table 3.2 - Coefficients for Laminar Flow over a Flat Plate

Coefficient	Value
N	0.5
M	3.2
C	$2.53x10^{-9} \cdot (\cos(\alpha))^{0.5} \cdot \sin(\alpha) \cdot x^{-0.5} \cdot \left(1 - \frac{h_w}{h_0}\right)$

Table 3.3 - Coefficients for Turbulent Flow over a Flat Plate

V_∞	Coefficient	Value
$\leq 3962 \frac{m}{s}$	N	0.8
	M	3.37
	C	$3.89x10^{-8} \cdot (\cos(\alpha))^{1.78} \cdot (\sin(\alpha))^{1.6} \cdot x_T^{-0.2} \left(\frac{T_w}{556}\right)^{-0.25} \cdot \left(1 - \left(1.11 \frac{h_w}{h_0}\right)\right)$
$> 3962 \frac{m}{s}$	N	0.8
	M	3.7
	C	$2.2x10^{-9} \cdot (\cos(\alpha))^{2.08} \cdot (\sin(\alpha))^{1.6} \cdot x_T^{-0.2} \cdot \left(1 - \left(1.11 \frac{h_w}{h_0}\right)\right)$

In the tables above, R_n indicates the nose radius of the geometry (in feet), α represents the flat plate angle of attack (in degrees), x denotes distance from the leading edge (in feet), x_T - represents the distance from the transition point (in feet), h_w signifies enthalpy at the wall (in ft·lb/slugs), and h_o represents the total enthalpy (in ft·lb/slugs).

Additionally, other correlations for stagnation point heating have been developed by Detra et al.[14] in 1957 and Scott et al.[15] in 1985. Both of these relations, which are written below, are slightly different than those derived by Anderson (discussed above). Nonetheless, the results generated using all three methods are very comparable.

$$\text{Detra et al.: } q_{w,0} = \frac{17,600}{\sqrt{R_n}}\left(\frac{\rho_\infty}{\rho_{sea-level}}\right)^{0.5}\left(\frac{V_\infty}{26,052\frac{ft}{s}}\right)^{3.15} \tag{3.13}$$

$$\text{Scott et al.: } q_{w,0} = \frac{18,300\left(\rho_\infty\right)^{0.5}}{\sqrt{R_n}}\cdot\left(\frac{V_\infty}{10^4}\right)^{3.05} \tag{3.14}$$

3.4 Numerical Methods

Due to the increase in complexity as a flow transitions from supersonic to hypersonic, modeling the behavior of the flow numerically or experimentally, as discussed in previous sections, becomes very challenging. Computational techniques are utilized to provide flow related information during the configuration selection phase. It is necessary to evaluate critical flow conditions to determine the operational envelope for a vehicle design. Aside from flight and ground testing, computational based codes serve as another essential source of information. Currently, computational methods such as computational fluid dynamics

(CFD) and approximate engineering codes are utilized to numerically compute the hypersonic aerodynamic flowfield. Both of these types of computational schemes have advantages and difficulties associated with them.

Simulation and analysis of a hypersonic environment using CFD codes can be separated into three categories. As discussed by Anderson in *Hypersonic and High-Temperature Gas Dynamics*, these three CFD techniques include Viscous-Shock-Layer (VSL), Parabolized Navier-Stokes (PNS), and Full Navier-Stokes. These methods are more accurate than engineering codes based on boundary layer equations. Both VSL and PNS methods provide a less precise solution than the full N-S equations. CFD codes allow the computation of many aspects of hypersonic flow including shape of the shock generated, differences in variables between the shock layer and the body, effect of skin friction, etc[8]. Before using a CFD code, the object that is being analyzed must be represented and well defined. In order to do this, a grid must be generated around the geometry by separating the surface of the vehicle into a finite number of elements. This can be an extremely challenging and time consuming process, as there can be many configurations of grids that can be utilized. This process becomes more complicated with a more complex geometry[10]. Once the grid is generated, the above mentioned algorithms can be implemented to simulate the behavior of the fluid flow as it interacts with the surface of the geometry.

It is important to discuss the difficulties that arise with CFD modeling of a hypersonic flowfield. Some of the many features that are complex to model are thin shock layers, viscous/inviscid interaction, real-gas effects (dissociation and ionization of air at high temperatures), and rarefication at high altitudes[10]. To mitigate some of these problems and decrease the amount of run-time and cost, numerical algorithms make simplified assumptions. Nevertheless, computational solutions are very beneficial in the aerothermodynamics field, particularly for low-speed, less complicated models. Much work is still required to represent all aspects of a hypersonic flowfield as a whole using

computational methods. This section will detail some numerical solutions that can be utilized to compute the heating rates of a vehicle traveling at hypersonic speeds.

3.4.1 Navier-Stokes Solutions

The solution of the full Navier-Stokes equations are known to be the most accurate calculations of a hypersonic viscous flow. These comprise of solving the continuity, x-momentum, y-momentum, z-momentum, and the energy equations[8]. Navier-Stokes code solvers provide time-marching solutions regarding surface heating rates of hypersonic vehicles during re-entry that are the closest to measured flight data. Many numerical solutions have been developed in the past and are currently being examined today, using explicit and implicit finite difference methods. The development of a code that solves Navier-Stokes equations for hypersonic flows is currently a very high level research project.

Langley Aerothermodynamic Upwind Relaxation Algorithm, known as LAURA, is a previously developed N-S solver by National Aeronautics and Space Administration (NASA). LAURA is a structured, multi-block, computational aerothermodynamic simulation code. This algorithm employs a finite-volume discretization technique to evaluate solutions to inviscid, thin-layer Navier-Stokes (TLNS), or full Navier-Stokes equations. The motivation for this code was due to the growing interest in simulating viscous, hypersonic flowfield to design space vehicles for transport and exploratory purposes[16].

One of the advantages of using time-marching solutions to the complete Navier-Stokes equations is that an entirely separated flow in any direction can be computed, unlike any of the other solver previously mentioned in this section. The Parabolized Navier-Stokes equations only allow calculating the solution for a separated flow in the crossflow direction[8]. However, these full Navier-Stokes solvers require the usage of supercomputers to store large

amounts of data and allow lengthy running time to reach a converged solution. With an increase in the complexity of initial flow criteria and geometrical configuration of the vehicle, the running times become even more massive. To compute the behavior of a vehicle in a hypersonic flowfield during re-entry, full N-S based solvers can take up to weeks to achieve a single solution. Thus, N-S code solvers are not the best methods to utilize during the initial phase of design, but instead during the final stage when accuracy of the results is of the utmost importance.

To conclude this section, practical uses of complete N-S solvers, such as to determine ways of decreasing drag and heat transfer to a blunt-nosed body, are essential in modern hypersonic aerodynamics along with other numerical and analytical techniques[8] (discussed in the next section).

3.4.2 Approximate Boundary Layer Codes

As mentioned in the previous section, a numerical method that can generate detailed approximations regarding the hypersonic flowfield while minimizing computational time is necessary during the preliminary phase of a design. Boundary layer code solvers deliver an approximate solution to the Navier-Stokes equations. Boundary layer codes provide details of a hypersonic viscous flow based on the principals of boundary layer theory. Boundary layer equations require the computation of the inviscid solution before calculating the viscous solution. By solving the inviscid flow over a body using numerical CFD methods, information regarding the outer-edge boundary conditions can be obtained. The flow properties at the outer-edge of the boundary layer can then be utilized to determine the boundary-layer profiles using a finite difference method. The boundary layer solver will use the outer-edge conditions as inputs within the code to solve for the detailed flowfield profile within the boundary layer of the flow, including the local surface temperature. The local

temperature gradient at the surface can be used to determine the aerodynamic heating distribution along the surface of the body.

The remainder of this section will discuss some boundary layer codes and inviscid flow solvers that have been previously developed. SABLE is an approximate boundary layer code written and developed by H. Harris Hamilton II, Daniel R. Millman, and Robert B. Greendyke in 1992[4]. SABLE can compute the non-similar, axisymmetric boundary layer equations by using an implicit finite-difference method. The code has the capability of modeling laminar and turbulent flow for an ideal gas, carbon tetrafluoride (CF_4), or equilibrium air chemistry. The code can generate boundary layer solutions within a matter of seconds, unlike CFD codes that can take weeks to converge. There exists, however, a drawback to this code- it must be operated in combination with a structured grid generated inviscid flow solver.

Written by one of the same authors as SABLE, BLUNT2D is a structured grid inviscid flow solver. It was created by H. Harris Hamilton II and John R. Spall in 1986. This inviscid code provides time-dependent results for an axisymmetric flow over a blunt body[17]. Similar to SABLE, the average run-time for BLUNT2D is very little, reaching a converged solution in a few minutes. The combined usage of SABLE and BLUNT2D can quickly give information regarding the aerodynamic heating distribution over the surface of a blunt body.

As an application of SABLE and BLUNT2D, Brian Trench developed an innovative approach to estimating laminar convective heating rates in 2012. This method considers blunted sphere cones with different half angles in a hypersonic flowfield at various angles of attack. Using the aerothermodynamic data provided by SABLE, the laminar convective heating distribution in a non-dimensionalized form was determined for equilibrium air chemistry. The correlations developed are valid over specific freestream velocities, altitudes,

and nose radii of the geometry. Furthermore, this method also provides the relations for the stagnation point heating[18].

Other examples of approximate engineering codes that can evaluate the convective heating rates for vehicles in hypersonic flow are LATCH and UNLATCH. Langley Approximate Three-Dimensional Convective Heating, also known as LATCH, is a method to calculate the viscous solution to the boundary layer equations using a single block structured grid[19,20]. Moreover, UNLATCH is a vicious flow solver that utilizes unstructured grids[21]. Both of these codes are based on the fundamentals of axisymmetric analog for general three-dimensional boundary layers. An axially symmetric similarity assumes a small viscous crossflow in the boundary layer and can be disregarded. This reduces and simplifies the three-dimensional boundary layer equations into the axisymmetric boundary layer equations[21]. By substituting the radius of the axisymmetric body with a metric coefficient, the heating distribution on a three-dimensional body can be evaluated along the inviscid surface streamlines. The metric coefficient is determined by the convergence or divergence of the surface streamlines.

However similar to SABLE, both of these engineering codes require the usage of a three-dimensional inviscid flow solver to compute the inviscid flow properties first before running them. CART3D, typically used in combination with LATCH and UNLATCH, is an inviscid code that can calculate laminar and turbulent solutions based on a finite volume discretization method. It was initially developed for subsonic and transonic flight speeds, but was later expanded to include hypersonic flight speeds as well. Based on the complexity of the geometry being analyzed, the estimated computer run time for both of these codes (CART3D and LATCH/UNLATCH) together is approximately 15 to 30 minutes.

3.4.3 Interpolation and Extrapolation Programs

Interpolation programs utilize a database with aerothermodynamic information and quickly generate approximate interpolated results according to the trends noticed within the existing data. An interpolation code named Automated Design Space Interpolation (ADSI) was developed by Grant Palmer in 2009. Palmer's code attempts to create surface atmosphere data at a particular point in a trajectory space based on a presently existing database of solutions generated by CFD methods. ADSI studies various complex interpolation techniques in one-dimensional, two-dimensional, and three-dimensional trajectory space. This interpolation program requires a significant amount of database solutions in order to generate results to an acceptable level of accuracy[23].

Another interpolation tool was later developed by Kurt Whittington titled Thermal Reentry Atmosphere Parameters (xTRAP) in 2011. Whittington's method incorporates both interpolation and extrapolation techniques by using boundary layer equations and hypersonic flowfield relations. The aerodynamic flowfield around a vehicle is first evaluated using approximate boundary layer codes such as UNLATCH. Afterwards, databases to be utilized for space trajectory calculations are loaded with information from known solutions. This process requires approximately three days. After the database is populated, the heating rates around the surface of the body can be evaluated within a matter of seconds. Since the heating rates are based on the specified flight conditions, this program allows changes to be made to flight conditions and rapidly obtain the heating distribution. xTRAP was developed in Microsoft Excel to minimize the usability effort as it was intended to be utilized by undergraduate students. However, the accuracy of the interpolations and extrapolations depends solely on the preciseness of the solutions in the databases. This serves as a disadvantage for this tool[24].

Chapter 4

Requirements and Considerations

The objective of this research is to develop the laminar convective heating rates for an axisymmetric parabolic geometry. Following the standard engineering design process, it is important to first describe the user requirements and afterwards outline various design considerations. This section will provide detailed information regarding the preliminary phase of the design.

4.1 Project Requirements

The primary focus of this research is to develop simple correlations to describe the laminar convective heating rates for a particular geometrical configuration. These relations will assist during the preliminary phase of a design when analyzing hypersonic vehicles. Thus, it is important that the heating relations that will be developed and validated must follow some key requirements. The user requirements and appropriate category of evaluation are detailed in the table below.

Table 4.1 - Description of User Requirements

#	Category	Description of Requirement
1	Functionality	The correlations evaluate laminar convective heating rate at any particular point along the body.
2	Functionality	The relations are valid for perfect gas chemistry.

Table 4.1 Continued

3	Functionality	The relations are valid for a range of freestream velocities.
4	Functionality	The relations are valid for a range of altitudes.
5	Functionality	The relations are valid for a variety of nose radius lengths.
6	Accuracy	The results generated must be within 15% accuracy of the results obtained from a proven engineering code.
7	Efficiency	The correlations must be easily implemented on commonly used software.
8	Efficiency	The computer run time of the correlations must be less than 30 seconds.

As can be seen in the table, the user requirements are divided into three different categories. These categories were selected to help classify various concerns of the research project. Correlations will be developed to quickly compute the aerodynamic heating distribution along the surface of a geometry. The relations will have to be valid for various parameters, including a range of freestream velocities, altitudes, and nose radius lengths for the particular gas model assumed within the derivations. A specific range of values that represent a hypersonic aerothermodynamic environment will be selected for the parameters listed. Detailed information about these parameters will be provided in the next section. The correlations must be able to accurately compute the heating distribution at any point along the body for the chosen range of parameters.

When a new method is introduced within the field of engineering, the results generated using the new approach must be validated. This will be done using a previously proven engineering code that calculates laminar convective heating rates for the geometry considered. The aim will be to accurately compute the heating rates using the newly developed technique. The

results must be within 15% accuracy of the solution given by the computer code. As previously mentioned, various ranges of freestream conditions and geometry parameters will be tested to determine the preciseness of the new method.

One of the important aspects of this research is to establish a set of relations that can rapidly evaluate the heating distribution for a re-entry vehicle traveling at hypersonic speeds. Thus, it is desired to make the correlations as efficient as possible, eliminating heavy run times and costs associated with computational methods (such as CFD or approximate engineering codes) and experimental techniques (i.e. ground or flight tests). The primary application of this newly developed approach will be in undergraduate aerospace or aeronautics courses, requiring the method to be simple and accurate.

4.2 Design Considerations

This section details important design considerations and selections made for this research. Specific information regarding the analytical method, geometry, flow type, and gas model selection is explained below.

4.2.1 Analytical Method Selection

To develop correlations to compute the laminar convective heating rates for an axisymmetric blunted nose geometrical configuration, several analytical methods were considered. Some of the analytical methods studied are described in Section 3.3. After much examination, it was determined that Lester Lees' approach explained in *Laminar Heat Transfer Over Blunt-Nosed Bodies at Hypersonic Flight Speeds* would be the most effective and reliable method to base this study on[3]. Various topics of importance are discussed in this article, including

modified Newtonian flow approximation, reduction of heat transfer rates, geometrical formations for hypersonic vehicles, and gas density near the surface and outside of the boundary layer. The method developed by Lees computes the laminar heat transfer rate at any point along the surface of the geometry with respect to the stagnation point heat transfer rate. By representing the heating rate in this manner, many parameters within the calculations are eliminated and the relation becomes non-dimensionalized. The two geometrical configurations he studies are an isothermal hemispherical nose and a blunted nose cone. The effects of increasing the cone half angle are investigated within the analysis.

Due to the simplicity, reliability, and efficiency of Lees' approach, this analytical method was chosen for the research. The ability to approximate the heat transfer distribution along the surface of an axisymmetric parabolic geometry by means of an analytical approach is the objective of this research. Detailed information about the geometry is provided in the next section. The method selected will reduce computation time and cost while providing accurate solutions.

4.2.2 Geometry

The curve of intersection between a plane and a hollow cone will produce conic sections. A perpendicular plane intersecting with a cone will generate a circle. If the plane is at an angle and cuts entirely through the cone, the resulting conic curve will be an ellipse. When the plane is parallel to a line on the surface of the cone and does not cut through the cone, an open-ended parabola is formed. And lastly, a hyperbola is created when the plane is at a smaller inclined angle from the axis of the cone. The figure below depicts the intersections of the plane and the cone as well as the four resulting conic curves[25].

All four curves can be represented with one relation. The equation of the general conic curves is listed below,

$$r^2 = 2R_o x + Bx^2 \tag{4.1}$$

where R_o signifies the nose radius and B is a variable based on the particular conic curve. For an ellipse, $B < 0$ and $R_o > 0$. For a parabola, $B = 0$ and $R_o > 0$. And lastly, a hyperbola can be characterized with a $B > 0$. Note that a circle is a special case of an ellipse and, thus, can be represented with similar variables.

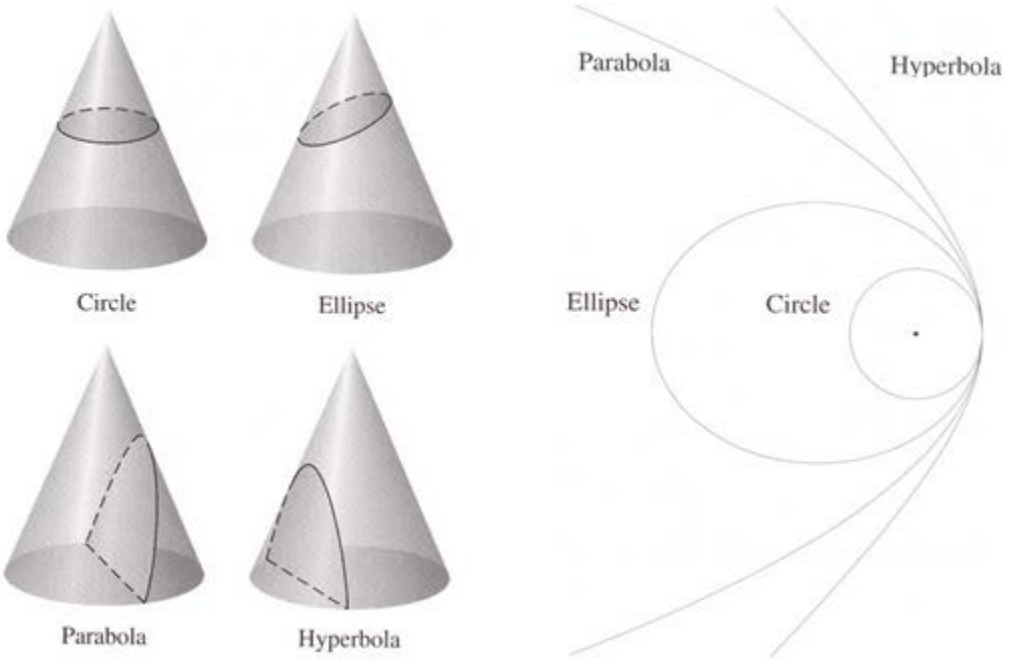

Figure 4.1 - Illustration of Conic Sections

A parabolic curved geometry was selected to analyze for this research. A two-dimensional axisymmetric parabolic geometrical configuration consists of a blunted nose that is symmetric about the horizontal axis. This type of geometry is also known as an ogive. Figure 4.2 depicts the parabolic configuration and various parameters that are used to describe the specific geometry. The nose radius (R_o) is the distance from tip of the nose (1) to the center of the horizontal and vertical axis (3). The length R is the distance from the center of the parabola (3) to any point along the surface of the ogive. θ represents the angle between the tangent at a point along the surface of the parabola and the horizontal axis. The geometry of the ogive can be varied by changing the length of the nose radius.

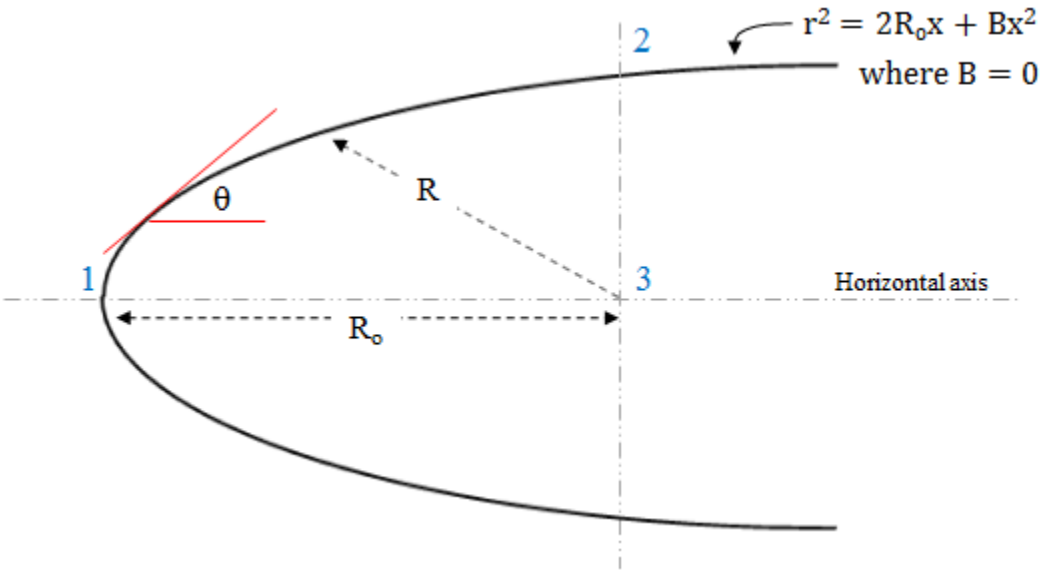

Figure 4.2 - Geometrical Representation of an Axisymmetric Paraboloid

A re-entry vehicle with an axisymmetric parabolic geometry will generate a detached bow shock wave ahead of the vehicle at hypersonic speeds. This type of configuration (as compared to a sharp nose geometry) reduces the heat transfer rates and permits for internal

heat conduction to occur, causing the body in hypersonic flow to approach thermal equilibrium. Blunt-nosed parabolic geometry has been utilized for various aerodynamics and ballistics applications, as it encompasses some of the many advantages associated with spherical shaped blunt-nosed geometries. For the purpose of this research, a parabolic blunt-nosed geometrical configuration with varied nose radius lengths will be examined.

4.2.3 Range of Velocity

With the selection of the geometrical configuration to analyze, the next step is to determine the range of freestream velocities to examine. The convective heating correlations will be valid for a range of freestream velocities or Mach numbers for the particular geometry discussed in the previous section. For this part of the design process, a nominal Space Shuttle trajectory data at the stagnation point was considered. The aerothermodynamic data from the entire trajectory were acquired and examined[18].

Since the maximum heating transfer rate will occur near the forward stagnation point, it is important to investigate the stagnation point heating rates for the Space Shuttle trajectory. The convective heating rates for the stagnation point are shown in the figure below against the Shuttle speed. As it can be seen, the heat transfer rates increase with higher velocities with the maximum heating rate occurring at approximately 23,000 ft/s. At lower velocities, the heat transfer rate at the stagnation point remains small. With an increase in velocity, the conversion of kinetic energy into heat significantly enlarges. The blue lines in the figure indicate the bounds of velocities chosen to examine, allowing applicable minimum and maximum heat transfer rates to be analyzed.

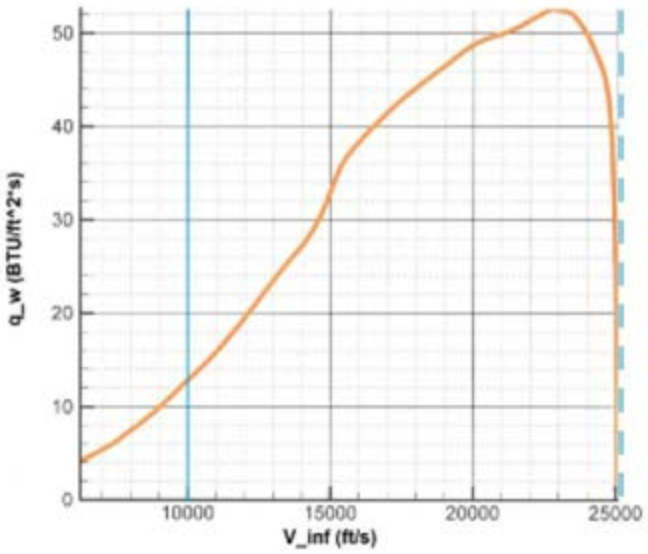

Figure 4.3 - Convective Heat Transfer Rate at the Stagnation Point for the Space Shuttle

The velocities and Mach numbers selected are more specifically listed in the equation below. This permits a freestream velocity range of 16,000 ft/s and Mach number variation of 14.3 to be studied. These values encompass both hypersonic and high-hypersonic flowfields and allow examination of heat transfer rates over a wide range of trajectory characteristics.

$$10,000\frac{ft}{s} \leq \textit{freestream velocity} \leq 26,000\frac{ft}{s}$$
$$9.0 \leq \textit{Mach number} \leq 23.3 \tag{4.2}$$

4.2.4 Laminar Versus Turbulent Flow

Laminar flow is described by the smooth streamlines that occur in parallel layers to the fluid flow without any disruption between each layer. The motion of the fluid particles is

organized and orderly in a laminar flow. Occurring at lower velocities, laminar flow does not display any cross streams in the direction perpendicular to the flow. Turbulent flow, however, is characterized by a disorderly flow regime that is dominated by eddies and lateral mixing. Fluid in turbulent flow experiences unstructured and chaotic motion, causing streamlines to be rough and discontinuous. Fourier's law of heat conduction states that the heat transfer on the surface of an object can be explained by the expression below,

$$q_w = -k_w \left(\frac{\partial T}{\partial y} \right)_w \tag{4.3}$$

where k_w describes the thermal conductivity of the gas at the wall and the term in the brackets represents the temperature gradient in the gas at the wall. The temperature gradient is computed from the boundary layer flowfield solution, which provides edge properties and wall conditions. Note that the negative sign in the equation denotes that the heat conduction occurs in the direction opposite of the temperature gradient[8]. Turbulent temperature gradients at the wall are significantly larger than laminar temperature gradients at the wall. Consequently, the turbulent heat transfer rates are considerably higher than laminar heat transfer rates, sometimes by a factor of ten. This is due to the complicated and unpredictable characteristics of the flow as it transitions to turbulent.

Although properties of real flows are often turbulent in nature, computing complex attributes of a turbulent flow is very difficult. Before attempting to calculate boundary layer transition and turbulence modeling, it is helpful to fully understand characteristics of laminar flow first. Accurate modeling and simulation of turbulent flow is a continuing research effort within the aerothermodynamics field. Eddies and mixing of the flow generated by turbulent flow is nearly impossible to solve analytically, as the complexity of the flow creates many unknowns. For this reason, the researcher will place emphasis on evaluating correlations for

laminar convective heating rates. This research can be extended for turbulent flow when more information is known regarding the turbulence phenomenon.

4.2.5 Gas Model

Various gas models were considered for this research, including a perfect gas model and an equilibrium air model. All three of these gas models can be utilized to examine a hypersonic flowfield. A thermally perfect gas denotes that the gas in the system is non-reactive. The thermodynamic properties of a thermally perfect gas can be evaluated using the ideal gas equation of state described below,

$$p = \rho RT = p\left(\frac{R}{c_p}\right)h \tag{4.4}$$

where R represents the gas constant and c_p describes the specific heat at constant pressure. This approximation is used to study the behavior of gases under many conditions. There exist many limitations to the ideal gas law. Beyond temperatures of 3600 °R, the dissociation of the diatomic oxygen molecules starts to occur and causes the air to become chemically reactive. As the speed of the vehicle begins to increase and approach re-entry speeds, the assumption of an ideal gas becomes less acceptable[6].

Equilibrium air model assumes that the gas in the system is chemically reactive. For this theory, one particular temperature can be utilized to describe all of the different energy modes of all molecules and this temperature is equivalent to the temperature of the surroundings. Additionally, this model assumes that all of the chemical reactions are finished and in balance. Thus, the system will not experience any variation in chemical composition.

This model is a way to represent real-gas effects that result due to extremely high temperatures in hypersonic flow, and is known as a thermodynamic equilibrium.

In the method developed by Lester Lees, a perfect gas chemistry is assumed. The correlations for laminar heat transfer over blunt-nosed bodies derived by Lees are valid for a perfect gas chemistry[3]. Similarly, a perfect gas chemistry will also be assumed for this project since the analytical method selected for this research was by Lees. A method to evaluate the heat transfer rates over a parabolic shaped geometry for a perfect gas must first be developed. The method can then be extended to include equilibrium air chemistry. It is important to understand the behavior of the flow under the assumption of an ideal gas before accounting for real-gas effects within the system.

Chapter 5

Analysis and Design

This chapter details the process for the development of the stagnation point heating correlation and the non-dimensionalized laminar convective heating relations for a parabolic shaped geometrical configuration. The motivation behind the project will first be discussed under the analysis section of the chapter. Afterwards, the derived method will be presented in the design section.

5.1 Analysis

5.1.1 Ogive Geometry

Within the method developed by Lees, geometrical configurations with a hemispherical nose are examined. A hemispherical shape denotes that the radius of the nose will remain unchanged throughout the geometry. At any angle between the radius vector and the flight direction, the radius length will be the same. The figure below illustrates this concept. From the illustration, it can be seen that the length of the line from the center of the hemisphere to any location on the outer edge are equivalent. A symmetrical configuration, such as that of a hemisphere, significantly simplifies the equations representing the geometry.

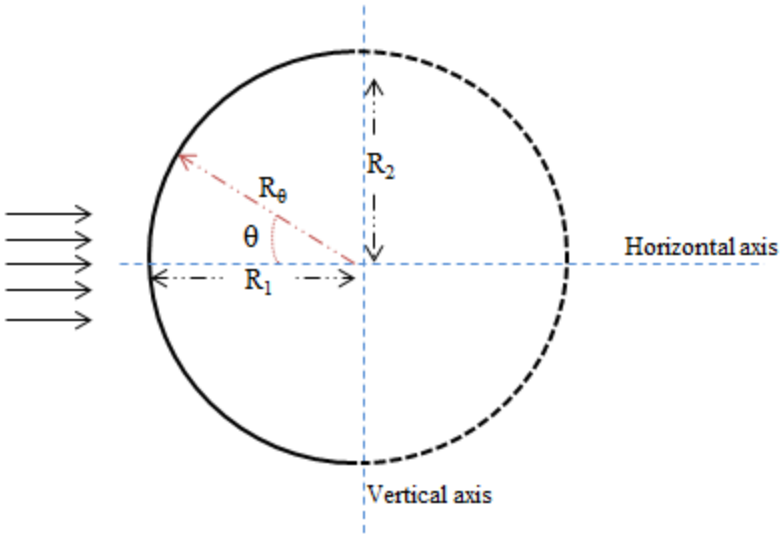

Figure 5.1 - Illustration of Hemispherical Nose Geometry

A parabolic shaped nose is a more complex geometrical configuration. An illustration of a parabolic shaped geometry can be seen below. It should be noted that the radius lengths vary at different points along the geometry. The nose radius is measured from the center of the ogive to the outer edge of the nose. A unique radius length exists at each location along the surface of the geometry. With a more intricate nose configuration, representing the geometry requires more effort. However, studying the heating distribution along the surface of an ogive in a more simplified manner can be extremely beneficial. Ogive shaped configurations are commonly utilized in aerodynamics and ballistics applications.

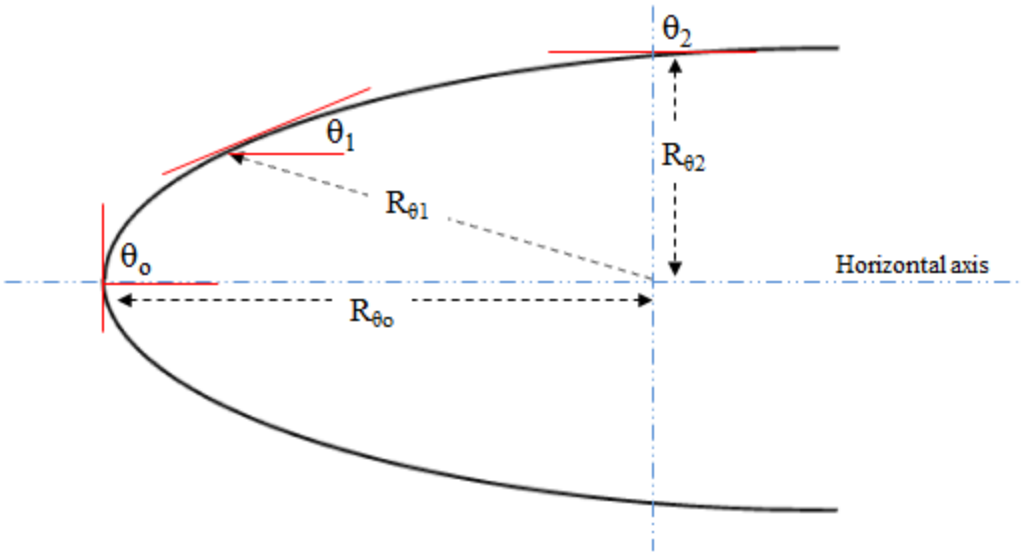

Figure 5.2 - Illustration of a Parabolic Nosed Geometry

Many analytical methods of computing heat transfer rates for blunt-nosed geometries are discussed in Section 3.3. However, an analytical technique of evaluating the heating distribution for a parabolic shaped configuration does not exist. Thus, one of the inspirations for this research is to establish a set of simplified correlations, similar to those developed by Lester Lees, that can compute the heating distribution over an ogive. Furthermore, this project can provide engineers and students a less-demanding way of approximating the laminar convective heat transfer rates over a blunt parabolic-nosed body in a hypersonic flowfield. This method can be utilized during the earlier phases of design without requiring high-performance computers and saving cost and time associated with such systems. The ability to alter geometrical parameters will be incorporated within the method.

5.1.2 Motivation for Non-dimensional Heating Correlations

One of the most important aspects of the technique developed by Lester Lees was the form of the correlation used to describe the surface heat transfer rate distribution. The laminar convective heating rate was defined in a non-dimensional form by simplifying the relation as a ratio of the local heat transfer rate to the heat transfer rate at the stagnation point,

$$\frac{\dot{q}_w}{(\dot{q}_w)_o} \tag{5.1}$$

Setting up the heat transfer rate in this form allows eliminating various parameters within the correlations. Additionally, it allows comparison of surface heating distribution for various geometries and Mach numbers within one figure. One of the figures included in Lees' paper displaying the laminar heat transfer rate over a hemispherical nose is shown below[3]. Note that the computations were made assuming the temperature outside the boundary layer is much larger than the temperature near the surface of the blunt-nosed body. The y-axis displays the relation described in Equation 5.1 and the x-axis describes the angle between the radius vector and the flight direction. The x-axis increases from an angle of 0°, the forward stagnation point of the hemisphere at the nose to an angle of 90°.

The surface heat transfer rates for the hemispherical-nosed body follow a similar trend, varying slightly with an increase in Mach number. However, when hypersonic speeds are considered (M > 5), the surface heat transfer rate curves appear to be independent of Mach number. This indicates that at hypersonic speeds, the heat transfer distribution along the surface can be represented using one curve. The curve initiates with the highest heat transfer rate at the stagnation point and gradually decreases as the flow moves further away from the stagnation point.

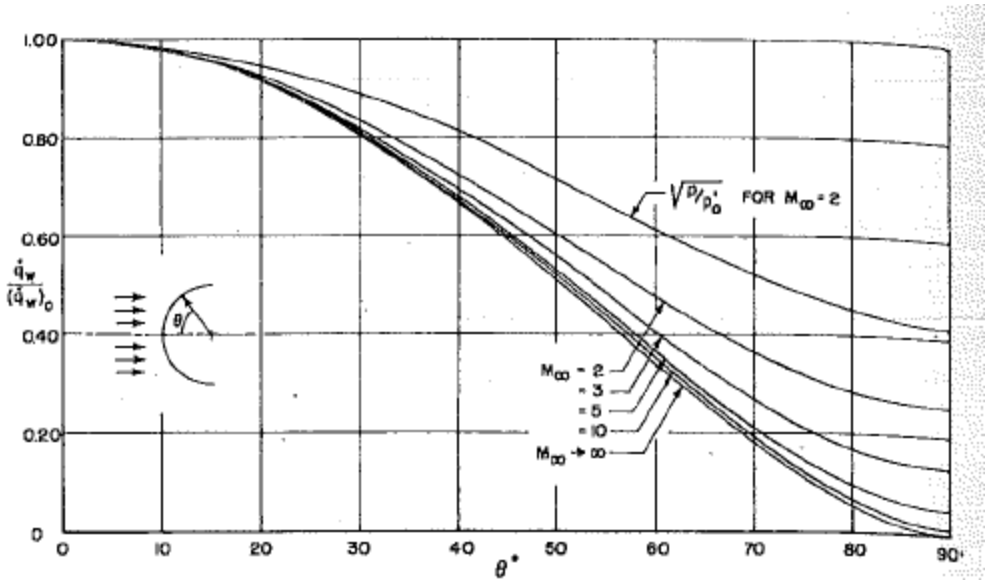

Figure 5.3 - Laminar Heat Transfer Rate over a Hemispherical Nose for (T_w/T_e) << 1

A blunt cone with a spherical nose was another geometry studied by Lees[3]. The heat transfer ratio along the surface of the body is shown in Figure 5.4 below. The y-axis represents the surface heat transfer ratio and the x-axis displays the distance along the surface in a non-dimensional form (s/R_n). The curve on the left describes the heat transfer rate along the spherical nose cap while the right side of the plot displays the distribution of the heat transfer rate for various cone half angles. Note that these relations are independent of the freestream Mach number. As stated earlier, the heat transfer ratio can be described with a single curve at true hypersonic speeds. In this case, the relation ($M_\infty \sin\boldsymbol{\theta}_c$) >> 1 denotes that the body is in a hypersonic flowfield.

Thus, the objective of this research is to develop a set of correlations that can describe the heat transfer rates along the surface of an ogive using one curve fit model. Motivated by Lees' method, it is desired by the researcher to establish these relations (assuming a perfect

gas chemistry) based on the geometrical parameters and independent of freestream conditions, including Mach number.

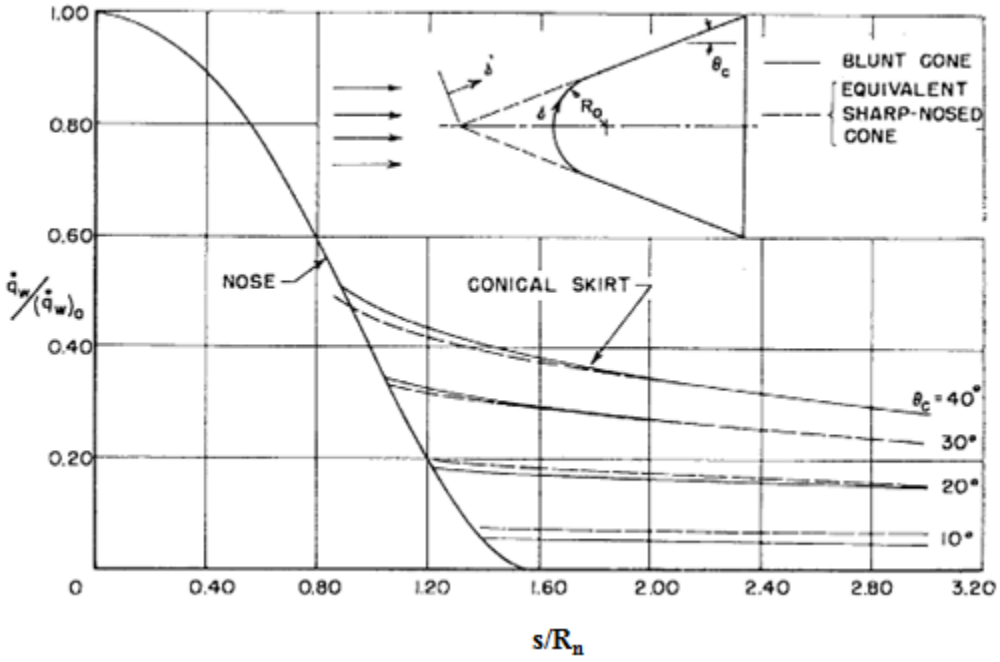

Figure 5.4 - Laminar Heat Transfer Rate over a Blunt-nosed Cone for $(T_w/T_e) << 1$ and $(M_\infty \sin\theta_c) >> 1$

5.2 Design

The remainder of this chapter will document the method utilized by the researcher to develop the set of correlations for the evaluation of the convective laminar surface heat transfer rate for a parabolic shaped geometry.

5.2.1 Representation of the Geometry

In the previous section, discussion was provided regarding the differences between hemispherical and parabolic shaped nose geometries. In order to analyze the heat transfer rate over the surface of the ogive, the geometric relations must be derived first. An illustration of the ogive shape can be seen below in Figure 5.5. Note that the x-axis is defined by the variable “x” and the y-axis is defined by the parameter “r”. Additionally, “s” is the distance along the body surface (measured from the forward stagnation point) and “θ” is the angle between the line tangential to the parabola and the horizontal axis at a particular point along the surface.

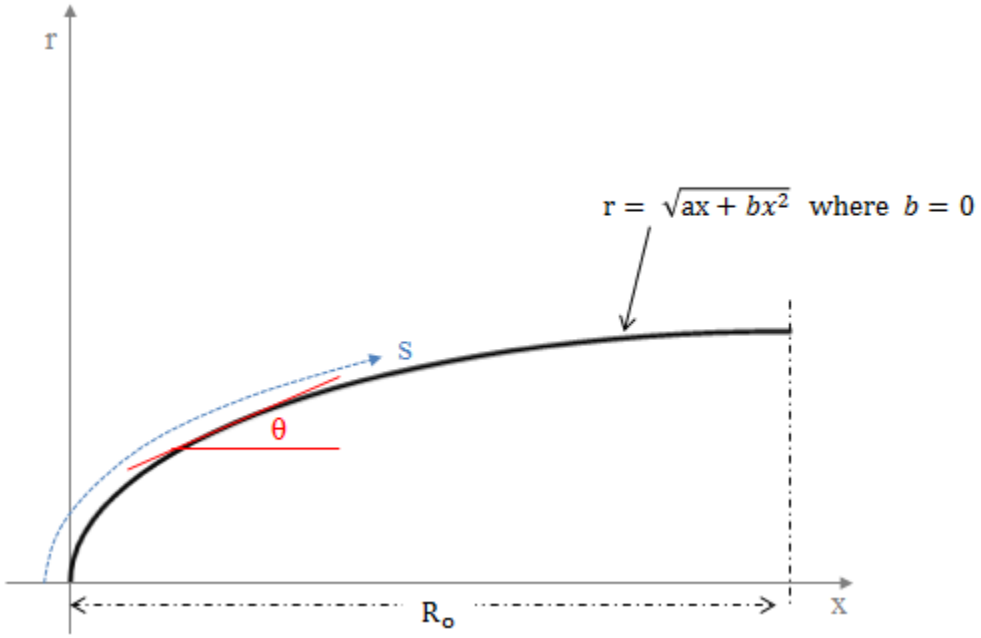

Figure 5.5 - Graphical Representation of the Ogive

The general conic equation is defined as,

$$r^2 = ax + bx^2 \tag{5.2}$$

$$\text{where} \begin{cases} b < 0 \text{ and } a > 0 & \text{ellipsoid} \\ b < 0 \text{ and } a > 0 & \text{paraboloid} \\ b > 0 & \text{hyperboloid} \end{cases}$$

Therefore, the equation for the case of the ogive can be simplified as,

$$r = \sqrt{ax} \tag{5.3}$$

A graphical depiction of the angle between the horizontal and the line tangent to the surface (shown in red in Figure 5.5) is depicted in Figure 5.6. This angle can be written as,

$$\tan(\theta) = \frac{dr}{dx} \tag{5.4}$$

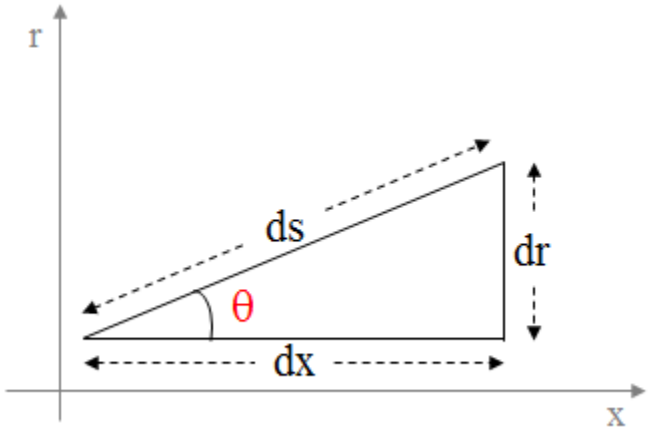

Figure 5.6 - Illustration of Tangential Angle

To avoid presenting an abundance of information and derivations, the complete analysis of the geometric relations is shown in Appendix A. The entire process of obtaining the below correlations is detailed in the appendix. The expression for "R", the radius length at any point along the surface of the ogive, was determined as,

$$\frac{1}{R} = \frac{\frac{a^2}{4}}{\left[r^2 + \frac{a^2}{4}\right]^{3/2}} \tag{5.5}$$

Using the boundary condition when r = 0 and R = R_o, the following relationship between R_o and a was obtained,

$$a = 2R_o \tag{5.6}$$

Furthermore, the derivative of "s" with respect to "r" for the ogive geometry was evaluated to be,

$$\frac{ds}{dr} = \sqrt{\left(\frac{dx}{dr}\right)^2 + 1} = \sqrt{\frac{r^2}{R_o^2} + 1} \tag{5.7}$$

Using the above expressions, the ogive geometry can be represented using various parameters. These relations will be utilized in the next section to evaluate the heat transfer rate at the stagnation point and at any location along the surface of the ogive.

5.2.2 Evaluation of the Stagnation Point Heat Transfer Rate

This section will cover the development of the stagnation point heat transfer rate. For the case of the blunted-nose geometry, particularly an ogive shaped configuration, the heat

transfer rate will be at a maximum at the forward stagnation point. Thus, the heat transfer rate at the forward stagnation point is necessary to evaluate so that the heat transfer rate quantity can be represented in a non-dimensional form.

As described by Lester Lees, the surface heat transfer rate can be described using the below expression. Some of the initial derivations are excluded within the analysis for redundancy purposes, as they can be referred to in Lees' journal article titled *Laminar Heat Transfer Over Blunt-Nosed Bodies at Hypersonic Flight Speeds*[3].

$$\dot{q}_w \cong 0.50\left(\overline{\mathrm{Pr}}\right)^{-2/3}\sqrt{\left(\rho_e\mu_e\right)_0}\sqrt{u_\infty}h_{se}\cdot F(s) \tag{5.8}$$

where Pr represents the average Prandtl number, ρ_e describes the gas density at the edge of the boundary layer, μ_e is the absolute viscosity at edge, u_∞ is the freestream velocity, h_{se} represents the total enthalpy at the edge, and the expression for F(s) is shown below.

$$F\left(s\right)=\frac{\left(\frac{1}{\sqrt{2}}\right)\left(\frac{p}{p_0'}\right)\left(\frac{\omega_e}{\omega_{e0}}\right)\left(\frac{u_e}{u_\infty}\right)r_0^k}{\left[\int_0^s\left(\frac{p}{p_0'}\right)\left(\frac{\omega_e}{\omega_{e0}}\right)\left(\frac{u_e}{u_\infty}\right)r_0^{2k}ds\right]^{1/2}} \tag{5.9}$$

In the above equation, P describes the static pressure, r_o is the radius of the cross section for a body of revolution, and s represents the distance along the surface of the body measured from the forward stagnation point (where k = 0 for a planar body and k = 1 for a body of revolution). The subscript e denotes the edge of the boundary layer, 0 symbolizes the forward

stagnation point, and ∞ indicates the freestream conditions. The expression for ω_e is provided below,

$$\omega_e = \frac{\mu_e}{\mathbb{R}_e T_e} \tag{5.10}$$

where R denotes the specific gas constant and T is the absolute temperature. Equation 5.8 allows computing the heat transfer rate at any point along the surface of the geometry. However, it is important to first derive a relation for the heat transfer rate specifically at the forward stagnation point. As given by Lees, the heat transfer rate at the forward stagnation point for any blunted-nose geometrical configuration can be determined by the following expression. Equation 5.11 is a simplified version of Equation 5.8. Using Equation 5.11, a correlation for the heat transfer rate at the stagnation point for an ogive configuration will be developed. The remainder of this section will focus on deriving this correlation.

$$\dot{q}_{w,0} \cong 0.50 \cdot 2^{k/2} \left(\overline{\mathrm{Pr}}\right)^{-2/3} \sqrt{\left(\rho_e \mu_e\right)_0} \sqrt{u_\infty} \cdot h_{se} \cdot \frac{\sqrt{\left[\left(\frac{R}{u_\infty}\right)\left(\frac{du_e}{ds}\right)\right]_{s=0}}}{\sqrt{R_0}} \tag{5.11}$$

Since the ogive configuration signifies a planar body with a blunted-nose, “k” will be zero in the above equation. Thus, the following simplification can be implemented into Equation 5.11,

$$2^{k/2} \approx 1 \tag{5.12}$$

Next, it is necessary to evaluate the differential in Equation 5.11 for the case of the ogive. This requires determining the derivative of the velocity in the x-direction (at the edge of the boundary layer) with respect to “s” at the forward stagnation point (s = 0). In order to

compute the derivative, the Euler equations must be examined. The momentum equation states that,

$$\rho_e u_e \frac{du_e}{ds} = -\frac{dp}{ds} \tag{5.13}$$

By rearranging the above equation, it is possible to evaluate the velocity derivative at the edge of the boundary layer. However due to the symmetry in the geometry of an ogive, the derivative of the pressure term (dp/ds) at the stagnation point will result in a zero. This would yield a zero for the velocity derivative (du_e/ds) at the stagnation point as well. For this reason, the momentum equation must be differentiated with respect to "s" as follows,

$$\frac{d}{ds}\left(\rho_e u_e \frac{du_e}{ds} = -\frac{dp}{ds}\right) \tag{5.14}$$

Completing the above differentiation provides,

$$\rho_e\left[\frac{du_e}{ds}\cdot\frac{du_e}{ds} + u_e\frac{d^2u_e}{ds^2}\right] + \frac{d\rho_e}{ds}\cdot u_e\frac{du_e}{ds} = -\frac{d^2p}{ds^2} \tag{5.15}$$

At the forward stagnation point, the velocity at the edge of the boundary layer is stagnant ($u_e = 0$). This simplifies the above equation to,

$$\rho_{e,0}\left(\frac{du_e}{ds}\right)_0^2 = -\left(\frac{d^2p}{ds^2}\right)_0 \tag{5.16}$$

Rearranging the equation to solve the velocity derivative yields Equation 5.17. The technique of non-dimensionalization is often used in aerodynamics. By representing quantities in a non-dimensional form, the parameters in the study can be simplified by relating them to the

freestream conditions. This method was applied to Equation 5.17 to determine the derivative of the velocity ratio as described in Equation 5.18.

$$\left(\frac{du_e}{ds}\right)_0 = \sqrt{-\frac{1}{\rho_{e,0}}\left(\frac{d^2p}{ds^2}\right)_0} \tag{5.17}$$

$$u_\infty\left(\frac{d\left(u_e/u_\infty\right)}{ds}\right)_0 = \sqrt{-\frac{p_\infty}{\rho_{e,0}}\left(\frac{d^2\left(p/p_\infty\right)}{ds^2}\right)_0} \tag{5.18}$$

To compute the pressure derivative in Equation 5.17, the modified Newtonian law was utilized. The modified Newtonian law provides a relation for the pressure ratio (P/P_∞) for any point along the surface of a blunted-nose body. The pressure along the surface of the geometry is non-dimensionalized by relating the quantity to the freestream condition. By differentiating the pressure ratio twice, the second derivative of pressure at the stagnation point can be evaluated. The process of deriving an expression for $[d^2(P/P_\infty)/ds^2]$ is detailed in Appendix B. Refer to the appendix for the complete analysis. Note that the pressure derivative was determined as a non-dimensional pressure ratio quantity. This form was used so that the quantity can be substituted into the non-dimensionalized expression described in Equation 5.18.

The following expression was derived as the second derivative of the pressure ratio,

$$\left(\frac{d^2\left(p/p_\infty\right)}{ds^2}\right)_0 = \frac{-8}{a^2}\cdot\left(\frac{p_{0,2}}{p_\infty}-1\right) \tag{5.19}$$

Substituting Equation 5.19 into Equation 5.18 yields the following expression,

$$u_\infty \left(\frac{d\left(u_e / u_\infty \right)}{ds} \right)_0 = \sqrt{-\frac{p_{0,2}}{\rho_{e,0}} \left[-\frac{8}{a^2} \left(1 - \frac{p_\infty}{p_{0,2}} \right) \right]} \tag{5.20}$$

In the above equation, $P_{o,2}$ denotes the stagnation pressure behind the shock wave. To further simplify the expression for the velocity ratio, it is necessary to express the conditions at the stagnation point in terms of geometric parameters and Mach number. In order to do this, the equation of state will be studied. The equation of state says that,

$$P = \rho RT \tag{5.21}$$

Since temperature does not change across a shock wave for an adiabatic wall, the temperature behind the shock wave will be the same as the temperature at the stagnation point. Implementing this assumption generates the following,

$$p_{0,2} = \rho_{e,o} R T_0 \tag{5.22}$$

Next to evaluate an expression for the stagnation point temperature, the conservation of energy equation will be examined. The energy equation states that,

$$C_p T_\infty + \frac{u_\infty^{\,2}}{2} = C_p T_0 \tag{5.23}$$

where T indicates the absolute temperature at a specific location (denoted by the subscript). Dividing the entire equation by $C_p T_\infty$ produces Equation 5.24. Substituting the relationship

between freestream velocity and ratio of specific heats described in Equation 5.25 into the energy equation yields a correlation for the stagnation point temperature.

$$1+\frac{u_\infty{}^2}{2C_pT_\infty}=\frac{T_0}{T_\infty} \tag{5.24}$$

$$\frac{u_\infty{}^2}{C_pT_\infty}=(\gamma-1)M_\infty{}^2 \tag{5.25}$$

$$T_0=T_\infty\left(1+\frac{(\gamma-1)}{2}M_\infty{}^2\right) \tag{5.26}$$

Substituting Equation 5.26 into Equation 5.22 develops the following expression. Implementing this formulation into the velocity derivative described in Equation 5.20 produces Equation 5.28.

$$\frac{p_{0,2}}{\rho_{e,0}}=RT_\infty\left(1+\frac{(\gamma-1)}{2}M_\infty{}^2\right) \tag{5.27}$$

$$\left(\frac{d\left(u_e/u_\infty\right)}{ds}\right)_0=\sqrt{-\left[\frac{RT_\infty}{u_\infty{}^2}\right]\left[1+\frac{(\gamma-1)}{2}M_\infty{}^2\right]\left[\frac{-8}{a^2}\cdot\left(1-\frac{p_\infty}{p_{0,2}}\right)\right]} \tag{5.28}$$

Since R can be written as ($R = V_{sound}{}^2/(\gamma \cdot T_\infty)$) and Mach number can be expressed as ($M_\infty = u_\infty/V_{sound}$), the following simplification can be made to the first term in the root.

$$\frac{RT_\infty}{u_\infty{}^2}=\frac{V_{sound}^2}{\gamma u_\infty{}^2}=\frac{1}{\gamma M_\infty{}^2} \tag{5.29}$$

$$\frac{p_\infty}{p_{0,2}} = \frac{1}{\gamma M_\infty^{\,2}} \tag{5.30}$$

Lester Lees applies the above approximation for ($P_\infty/\rho_{0,2}$) within his derivation of surface heat transfer rates for flows traveling at hypersonic speeds[3]. Dr. Fred DeJarnette advised that this was a reasonable approximation to make for the purpose of this research. Thus, Equation 5.30 was also used in the development of this method. Replacing the first term in the root with Equation 5.29 and implementing the above approximation generates the resulting expression for the velocity derivative at the stagnation point,

$$\left(\frac{d\left(u_e/u_\infty\right)}{ds}\right)_0 = \sqrt{-\left[\frac{1}{\gamma M_\infty^{\,2}}\right]\left[1+\frac{(\gamma-1)}{2}M_\infty^{\,2}\right]\left[\frac{-8}{a^2}\cdot\left(1-\frac{1}{\gamma M_\infty^{\,2}}\right)\right]} \tag{5.31}$$

Note that in the above equation for the case of the ogive, all parameters are a function of the geometry or the freestream Mach number. This reduces the relation significantly by eliminating any additional variables that may otherwise need to be calculated. In order to further simplify the computation of the heat transfer rates over the surface of the ogive, the heating distribution will be expressed in a non-dimensional form. This non-dimensional form will eliminate additional parameters that still exist in Equation 5.11 for the stagnation point heating. The next section of this chapter will detail the process of developing non-dimensionalized heat transfer rate correlations.

5.2.3 Development of the Non-dimensionalized Heat Transfer Rate

This section will document the process of developing a non-dimensional form of the heat transfer rate. Now that a part of the stagnation point heating rate has been simplified, the

remainder of the relation will be streamlined by relating it to the surface heat transfer rate. The heating distribution for an ogive can be simplified by dividing Equation 5.8 by Equation 5.11 and non-dimensionalizing the velocity derivative,

$$\frac{\dot{q}_w}{\dot{q}_{w,0}} = \frac{\sqrt{R_0}\cdot F(s)}{\sqrt{\left[\left(\frac{R}{u_\infty}\right)\left(\frac{du_e}{ds}\right)\right]_{s=0}}} = \frac{\sqrt{R_0}\cdot F(s)}{\sqrt{\left[R\cdot\left(\frac{d\left(u_e/u_\infty\right)}{ds}\right)\right]_{s=0}}} \tag{5.32}$$

Substituting expression derived in the previous section for the velocity ratio into the non-dimensional heat transfer rate generates,

$$\frac{\dot{q}_w}{\dot{q}_{w,0}} = \frac{F(s)}{\sqrt{-\left[\frac{1}{\gamma M_\infty{}^2}\right]\left[1+\frac{(\gamma-1)}{2}M_\infty{}^2\right]\left[\frac{-8}{a^2}\cdot\left(1-\frac{1}{\gamma M_\infty{}^2}\right)\right]}} \tag{5.33}$$

Note that the radius (R) at the stagnation point is the nose radius of the ogive (R_o) and therefore, it can be eliminated from the expression. Additionally, the expression for F(s) can also be simplified by making the assumption that ($\omega_e \cong \omega_{e,o}$) due to the slow deviation of the quantity at high enthalpies.

$$F(s) = \frac{\left(\frac{1}{\sqrt{2}}\right)\left(\frac{p}{p_{0,2}}\right)\left(\frac{u_e}{u_\infty}\right)}{\left[\int_0^s\left(\frac{p}{p_{0,2}}\right)\left(\frac{u_e}{u_\infty}\right)ds\right]^{1/2}} \tag{5.34}$$

Replacing (ds) in the equation with the expression derived in Appendix A for (dθ) yields,

$$F(\theta) = \frac{\left(\frac{1}{\sqrt{2}}\right)\left(\frac{p}{p_{0,2}}\right)\left(\frac{u_e}{u_\infty}\right)}{\left[\int_{90}^{\theta} -\left(\frac{p}{p_{0,2}}\right)\left(\frac{u_e}{u_\infty}\right)\frac{a}{2\sin^3\theta}\,d\theta\right]^{1/2}} \tag{5.35}$$

Using the modified Newtonian law and the approximation described in Equation 5.30, the pressure ratio and velocity profile can be written as,

$$\frac{p}{p_{0,2}} = \sin^2\theta + \frac{1}{\gamma M_\infty{}^2}\cos^2\theta \tag{5.36}$$

$$\frac{u_e}{u_\infty} = \sqrt{\left[1 + \frac{1}{M_\infty{}^2}\cdot\left(\frac{2}{\gamma - 1}\right)\right]\left[1 - \left(\frac{p}{p_{0,2}}\right)^{\frac{(\gamma-1)}{\gamma}}\right]} \tag{5.37}$$

At each point along the surface of the ogive, there exists a unique angle tangential to the geometry. At the stagnation point, θ equates to 90 degrees. Note that the integral in Equation 5.35 starts at 90° and ends at 0°, unlike the coordinate system used by Lees. The expression F(s) was converted to F(θ) due to the reason that both the pressure ratio and the velocity ratio are expressed in terms of θ. Refer to the figure below for a visual representation of the angle tangential to the surface at the stagnation point and at several other locations. Note that θ_1 is approximately at 45° and θ_2 is at a point parallel to the horizontal axis (0°).

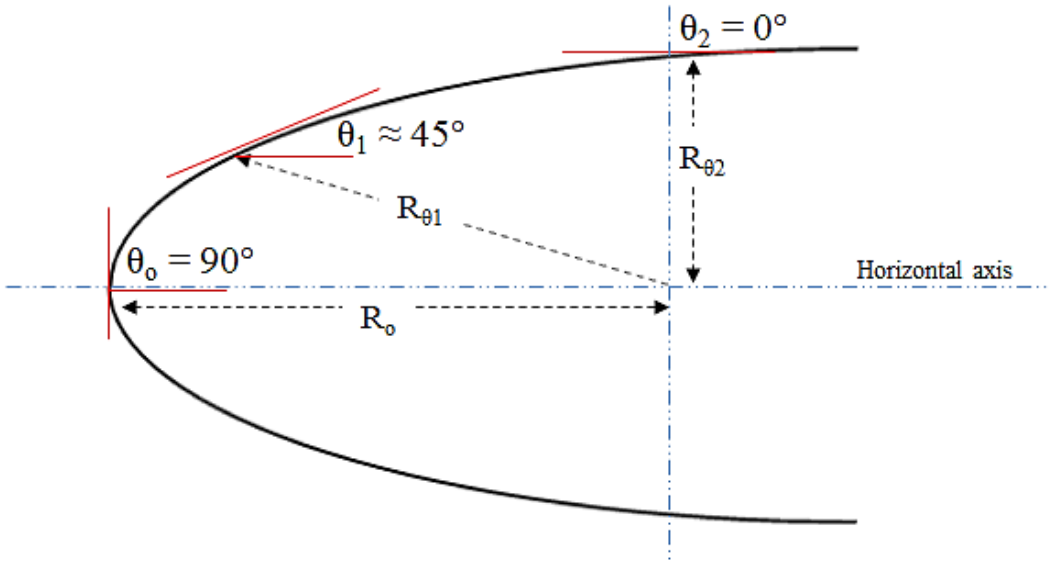

Figure 5.7 - Illustration of Angles Tangential to the Surface

However, the integration of the product of the terms in the denominator creates complications. The relations for the pressure and velocity ratios are very difficult to integrate individually. Multiplying the correlations together, as required by the expression for F(s), further challenges this issue of integration. Many methods were examined to evaluate an expression for the denominator of F(s); however, none of the techniques applied to determine an analytical solution to the integral proved practical.

For this reason, a numerical approximation was perused to evaluate a solution to the integral at each point along the surface of the ogive. The objective of this research is to develop a simpler method to evaluating the heat transfer rate over the surface of a parabolic geometry. With this goal in mind, it was necessary to utilize a simple numerical technique to approximate the integral. The trapezoidal rule was selected as the method of numerical

integration due to the simplicity in the process, allowing undergraduate students to easily employ the method developed. The trapezoidal rule states that,

$$\int_a^b f(x)dx \approx (b-a)\left[\frac{f(a)+f(b)}{2}\right] \tag{5.38}$$

Applying the trapezoidal rule to evaluate the denominator of F(s) provides,

$$\int_{\theta_1}^{\theta_2} f(\theta)d\theta \approx (\theta_2-\theta)_1\left[\frac{f(\theta_1)+f(\theta_2)}{2}\right] \tag{5.39}$$

The implementation of the trapezoidal rule approximation to evaluate the heat transfer rate will be discussed in 5.2.5. The next section will document the evaluation of the parameter "s" that computes the distance along the ogive surface (from the stagnation point).

5.2.4 Evaluation of Surface Distance Parameter

As can be seen, the coordinate system selected for the ogive geometry is particular to this method. Lees utilized a slightly different coordinate scheme, where the parameter θ represented the angle between the flight direction and the radius vector located at the center of the nose. For the case of the paraboloid, the parameter θ is defined by the angle between line tangential to the surface and the radius vector. Refer to Figure 5.5 for a visual representation of the coordinate system.

Additionally, it is important to relate the angle θ to the actual distance along the surface from the radius vector. The distance from the nose of the ogive to a point along the surface will be defined by the parameter "s". In order to establish a relationship between θ and s, the expression for (ds/dθ) will be examined. By integrating the expression for (ds/dθ) (shown Equation B.10), the following formulation can be found.

$$s = -\frac{a}{2}\left[\frac{1}{8}\left(-\csc^2\left(\frac{\theta}{2}\right)+\sec^2\left(\frac{\theta}{2}\right)+4\log\left(\sin\left(\frac{\theta}{2}\right)\right)-4\log\left(\cos\left(\frac{\theta}{2}\right)\right)\right)\right]+\mathcal{C} \quad (5.40)$$

The variable $\mathcal{C}$ represents the constant of integration. The constant can be determined by using the boundary condition when (s = 0 and r = 0), the angle tangential to the surface will be orthogonal to the flight direction. This occurs at the stagnation point where the angle θ is equivalent to (π/2) or 90°. Refer to Figure 5.8 below for a visual representation of this boundary condition. Implementing this boundary condition into Equation 5.40 results in the following,

$$0 = -\frac{a}{2}\left[\frac{1}{8}\left(-2+2+4\log\left(\frac{1}{\sqrt{2}}\right)-4\log\left(\frac{1}{\sqrt{2}}\right)\right)\right]+\mathcal{C} \quad (5.41)$$

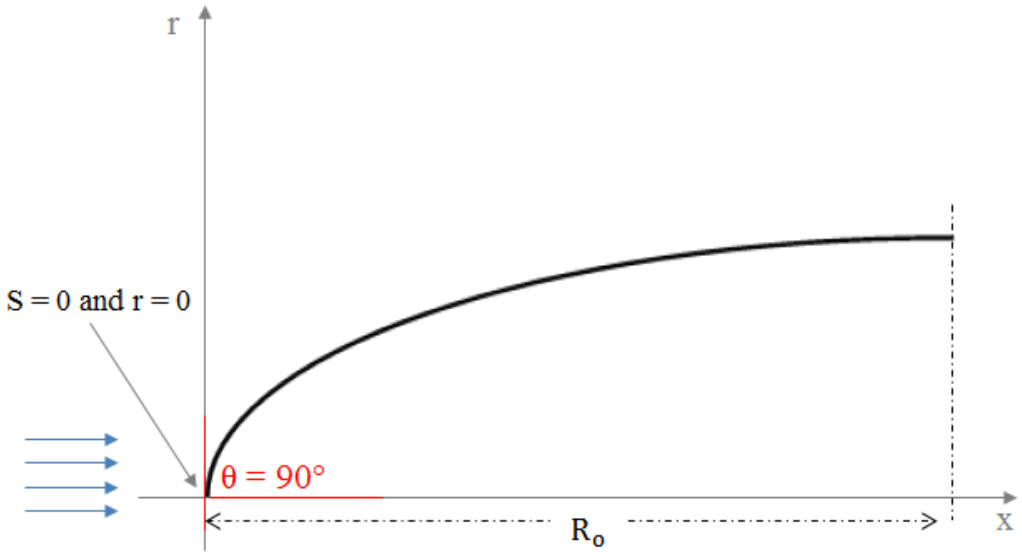

Figure 5.8 - Illustration of the Stagnation Point Boundary Condition

Thus, the constant of integration is evaluated to be ($\mathbb{C} = 0$). Substituting this into Equation 5.40 provides a relation for the surface distance along the paraboloid (s) as a function of the tangential angle (θ).

$$s(\theta) = -\frac{a}{16}\left[-\csc^2\left(\frac{\theta}{2}\right) + \sec^2\left(\frac{\theta}{2}\right) + 4\log\left(\sin\left(\frac{\theta}{2}\right) - \cos\left(\frac{\theta}{2}\right)\right)\right] \qquad (5.42)$$

This expression can be useful when describing the surface heat transfer rate along the surface of the geometry. The distance along the surface can be simply explained in terms of the geometrical parameters. The nose radius length of the ogive is incorporated within the relation above ($a = R_o$).

5.2.5 Implementation in MATLAB

As described in Section 4.1, one of the project requirements set by the user is the implementation of the method with a commonly used programming language. Several programs with numerical computing capabilities were considered. MATLAB was ultimately chosen as the computer program to apply the method developed. This section will cover the process of using MATLAB as a tool to compute the surface heat transfer rates over the surface of the ogive.

When writing a program to compute calculations, it is important to define the input parameters at the beginning. This allows the user to modify any of the parameters without altering the body of the code. These input variables can be pertaining to the flow field or the particular geometry within the study. For the purpose of modeling the heat transfer rates over a paraboloid, various parameters were specified. Table 5.1 lists all of the input parameters that were encoded into the MATLAB program. Note that the speed of sound is dependent on the altitude of the vehicle. To determine the speed of sound at various altitudes, refer to the 1972 U.S. Standard Atmosphere[26].

Table 5.1 - Input Parameters for MATLAB Implementation

Input Parameter	Definition	Value(s) Implemented
gamma (γ)	Ratio of specific heats (C_p/C_v)	1.4
V_sound	Speed of sound (ft/s)	(dependent on altitude)
Mach	Mach number	9.0 - 24.0
Ro	Nose radius of paraboloid (ft)	0.5, 1, 5, 10

The next step of the process involves generating the paraboloid geometry within MATLAB. It is important to select the coordinate system and axis before creating the geometrical shape. For consistency purposes, the ogive shaped geometry will be plotted with variables “x” and “r” (similar to Figure 5.5). Geometrical relations derived in Section 5.2.1 were utilized to create a blunted-nose parabolic configuration. The figure below illustrates the paraboloid geometry with a nose radius of 0.1 feet. Note the blunted nose of the paraboloid at the stagnation point. Further downstream of the stagnation point, the paraboloid will eventually become parallel to the horizontal axis.

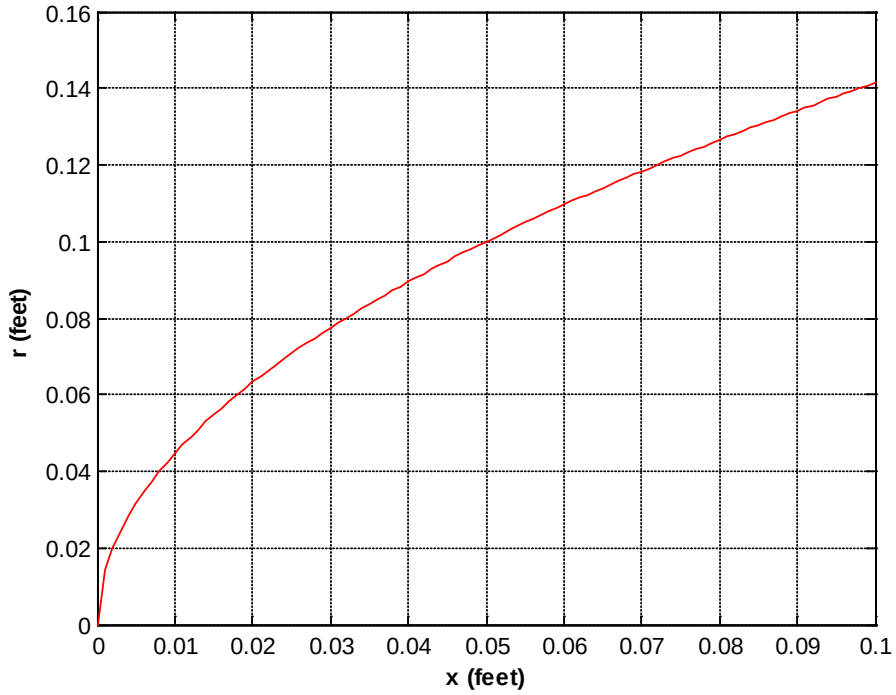

Figure 5.9- Graphical Representation of a Paraboloid with a Nose Radius of 0.1 feet

The next step is to implement the equations derived in Sections 5.5.2 and 5.2.3. Before the correlation for the non-dimensional heat transfer rate can be applied, the equation for F(s)

must be programmed using the trapezoidal rule. The numerator of F(s) must be evaluated at each variation of θ. Since an integration requires summing the area under the curve, the denominator must be evaluated at each variation of θ as well using the trapezoidal rule described in Equation 5.39. As θ varies from 90° to 0°, the quantity of the denominator (computed using the Equation 5.39) must be added to the quantity evaluated at the previous θ angle. This will complete the integration required by the F(s) expression in Equation 5.35. Once an array of computed F(s) is generated, the non-dimensional heat transfer rates at each point along the surface can be determined. Equation 5.33 provides the correlation for evaluating the non-dimensional heat transfer rates.

Once the correlations for evaluating the non-dimensional heating rates have been coded, the program can be operated at various freestream conditions. To demonstrate the implementation of the heating rates in MATLAB, Mach numbers of 5, 10, and 20 have been inputted into the program. The figures below describe the non-dimensional surface heat transfer rates for a paraboloid with a nose radius of 0.1 feet. Note the legend indicating the different Mach numbers in the figures. Figures 5.10 and 5.11 illustrate that for Mach numbers greater than 5, the curve describing the heat transfer rates along the surface remains nearly unchanged. This is valid for surface locations defined as both the angle tangential to the surface (θ) and the non-dimensional surface location (S/R_o). This indicates that at hypersonic speeds, the non-dimensional heating rates can be explained using one curve-fit equation. More details regarding this will be provided in the next chapter.

The objective of this particular section is to demonstrate the simplicity of implementing the relations developed in this research project. MATLAB was utilized as a tool to demonstrate the implementation of these correlations. Similarly, any other programming language can be easily used to compute the surface heat transfer rates for an ogive configuration.

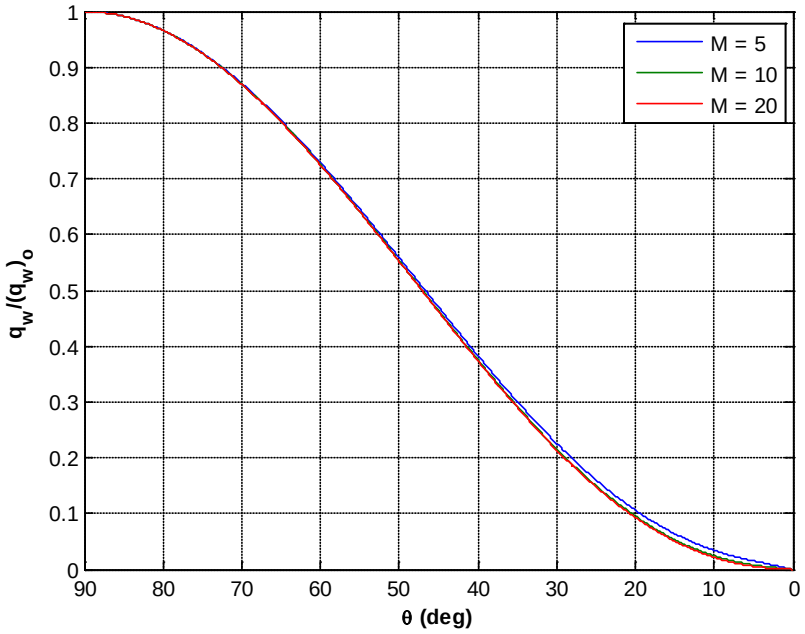

Figure 5.10 - Non-dimensional Heating Rates for a Paraboloid with R_o = 0.1 ft

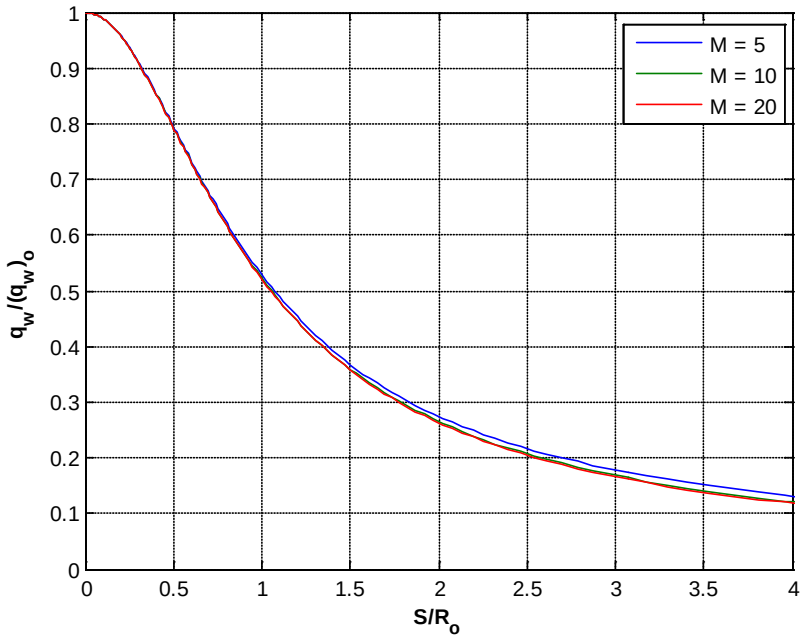

Figure 5.11 - Heating Rates as a Function of Non-dimensional Surface Location

Chapter 6

Validation and Results

This chapter discusses and compares the results generated to approximate engineering codes. Details regarding the usage of the engineering codes BLUNT2D and SABLE will also be provided. Additionally, the user requirements described in Section 4.1 will be reviewed again to assess the validity of the results and achievement of the objective of the research project.

6.1 Validation

The first part of this chapter will cover the usage of the engineering codes BLUNT2D and SABLE. These codes will assist in validating the correlations developed for computing the surface heating rates of a paraboloid.

6.1.1 Usage of BLUNT2D and SABLE

As described in Section 3.4.2, the approximate engineering code BLUNT2D is an inviscid flow solver. The code follows a structured grid scheme and computes boundary layer edge conditions. These edge conditions are then used as inputs to an approximate boundary layer code SABLE. In order to replicate the geometrical configuration of a paraboloid and the freestream conditions implemented in the development of the relations, it was necessary to

select specific input parameters for BLUNT2D and SABLE. Table 6.1 notes the input parameters and particular values implemented.

Table 6.1 - Inputs for BLUNT2D

Input Parameter	Definition	Options	Value(s) Implemented
igas	Gas model	0 - perfect gas 1 - CF_4 2 - equilibrium air 3 - equilibrium Martian atmosphere	0 - perfect gas
im	Number of points around body	-	101
jm	Number of points between the body and the shock	-	21
km	Maximum number of time steps	-	20,000
kout	Output interval	-	20,000
itsf	Type of time step	0 - global minimum time step 1 - local maximum time step	1 - local maximum time step
iinit	Initial shock/solution	0 - initial shock input numerically 1 - initial shock input analytically 2 - initial shock constant, dr(i) = dr1 3 - initial solution obtained from restart file	3 - initial solution obtained from restart file
iplot	Plot file output	0 - no 1 - yes	1 - plot file output
iidds	Initial data surface for super	0 - no 1 - yes	0 - no initial data for super
ixy	xy flowfield output file	0 - no 1 - yes	0 - no xy flowfield output file
vinfe	Freestream velocity (ft/s)	-	10,000 - 26,000
gam	Ratio of specific heats	(only for perfect gas)	1.4

Table 6.1 Continued

rgase	Gas constant (ft^2/s^2-°R)	(only for perfect gas)	1716.0
rhoie	Freestream density ($slugs/ft^3$)	-	6.457e-8 - 3.4558e-6
tinfe	Freestream temperature (°R)	-	370.9 - 479.1
pbmin	Minimum value for (p_b/p_{inf}) for initializing solution	(typical values are 20.0 - 50.0)	10.0
jay	Body type	0.0 - 2D bodies 1.0 - axisymmetric bodies	1.0 - axisymmetric bodies
dtfac	cfl step size	(0.5 - 0.8)	0.8
epsi	Smoothing coefficient	(epsi < 0.04)	0.02
bb	Body bluntness parameter	0.0 for paraboloid > 0.0 for ellipsoid < 0.0 for hyperboloid	0.0
bb1	Stretching parameter	(bb1 + bb2 = 1)	1.0
bb2	Stretching parameter	($bb1*x_i + bb2*x_i^2 = phi$)	0.0
dr1	Shock layer thickness at stagnation point	-	0.10
bs	Bluntness parameter for shock	-	0.0
rsorn	R_s/R_n at stagnation point	(generally > 1)	1.0
ibod	After body type	0 - blunt nose with no after body 1 - blunt nose with cone after body 2 - blunt nose with biconic after body	0 - blunt nose with no after body
bslop1	Not used	-	0
bslop2	Not used	-	0
phim	Phi max (deg)	-	90
xp	Location of pole	-	4.0
xc	Not used	-	0.0

The parameters marked in red were varied throughout the validation process. Many of the other variables remained constant, as advised by H. H. Hamilton. Note that various

parameters were selected to describe a blunt-nose paraboloid with no after body. Additionally, the maximum "phim" angle was chosen to be 90° so that the downstream output plane is perpendicular to the body axis. The parameter "xp" is a non-dimensional body length. BLUNT2D is an inviscid solution that is independent of body geometry variables and therefore, the solution from BLUNT2D for a specific set of freestream conditions is valid for all nose radii. This is the reason for non-dimensionalizing the body length by the nose radius. Refer to the figure below for an illustration of the non-dimensional body length.

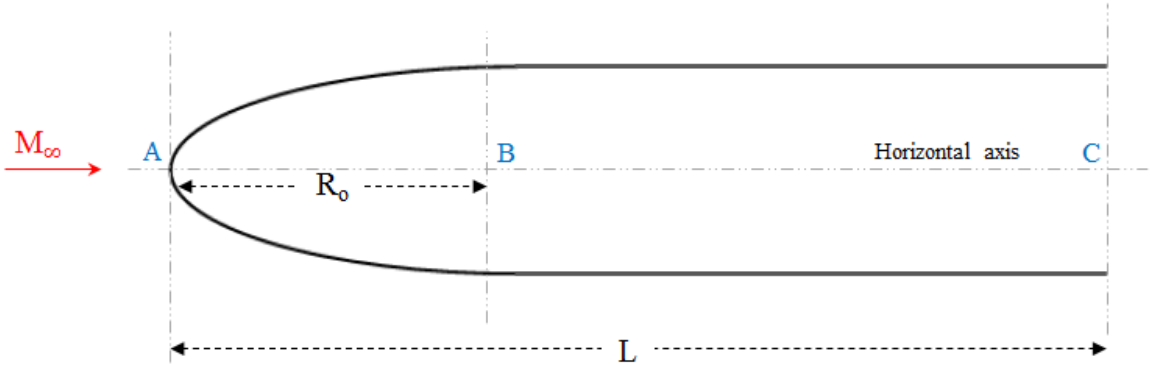

Figure 6.1- Geometrical Illustration of the Non-dimensional Body Length

Note that "L" is the distance along the axis measured from the nose (AC) and "R_o" is the nose radius of the parabola (AB). Therefore, the non-dimensional parameter "xp" can be described as,

$$xp = \frac{L}{R_o} \tag{6.1}$$

During the validation process, the non-dimensional body length parameter "xp" was held constant to a value of 4. It was advised by Hamilton to run test cases for paraboloid

geometries with an "xp" value of 3 or 4[27]. Additionally, some of the freestream conditions listed in the table above are from the user requirements section. Refer to Section 4.2.3 to see detailed information regarding the selection of the range of freestream velocities to be examined. It should be noted that freestream velocity is utilized in BLUNT2D, instead of Mach number. The ranges of density and temperature were chosen based on the range of altitude selected. The graph below describes the variation of the heat transfer rate as the altitude of the Space Shuttle changes[18]. From the figure, it can be noticed that the convective heating rate increases as the Shuttle travels through the atmosphere. The maximum heating rate occurs at approximately 230,000 feet before the heating rate starts to gradually decrease during the descent phase.

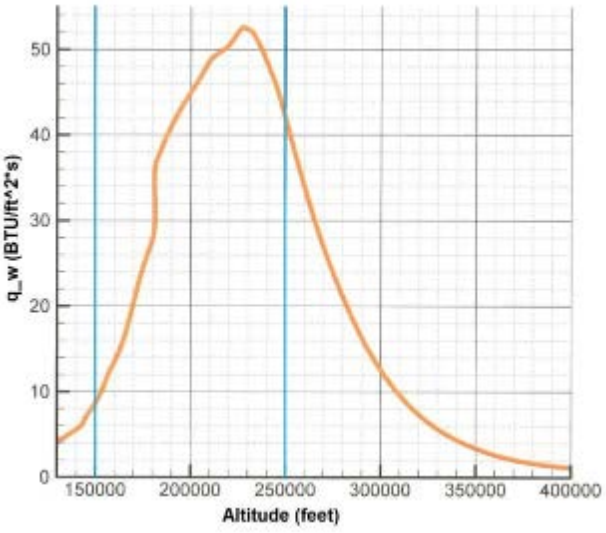

Figure 6.2 - Variation of Convective Heating Rate with Altitude for a Nominal Space Shuttle Trajectory

The range of velocities selected for examination is 10,000 - 26,000 ft/s (as detailed in Section 4.2.3). Figure 6.3 plots the velocity variation with altitude for a nominal Space Shuttle trajectory[18]. The Shuttle enters the Earth's atmosphere at a constant speed of 25,000 ft/s. As

the Shuttle becomes closer to the surface of the Earth, the speed of the vehicle starts to decrease. Marking the above velocities on the figure below would generate a rectangular box indicated by the orange line.

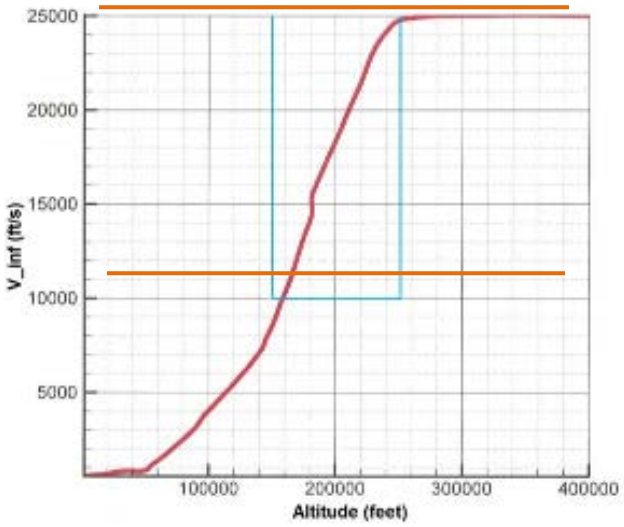

Figure 6.3 - Velocity Variation with Altitude for a Nominal Space Shuttle Trajectory

It is apparent in the figure that the altitudes experienced during the range of velocities noted earlier are between 150,000 - 250,000 feet (indicated by the blue lines). Thus, this is the range of altitudes selected for examination. The 1972 U.S. Standard Atmosphere was reviewed to evaluate the ranges of freestream density and temperature for the study. Based on the altitudes above, the freestream densities and temperatures were selected[26].

Once the input parameters are set for a particular case, a test run of BLUNT2D can be started. The test run will generate an output file named “blec.blu” that contains boundary layer edge conditions. The contents of this output file will then need to be copied into the input file for SABLE (blec.sab). Since SABLE is an approximate boundary layer code, it requires the boundary layer edge conditions from an inviscid solver. In addition to the “blec.sab” input file, SABLE also utilizes the following table of input parameters.

Table 6.2 - Inputs for SABLE

Input Parameter	Definition	Options	Value(s) Implemented
nm	Number of points in boundary layer	-	101
ksteps	No. of computational steps in streamwise (xi) direction	-	10,000
iprint	Print frequency in steamwise (xi) direction	-	3
itrans	Transition	0 - instantaneous transition 1 - finite transition	0 - instantaneous transition
igas	Gas model	0 - perfect gas 1 - CF_4 2 - equilibrium air 3 - equilibrium Martian atmosphere	0 - perfect gas
iflow	Flow type	0 - sharp 1 - blunt	1 - blunt
ireq	Radiative equilibrium wall	0 - no 1 - yes	0 - no radiative equilibrium wall
ient	Entropy	0 - constant entropy 1 - variable entropy	0 - constant entropy
jay	Body type	0 - 2D 1 - axisymmetric	1 - axisymmetric
iplot	Plot output file	0 - no plot 1 - plot (English units) 2 - plot (metric units)	1 - plot (English units)
etamax	Max eta value	(~10 for laminar, ~100 for turbulent)	10.0
ak	Stretching factor	(~1.04 for laminar, ~1.09 for turbulent)	1.04
aks	Turbulence constant k*	(~0.4)	0.4
as	Turbulence constant a*	(~26.0)	26.0
alam	Turbulence constant lambda	(~0.0168)	0.0168
vinf	Freestream velocity (ft/s)	-	10,000 - 26,000

Table 6.2 Continued

gamma	Ratio of specific heats	(only for perfect gas)	1.4
cp	Heat capacity at constant pressure	(only for perfect gas)	6006.0
rhoinf	Freestream density (slugs/ft^3)	-	6.4576e-8 - 3.4558e-6
tinf	Freestream temperature (°R)	-	370.9 - 479.1
pref	Reference pressure (slugs/ft^2)	(parameter "rhov2" obtained from output.blu)	(in English units)
uref	Reference velocity (ft/s)	(same as freestream velocity)	10,000 - 26,000
twc	Constant wall temperature (°R)	(file needed for twc = 0)	1000.0
rfac	Recovery factor	-	0.0
epsi	Surface emissivity	-	0.9
prc	Molecular Prandtl number	-	0.72
viscon	Sutherland constant	-	2.27e-08
suther	Sutherland constant	-	198.6
prt	Turb. Prandtl number	-	0.9
dx1	Initial step size (ft)	-	0.001
dxmax	Max step size (ft)	-	0.05
xtrans	Surface distance to transition (ft)	-	5000.0 (fully laminar)
xstop	Surface distance to stop solution (ft)	-	7.5
xbar	Constant for transition region	(approximately 2.0)	2.0
refln	Reference length (ft)	-	0.5, 1, 5, 8, 10
cst	Constant to convert input zt, xt, etc. (ft)	-	0.5, 1, 5, 8, 10
qref	Reference heating rate (BTU/ft^2-sec)	-	1.0

Similar to the inputs for BLUNT2D, the parameters that were varied in SABLE during the validation process are marked in red in Table 6.2. A few additional parameters altered in SABLE are reference pressure, reference velocity, and reference lengths. The reference

pressure value is obtained from “output.blu” once BLUNT2D has completed running. The reference velocity is required to be the same as the freestream velocity for a particular run.

Note that the actual nose radius of the paraboloid is also included within the input parameters. Viscous boundary layer solutions, such as SABLE, are dependent of geometry parameters. For the case of the ogive, the nose radius length is used to convert the physical dimension obtained from BLUNT2D as a non-dimensional quantity to feet. These parameters are listed as “refln” and “cst” in the table above. Both of these quantities will remain identical for a particular test case. Lastly, it is important to observe that the constant wall temperature was utilized during the validation process instead of the radiative equilibrium wall temperature. It was advised by Hamilton to use a constant wall temperature of 1000.0°R for all of the test cases[27].

Running SABLE generates an output file that contains information regarding the aerothermodynamic data for the particular geometry described within the inputs. Changes in pressure (P_e), velocity (V_e), temperature (T_e), Mach number (M_e), heat transfer rates at the wall (q_w), and heat transfer coefficients (C_H) across the surface of the body are included within the output file. For the validation process of this project only the heat transfer rates will be used to compare the data obtained using BLUNT2D/SABLE and the analytical method developed.

Section 6.2 will present the results obtained using both the analytical method developed and the approximate engineering codes. The next section will provide a more detailed description of the test cases completed with BLUNT2D and SABLE.

6.1.2 Test Cases for Validation

In order to incorporate the ranges of design parameters described in Sections 4.1 and 4.2, it was necessary to utilize and run the approximate engineering codes over a variety of test scenarios. The tables below specifically list the test scenarios that were implemented in BLUNT2D and SABLE to obtain results. The test scenarios were separated into multiple tables by nose radius lengths. Note that the parameters are provided in English units due to the limitations of BLUNT2D and SABLE. Both of these engineering codes are only valid when using English units. While some of the parameters are not necessary for the utilization of the engineering codes (such as Mach and altitude), they are provided to impart additional pertinent information to the user regarding each test case.

Table 6.3 - Test Cases for Nose Radius Length of 0.5 ft

Test Case No.	R_o (ft)	V_∞ (ft/s)	Mach	Altitude (ft)	ρ_∞ (slugs/ft^3)	T_∞ (°R)
1	0.5	10,000	9.3	150,000	3.4558E-06	479.1
2	0.5	14,000	13.0	150,000	3.4558E-06	479.1
3	0.5	16,000	14.9	150,000	3.4558E-06	479.1
4	0.5	19,000	17.7	150,000	3.4558E-06	479.1
5	0.5	22,000	20.5	150,000	3.4558E-06	479.1
6	0.5	26,000	24.2	150,000	3.4558E-06	479.1
7	0.5	10,000	9.8	200,000	5.3279E-07	439.9
8	0.5	14,000	13.7	200,000	5.3279E-07	439.9
9	0.5	19,000	18.5	200,000	5.3279E-07	439.9
10	0.5	22,000	21.5	200,000	5.3279E-07	439.9
11	0.5	16,000	17.0	250,000	6.4570E-08	370.9
12	0.5	18,000	19.1	250,000	6.4570E-08	370.9
13	0.5	22,000	23.4	250,000	6.4570E-08	370.9

Table 6.4 - Test Cases for Nose Radius Length of 1.0 ft

Test Case No.	R_o (ft)	V_∞ (ft/s)	Mach	Altitude (ft)	ρ_∞ (slugs/ft^3)	T_∞ (°R)
14	1.0	10,000	9.3	150,000	3.4558E-06	479.1
15	1.0	19,000	17.7	150,000	3.4558E-06	479.1
16	1.0	26,000	24.2	150,000	3.4558E-06	479.1
17	1.0	10,000	9.8	200,000	5.3279E-07	439.9
18	1.0	22,000	21.5	200,000	5.3279E-07	439.9
19	1.0	10,000	10.9	250,000	6.4570E-08	370.9
20	1.0	16,000	17.0	250,000	6.4570E-08	370.9
21	1.0	18,000	19.1	250,000	6.4570E-08	370.9
22	1.0	22,000	23.4	250,000	6.4570E-08	370.9

Table 6.5 - Test Cases for Nose Radius Length of 5.0 ft

Test Case No.	R_o (ft)	V_∞ (ft/s)	Mach	Altitude (ft)	ρ_∞ (slugs/ft^3)	T_∞ (°R)
23	5.0	10,000	9.3	150,000	3.4558E-06	479.1
24	5.0	19,000	17.7	150,000	3.4558E-06	479.1
25	5.0	26,000	24.2	150,000	3.4558E-06	479.1
26	5.0	10,000	9.8	200,000	5.3279E-07	439.9
27	5.0	16,000	15.6	200,000	5.3279E-07	439.9
28	5.0	22,000	21.5	200,000	5.3279E-07	439.9
29	5.0	10,000	10.6	250,000	6.4570E-08	370.9
30	5.0	16,000	17.0	250,000	6.4570E-08	370.9
31	5.0	18,000	19.1	250,000	6.4570E-08	370.9
32	5.0	22,000	23.4	250,000	6.4570E-08	370.9

Table 6.6 - Test Cases for Nose Radius Length of 10.0 ft

Test Case No.	R_o (ft)	V_∞ (ft/s)	Mach	Altitude (ft)	ρ_∞ (slugs/ft^3)	T_∞ (°R)
33	10.0	10,000	9.3	150,000	3.4558E-06	479.1
34	10.0	19,000	17.7	150,000	3.4558E-06	479.1
35	10.0	16,000	15.6	200,000	5.3279E-07	439.9
36	10.0	22,000	21.5	200,000	5.3279E-07	439.9
37	10.0	16,000	17.0	250,000	6.4570E-08	370.9
38	10.0	22,000	23.4	250,000	6.4570E-08	370.9

Note the freestream density and temperature values were obtained based on the altitude of the vehicle from the 1972 U.S. Standard Temperature[26]. The above tables will be revisited in Section 6.2.2 to yield the percent error analysis for each test case.

6.2 Results

The results generated from both the analytical method and the engineering codes (BLUNT2D and SABLE) will be presented in this section. The results from the analytical method will be referred to as "Desai" while the solutions from the engineering codes will be denoted as "SABLE".

It is important to note that the surface heating rate will be described in a non-dimensional form, to remain consistent to the developments made by Lees (see Section 3.3.2). The laminar boundary layer heat transfer rate along the surface of the paraboloid (q_w) will be non-dimensionalized by the stagnation point heat transfer rate ($q_{w,o}$). This method of non-dimensional analysis will allow comparison of results without the incorporation of parameter units. Similarly, the distance along the surface of the paraboloid will be non-dimensionalized by the nose radius. Thus, the surface location will be denoted by the non-dimensional parameter (S/R_o).

6.2.1 Percent Error Analysis

To evaluate the accuracy of the results generated by the analytical method, a percent error analysis was conducted between the analytical method and the engineering codes. The heating rates computed using BLUNT2D and SABLE were treated as exact results. The results generated from the correlations developed in this research were treated as approximate results. As described in Table 4.1, one of the requirements set by the user is that the analytical method must produce results within 15% accuracy of the exact results. Thus, once both of the methods have completed generating solutions for a set of input parameters (listed in Table 6.3), the percent error can be evaluated.

However, due to the variation in the total number of data points for each test case, an interpolated solution needed to be computed first. For both the approximate and exact methods, a spline interpolation was utilized to evaluate the solution for a set number of data points. A spline interpolation was selected as the form of interpolation due to the small amounts of interpolation error associated with it (allowing the comparison of interpolated results that closely match the raw data). Now that both set of solutions have equal number of data points, the percent error analysis can be performed. The equation used to compute the percent error is shown below. It is important to note that the absolute value of the percent error will be considered. The minimum and maximum percent errors for each test case will be presented in the following section.

$$\%\ \text{error} = \left| \frac{\left(\text{Desai result}\right) - \left(\text{SABLE result}\right)}{\left(\text{SABLE result}\right)} \right| \cdot 100\% \qquad (6.2)$$

6.2.2 Comparison of Non-dimensionalized Heating Rates

As mentioned in Section 6.1.2, various test cases were implemented into the method developed as a part of this research and BLUNT2D/SABLE. The test cases were validated over a range of freestream velocities and altitudes. The results of the non-dimensional heating rates were compared against one another to determine the minimum and maximum percent error values. The tables below describe the input parameters, minimum and maximum percent error, and the associated figure number for each test case. Note that the tables are separated by the nose radius of the parabolic-shaped geometry.

Table 6.7 - Non-Dimensional Heating Rate Results, R_o of 0.5 ft

No.	Figure No.	V_∞ (ft/s)	Mach	Altitude (ft)	|% Error|	
					Min	Max
1	6.4	10,000	9.3	150,000	0.16	11.3
2		14,000	13.0	150,000	0.18	11.9
3		16,000	14.9	150,000	0.17	12.1
4	C.1	19,000	17.7	150,000	0.18	12.2
5		22,000	20.5	150,000	0.18	12.3
6		26,000	24.2	150,000	0.19	12.4
7	6.5	10,000	9.8	200,000	0.16	11.2
8		14,000	13.7	200,000	0.18	11.9
9	C.2	19,000	18.5	200,000	0.18	12.2
10		22,000	21.5	200,000	0.18	12.3
11	6.6	16,000	17.0	250,000	0.17	11.9
12		18,000	19.1	250,000	0.18	12.1
13		22,000	23.4	250,000	0.18	12.3

Table 6.8 - Non-Dimensional Heating Rate Results, R_o of 1.0 ft

No.	Figure No.	V_∞ (ft/s)	Mach	Altitude (ft)	|% Error|	
					Min	Max
14	C.3	10,000	9.3	150,000	0.13	11.3
15		19,000	17.7	150,000	0.19	12.2
16		26,000	24.2	150,000	0.20	12.4
17	C.4	10,000	9.8	200,000	0.21	12.9
18		22,000	21.5	200,000	0.19	12.3
19	C.5	10,000	10.9	250,000	0.11	11.1
20		16,000	17.0	250,000	0.16	11.9
21	C.6	18,000	19.1	250,000	0.18	12.1
22		22,000	23.4	250,000	0.19	12.3

Table 6.9 - Non-Dimensional Heating Rate Results, R_o of 5.0 ft

No.	Figure No.	V_∞ (ft/s)	Mach	Altitude (ft)	|% Error|	
					Min	Max
23	C.7	10,000	9.3	150,000	0.18	11.4
24		19,000	17.7	150,000	0.25	12.2
25		26,000	24.2	150,000	0.25	12.4
26	6.7	10,000	9.8	200,000	0.18	11.3
27		16,000	15.6	200,000	0.24	12.0
28		22,000	21.5	200,000	0.25	12.3
29	C.8	10,000	10.6	250,000	0.17	11.1
30		16,000	17.0	250,000	0.23	12.0
31	C.9	18,000	19.1	250,000	0.25	12.1
32		22,000	23.4	250,000	0.24	12.3

Table 6.10 - Non-Dimensional Heating Rate Results, R_o of 10.0 ft

No.	Figure No.	V_∞ (ft/s)	Mach	Altitude (ft)	|% Error|	
					Min	Max
33	6.8	10,000	9.3	150,000	0.24	11.4
34		19,000	17.7	150,000	0.20	12.2
35	C.10	16,000	15.6	200,000	0.23	12.1
36		22,000	21.5	200,000	0.21	12.3
37	6.9	16,000	17.0	250,000	0.23	12.0
38		22,000	23.4	250,000	0.22	12.3

To illustrate some of the comparative results visually, a few of the test cases were selected to be displayed in this section. The figures presented in the remainder of this section are marked in red in Tables 6.7 to 6.10. The additional figures are shown in Appendix C.

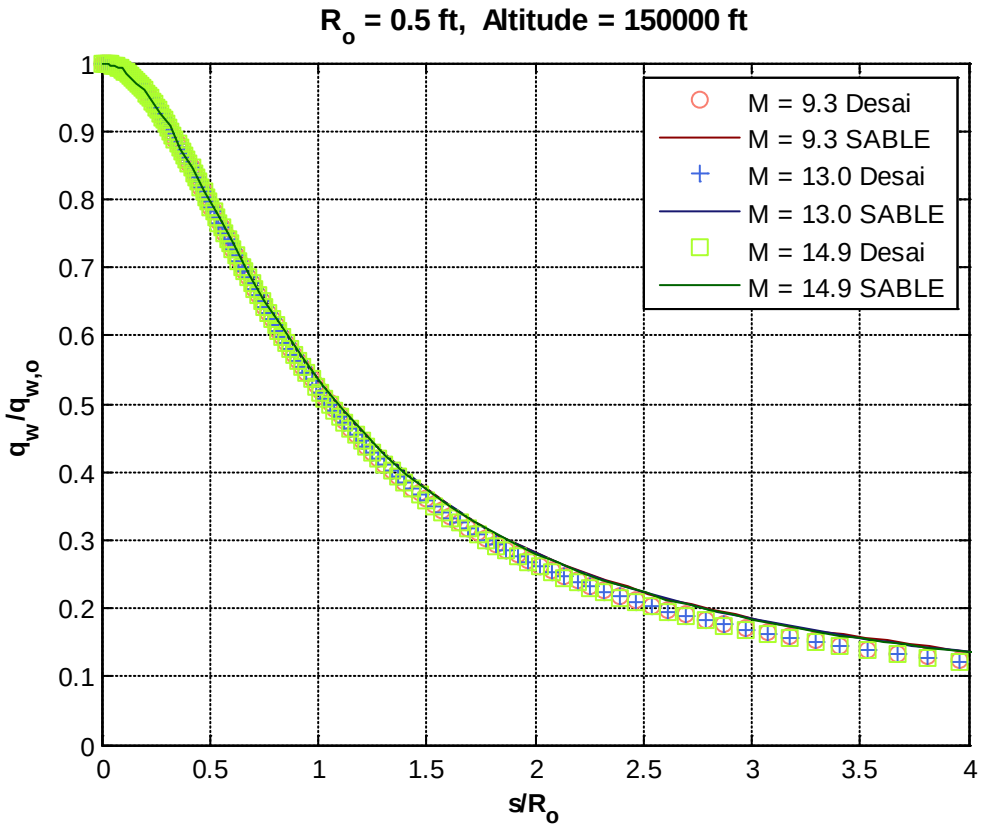

Figure 6.4 - Desai vs. SABLE Results for R_o = 0.5 ft, Alt = 150,000 ft, M = 9.3 to 14.9

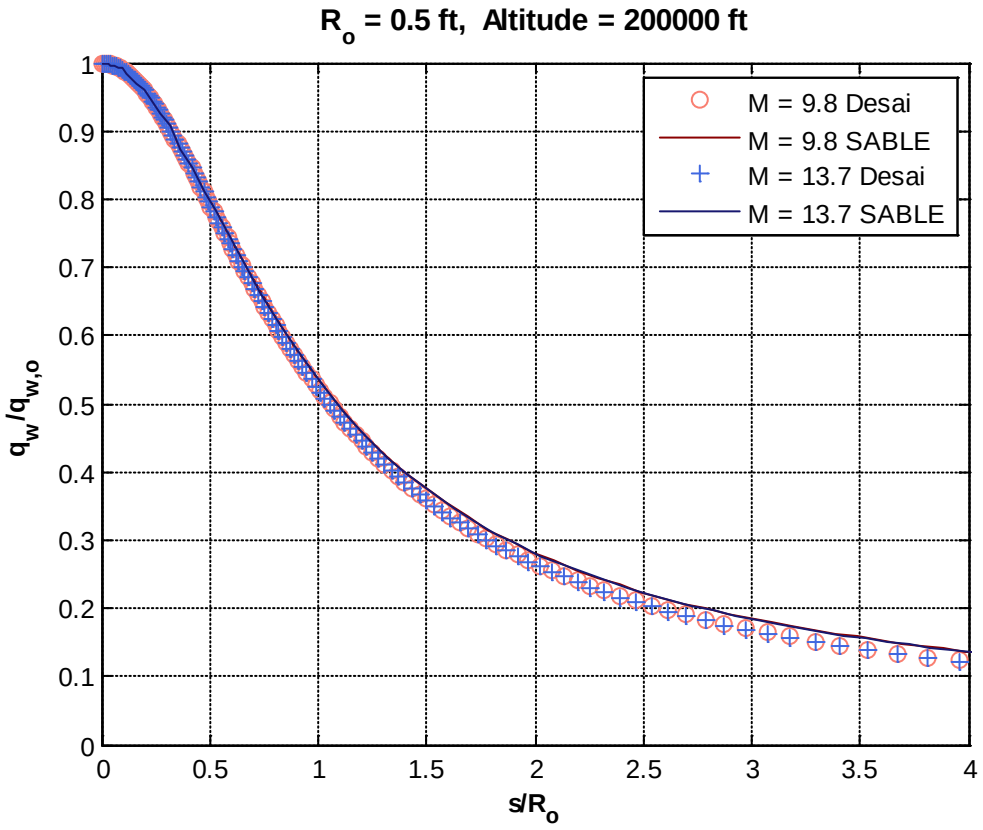

Figure 6.5 - Desai vs. SABLE Results for R_o = 0.5 ft, Alt = 200,000 ft, M = 9.8 to 13.7

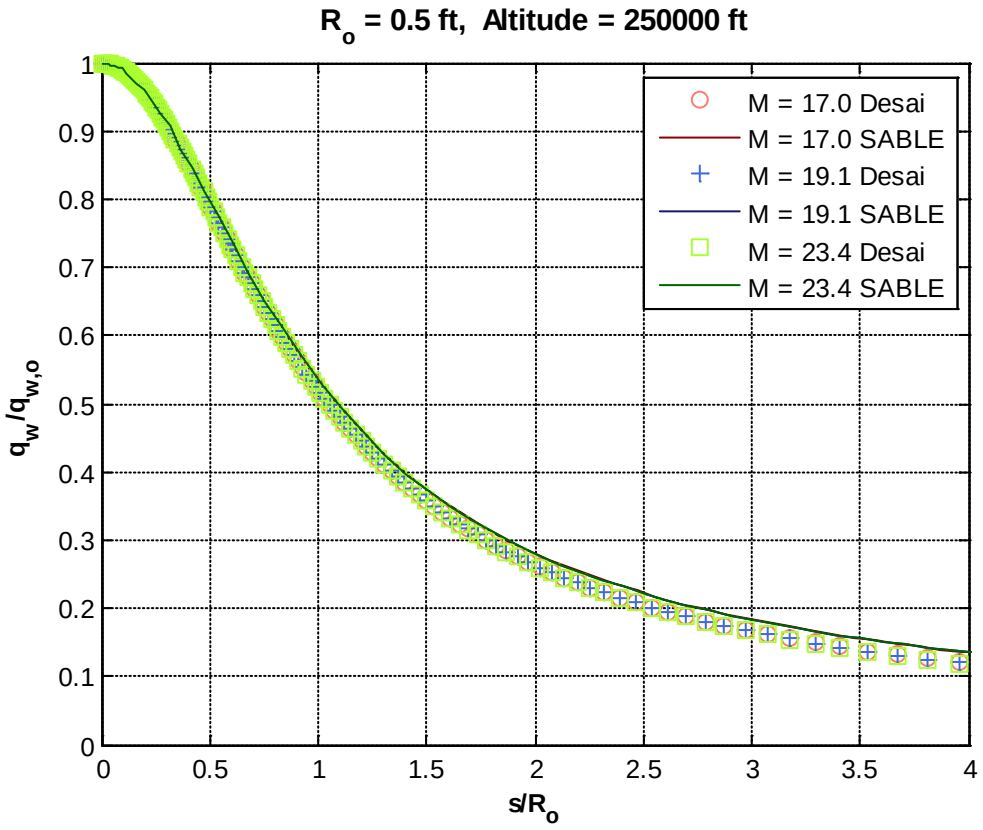

Figure 6.6 - Desai vs. SABLE Results for R_o = 0.5 ft, Alt = 250,000 ft, M = 17.0 to 23.4

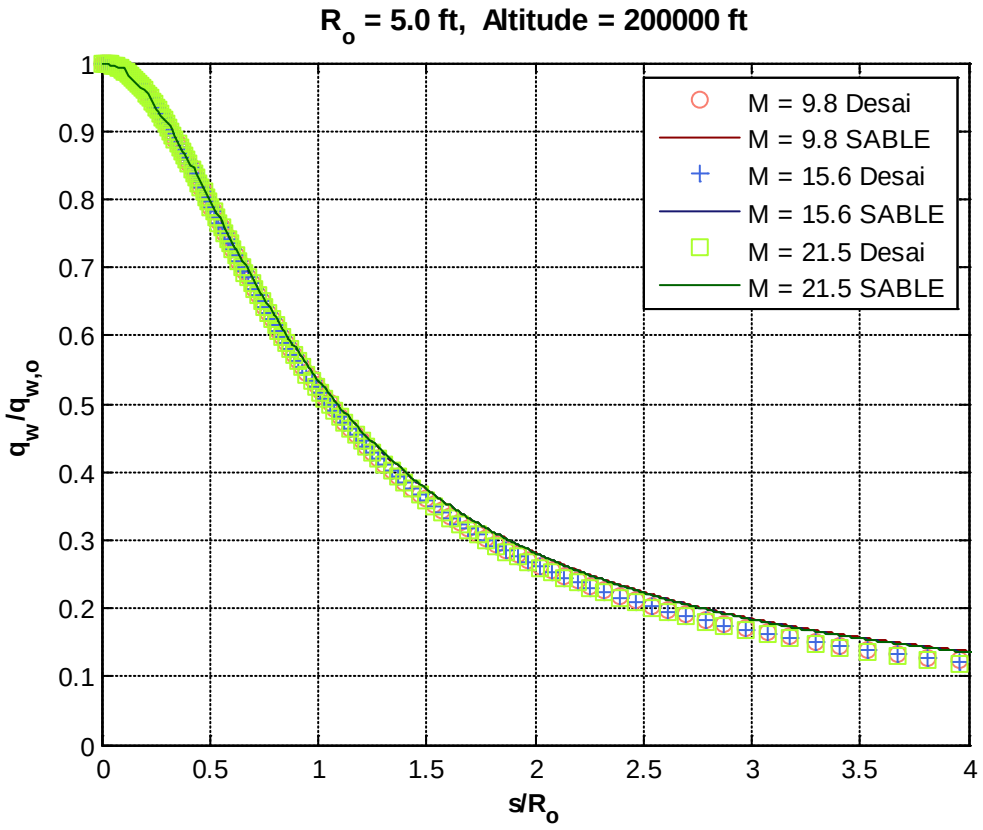

Figure 6.7 - Desai vs. SABLE Results for R_o = 5.0 ft, Alt = 200,000 ft, M = 9.8 to 21.5

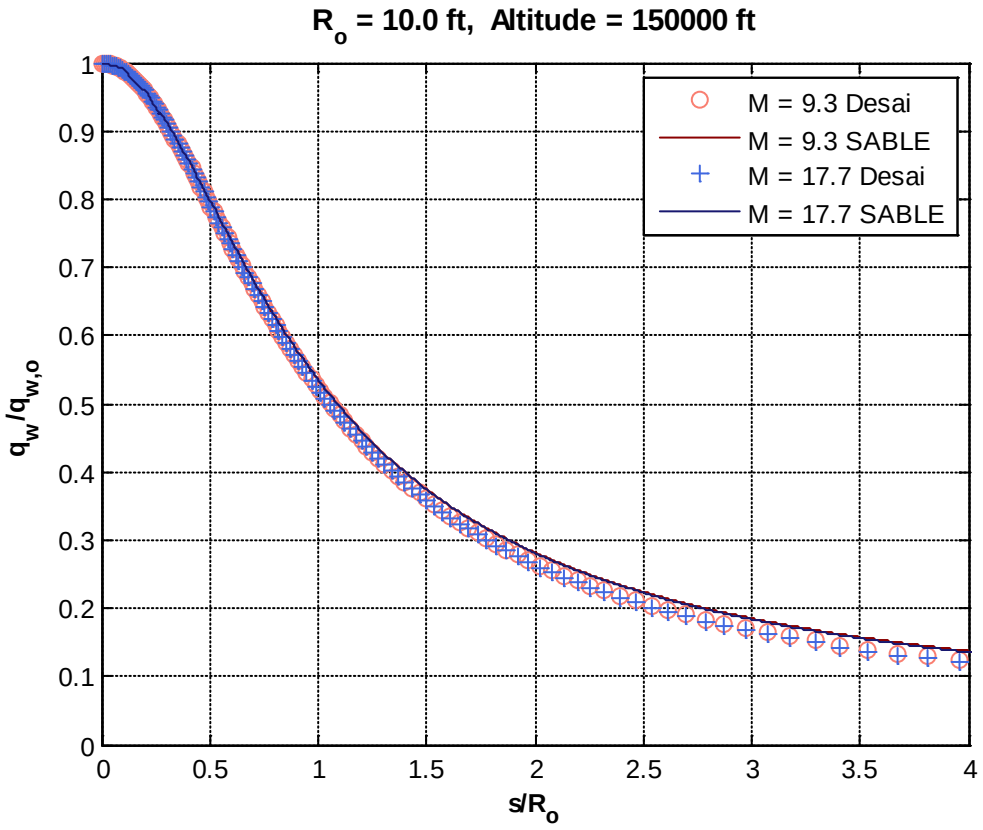

Figure 6.8 - Desai vs. SABLE Results for R_o = 10.0 ft, Alt = 150,000 ft, M = 9.3 to 17.7

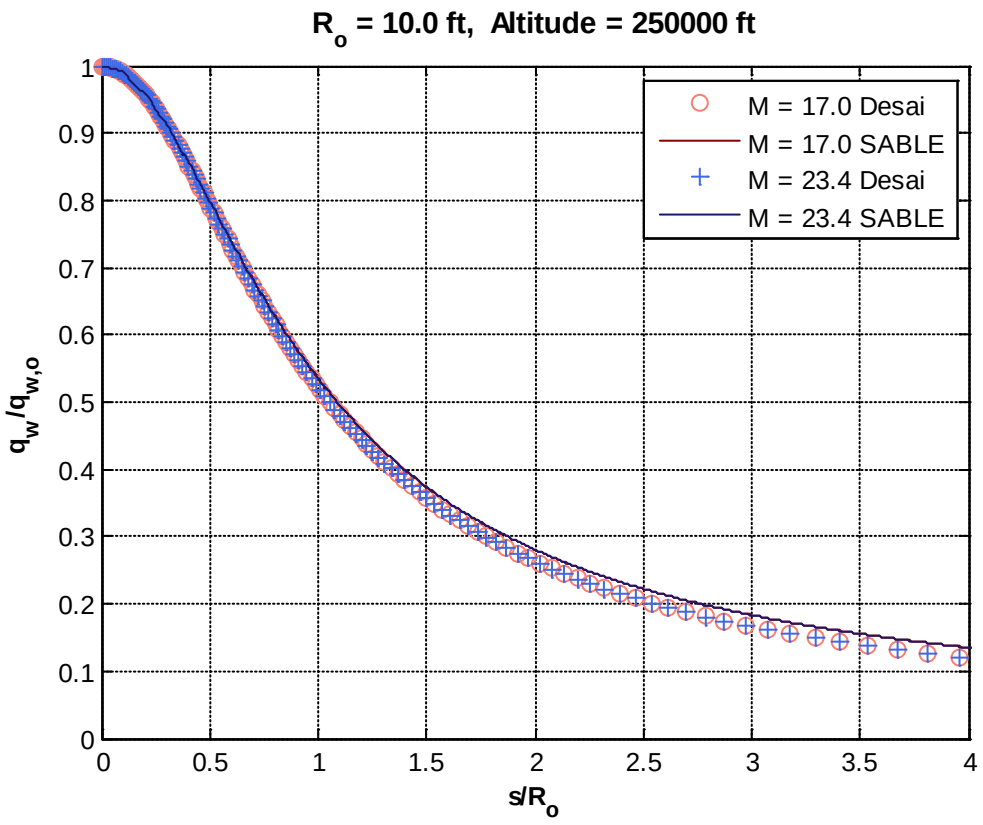

Figure 6.9 - Desai vs. SABLE Results for R_o = 10.0 ft, Alt = 250,000 ft, M = 17.0 to 23.4

6.2.3 Discussion of Non-dimensionalized Heating Rates

Many observations were made during the analysis phase of this research. Based on the percent error analysis and plots presented in the previous section, this section will identify and discuss the results. The following overall trends were noted from the results,

1. The results were more accurate near the forward stagnation point and decreased further away from the stagnation point.
2. The results were under-predicted at locations further away from the stagnation point.
3. Accuracy generally decreased at higher velocities.
4. The variation in altitude did not yield an overall trend in error.
5. Changes in nose radius did not influence the accuracy of the results.

A critical design requirement of a hypersonic vehicle is minimizing the amount of heat supplied to the body during re-entry. One of the ways this can be achieved is by selecting a configuration with high-pressure drag for the body, such as blunt bodies. Though much of the convective heat experienced by the vehicle can be reduced for the case of the parabolic-shaped geometries, the stagnation point region will still experience large amounts of thermal loads. This is due to maximum heating occurring at the stagnation point and remaining high near that location. Thus, it is important to accurately predict the surface heating rates near the stagnation point. According to the analysis completed in Section 6.2.2, it can be concluded that the results for the non-dimensional surface heating rates were the most accurate near the forward stagnation point. At surface locations closest to the stagnation point, an average of approximately 0.20 percent error was observed. At locations further away from the stagnation point, the accuracy of the results began decreasing. The table below indicates the average percent error of all of the runs at various locations along the surface.

Table 6.11 - Average Percent Error at Various Surface Locations

Non-dimensional Surface Location (s/R_o)	|Average % Error|
0.0	0.00
0.1	0.31
0.5	0.66
1.0	2.45
1.5	4.35
2.5	7.92
3.0	9.43
3.5	10.79
4.0	12.00

Note that near s/R_o values of less than 1.0, the average percent error remains below 1.0 percent. However beyond s/R_o values of 1.0, the average percent error increases significantly. For this reason, the non-dimensional surface locations are separated into 2 sections. The figure below indicates the region markings within the plot in addition to the non-dimensional surface heating rates (similar to Figure 6.4). Refer to Equation 6.3 for specific boundaries of the regions.

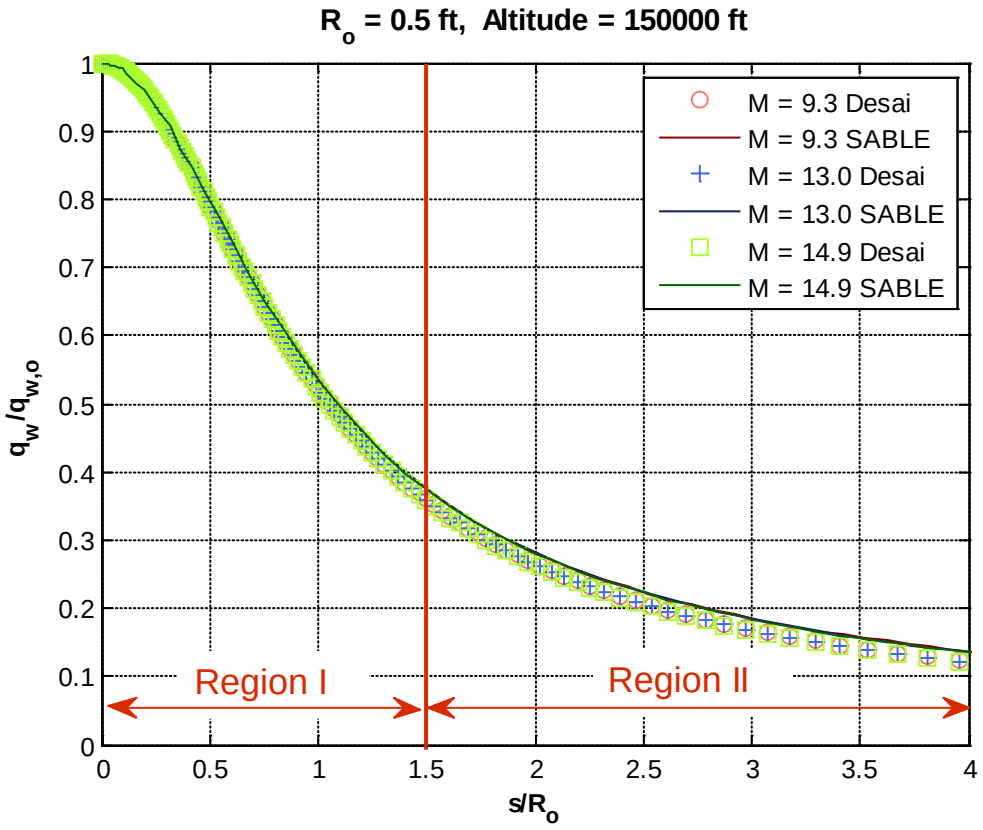

Figure 6.10 - Replication of Figure 6.4 with Region Markings

$$\text{Region I}: \quad 0 \le \frac{s}{R_o} \le 1.5$$
$$\text{Region II}: \quad 1.5 < \frac{s}{R_o} \le 4.0 \tag{6.3}$$

The two regions will be examined further in the following section. Since the area near the stagnation point (Region I) is defined to be the most significant region within the study, this conclusion is acceptable for the purpose of this research. It is important to note that this conclusion is valid for all ranges of altitudes, velocities, and nose radius lengths.

In Figure 6.10, it can be observed that at surface locations within Region II, the results generated by the method developed in this research under-predicted the non-dimensional heating rates. This indicates that the approximations computed by the analytical method generated lower results than expected. This characteristic within the results is consistently noticed for all of the test cases considered. In Table 6.11, the averages of the percent error along the surface of the paraboloid are listed as positive averages. However, this is only due to the percentage error formula (described in Equation 6.2) evaluating the absolute value of the error. If absolute value of the error was not taken into account, all of the results in Table 6.11 would be presented as negative errors. Within the field of aerothermodynamics, it is always regarded as beneficial to over-predict the surface heating rates. Under-predicting the thermal loads imparted on a body could yield many difficulties for the scientists, engineers, and designers involved. Although the results remain within the error limitation provided by the user, it important to consider this method and the associated results with some sort of a factor of safety or reliability. It will allow the method to be applicable within a set of limitations.

Furthermore, in order to determine the reasons for the above detailed characteristic existing within the results, the maximum error for each case was compared with the corresponding velocity for the particular run. All other variables were held constant to isolate and attribute any trend seen in the results to variations in velocity. By examining the relationship between maximum percentage error and velocity, another overall observation was recognized within the results. For an altitude of 150,000 ft and nose radius of 0.5 ft, the highest error (12.4%) occurred at a velocity of 26,000 ft/s, which is the highest velocity considered within the set of runs. The lowest error (11.3%) appeared at the lowest velocity tested, 10,000 ft/s. This comparison was completed for several other sets of parameters. Within all of the assessments, a similar observation was discovered. All of the test cases (per a set of parameters) were plotted to demonstrate and assist in determining a relationship between the change in velocity and maximum error observed in the results. Refer to Figure 6.11 to notice

the trend in the data points. The legend indicates the distinct set of parameters selected to conduct the analysis using various symbols and colors.

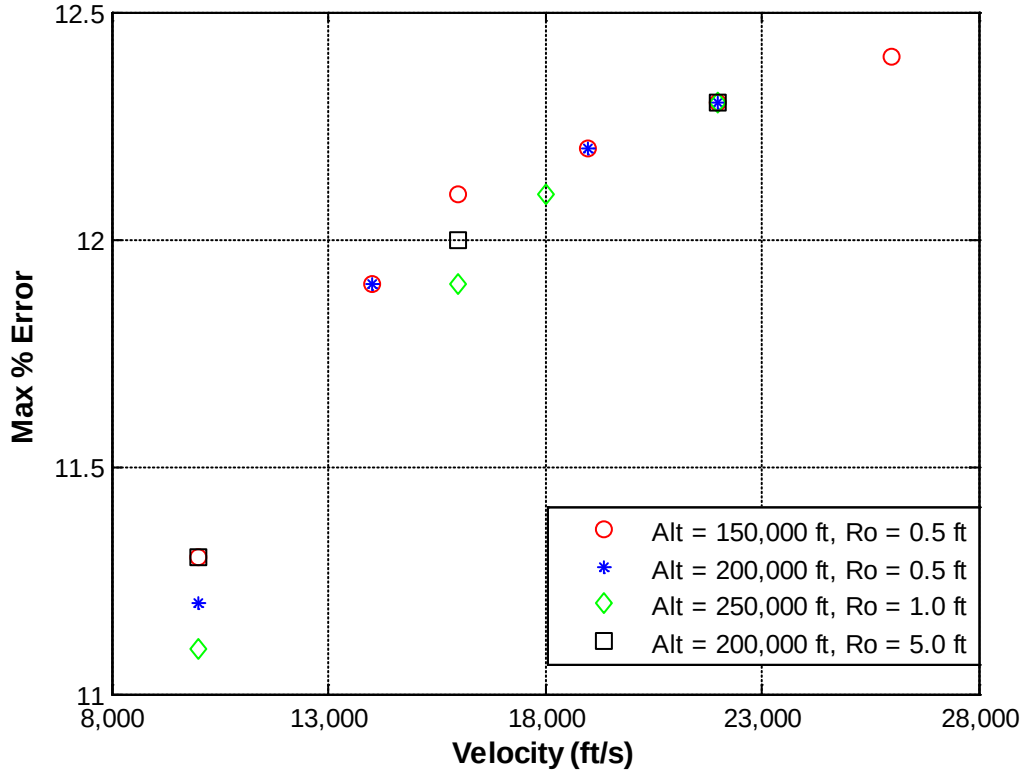

Figure 6.11 - Relationship between the Velocities Tested and Corresponding Maximum Errors

From this figure, it can be concluded that there exists a relationship between the velocity tested and error noted within the results. More specifically, the accuracy of the results decreased (in other words, the error in the results increased) at higher freestream velocities. It is important to note that the results for all test cases remained below the user requirement of 15% accuracy when compared with engineering codes. Thus, the method developed is deemed valid for the range of velocities considered for this research.

A similar examination was conducted to determine a relationship between altitudes implemented into the developed method and the maximum error generated. Based on the range of altitude set for validating the analytical method, three particular altitudes that sufficiently represented hypersonic flight were selected for testing. The three altitudes chosen were 150,000 ft, 200,000 ft, and 250,000 ft. A wide range of test cases were implemented using these three test altitudes. It was expected that a possible trend might exist between the altitude of the body and the accuracy of the results, when holding all other parameters constant. However, when the maximum errors were plotted against the corresponding altitude for each test scenario, a conclusive observation could not be made. The lowest altitude (150,000 ft) yielded a maximum error of 11.4% while the highest altitude (250,000 ft) produced a maximum error of 11.1% at a velocity of 10,000 ft/s and nose radius of 5.0 ft. For a separate set of parameters (velocity of 22,000 ft/s and nose radius of 0.5 ft), the variation in altitude did not alter the maximum error (remained 12.3% for all test cases). For several other sets of parameters, inconsistencies continued to exist within the analysis and a trend in the results could not be evaluated.

Due to the inconclusiveness of the results, it was determined that the variation in altitude does not yield an overall trend in the accuracy of the results. Note that all other parameters such as velocity and nose radius were maintained to be constant while conducting this analysis. This conclusion is valid for the range of altitude (150,000 ft to 250,000 ft) selected for this research. If the research extended the boundaries of the altitudes to be much larger, it is possible to notice a trend in the results. While this extension is out of the scope of this research, it can be incorporated in a future project.

Lastly, it was desired to evaluate whether a correlation can be formed for nose radius lengths and the maximum percentage error. Similar to the procedure described above, the variation in nose radius length was observed while keeping all other parameters constant. For a freestream velocity of 19,000 ft/s and an altitude of 150,000 ft, the maximum error did not

alter as the nose radius length was increased (the error remained as 12.2%). Similar behavior was noticed for most sets of parameters, including lower and higher velocities. With the exception of one outlier, the highest change in the error observed was 0.1% for a set of parameters. This variation in the error occurred twice in the results when the nose radius length was significantly enlarged (from 1 ft to 5 ft). The error does not escalate any further when the nose radius is increased from 5 ft to 10 ft. Refer to the figure below for a visual representation of the analysis.

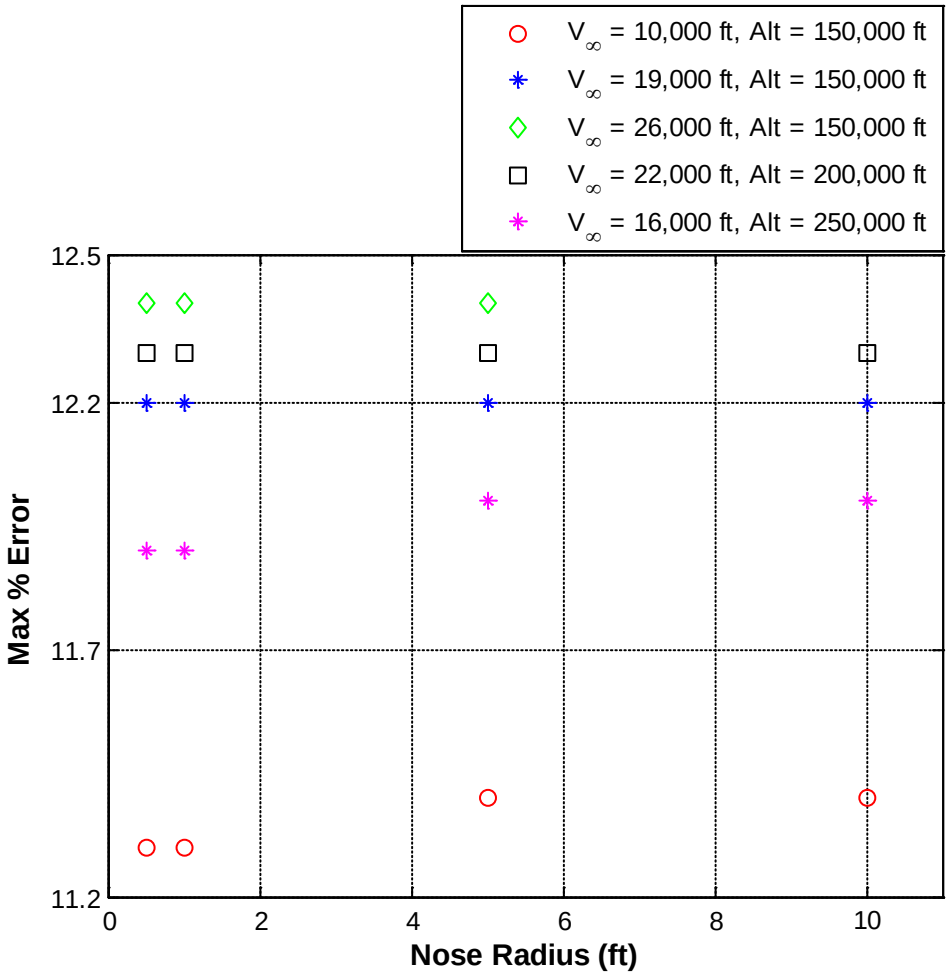

Figure 6.12 - Illustration of Nose Radii Effects on Maximum Error

This minute alteration in the maximum error can be attributed to the nose radius increasing by a multiple of 5, and can be disregarded since the nose radii considered for this research spans from 0.1 ft to 10 ft. Thus, it can be concluded from the analysis that the nose radius does not impact the error generated in the results. A greater change in error might be present in the results if the nose radius lengths are altered by larger orders of magnitude. While this may present an interesting topic for future projects, the conclusion was deemed valid for the purpose and requirements of this research.

6.2.4 Verification of User Requirements and Polynomial Curve Fits

Upon development of the method to evaluate non-dimensional surface heating rates, the project requirements listed in Table 4.1 were reexamined. The table below details each user requirement and discusses the completion of the requirement based on the validation of the correlations described in the preceding sections.

Table 6.12 - Verification of User Requirements

#	Description of Requirement	Completion of Requirement/Comments
1	The correlations evaluate laminar convective heating rate at any particular point along the body.	Yes - the laminar convective heating rates can be evaluated for a paraboloid with a specified nose radius.
2	The relations are valid for a perfect gas chemistry.	Yes - the results generated using the relations compare well with BLUNT2D/SABLE results for ideal gas chemistry.
3	The relations are valid for a range of freestream velocities.	Yes - valid for: $10{,}000 \text{ ft/s} \leq V_\infty \leq 26{,}000 \text{ ft/s}$
4	The relations are valid for a range of altitudes.	Yes - valid for: $150{,}000 \text{ ft} \leq \text{alt} \leq 250{,}000 \text{ ft}$
5	The relations are valid for a variety of nose radius lengths.	Yes - valid for: $0.5 \text{ ft} \leq R_o \leq 10 \text{ ft}$
6	The results generated must be within 15% accuracy of the results obtained from a proven engineering code.	Yes - maximum of 12.9% error observed when compared to BLUNT2D/SABLE
7	The correlations must be easily implemented on commonly used software.	Yes - the correlations for evaluating the heating rate were implemented in MATLAB.
8	The computer run time of the correlations must be less than 30 seconds.	Yes - all runs were completed in less than 2 seconds.

From the table above, it can be seen that all of the requirements were completed. The correlations are valid over a range of freestream velocities, altitudes, and nose radius lengths, as listed in the table. However as noted in the previous section, the non-dimensional surface location can be separated into two sections due to the increase of error noted between the regions. The average percent error within all of the test cases was analyzed for s/R_o values of 0 to 4.0. The first section is defined as s/R_o values of 0 (the stagnation point) to 1.5, where the highest surface heating occurs. The second region is indicated by s/R_o values of greater than 1.5 up to 4.0. The accuracy in the results is not as critical within this region, as the heating rates decrease further away from the stagnation point. Refer to Table 6.11 and Figure 6.10 for further explanation regarding the two regions.

After deducing various conclusions regarding this research in the previous section, it was desired to determine a polynomial curve fit that can describe the general form of the non-dimensional heating rates as an extension of this project. Since the results for the non-dimensional heating rates were independent of nose radius length (for the range of nose radii listed in the table above), the polynomial curve fits will be determined as a function of the non-dimensional surface location. The non-dimensional surface location parameter will be divided into two sections, as described above. Thus, two polynomial curve fits will be required to compute the surface heating rates. Note that altitude will be neglected within the curve fits since the variation in altitude did not yield an overall trend in the results.

To evaluate the curve fit that best defines the general shape of the non-dimensional heating rates for each region, it became necessary to test several curve fit models. Third, fourth, and fifth order polynomial curve fits were selected to model the surface heating rates as a function of the non-dimensional surface location parameter. The form of the 3^{rd}, 4^{th}, and 5^{th} order polynomial curve fits can be seen in Equations 6.4, 6.5, and 6.6, accordingly. Note that alphabetic variables A to F are the coefficients of the polynomials.

$$\frac{\dot{q}_w}{\dot{q}_{w,0}} = A \cdot \left(\frac{s}{R_o}\right)^3 + B \cdot \left(\frac{s}{R_o}\right)^2 + C \cdot \left(\frac{s}{R_o}\right) + D \tag{6.4}$$

$$\frac{\dot{q}_w}{\dot{q}_{w,0}} = A \cdot \left(\frac{s}{R_o}\right)^4 + B \cdot \left(\frac{s}{R_o}\right)^3 + C \cdot \left(\frac{s}{R_o}\right)^2 + D \cdot \left(\frac{s}{R_o}\right) + E \tag{6.5}$$

$$\frac{\dot{q}_w}{\dot{q}_{w,0}} = A \cdot \left(\frac{s}{R_o}\right)^5 + B \cdot \left(\frac{s}{R_o}\right)^4 + C \cdot \left(\frac{s}{R_o}\right)^3 + D \cdot \left(\frac{s}{R_o}\right)^2 + E \cdot \left(\frac{s}{R_o}\right) + F \tag{6.6}$$

Each test case was plotted and analyzed to find coefficients for the 3rd order polynomial curve fit for both sections. Once the coefficients for each test case were found, an average of the coefficients was evaluated. It is important to note that the coefficients from each test case did not deviate greater than 0.01 from the average of the coefficients, assuring the accuracy of the polynomial fit. Once this process was completed to find the 3rd order polynomial coefficients for both sections, the method was repeated to determine the 4th and 5th order polynomial coefficients for both regions. Table 6.13 lists the coefficients of 3rd, 4th, and 5th order polynomial curve fits for Region I and Region II. These coefficients can be substituted into Equations 6.4 - 6.6 to evaluate the non-dimensional heating rates at any point along the surface of the paraboloid.

Table 6.13 - Coefficients of Polynomial Curve Fits

Sec.	Order of Polynomial	Coefficients of Polynomial					
		A	B	C	D	E	F
I	3rd (Eq. 6.4)	2.39E-01	-4.69E-01	-2.64E-01	1.01E+00	-	-
II		-1.13E-02	1.27E-01	-5.19E-01	8.85E-01	-	-
I	4th (Eq. 6.5)	-2.87E-01	1.10E+00	-1.28E+00	-1.14E-02	1.00E+00	-
II		3.70E-03	-5.26E-02	2.96E-01	-8.16E-01	1.07E+00	-
I	5th (Eq. 6.5)	1.24E-01	-7.53E-01	1.71E+00	-1.61E+00	5.15E-02	1.00E+00
II		-1.10E-03	1.91E-02	-1.37E-01	5.21E-01	-1.11E+00	1.22E+00

Next, the accuracy of these polynomial curve fits needed to be evaluated to select one curve fit that best represents the non-dimensional heating rates. The 3rd, 4th, and 5th order polynomial curve fits were compared against the method developed in this research (named Desai) and SABLE. In an effort to avoid presenting copious amounts of data, the maximum error for each test case was evaluated for all three polynomial curve fits. Both regions of the non-dimensional surface location were considered when determining the maximum error. The average of the maximum errors noted in results was calculated for each order of polynomial to demonstrate the overall accuracy of the curve fits. The averages are listed in Table 6.14.

Table 6.14 - Average of the Maximum Errors Noted for Curve Fits

Order of Polynomial	|Average of Max % Errors|	
	Curve Fit Results Compared with Desai Results	Curve Fit Results Compared with SABLE Results
3rd	3.23	12.84
4th	1.01	11.85
5th	0.86	12.01

From the data presented in the table above, it can be seen that the 4th and 5th order polynomial fits better represent the method developed in this method (nearly less than 1% error in the results). A general trend of increasing accuracy with higher order of polynomial can be noticed from the results. Additionally when the curve fits were compared with SABLE, the 4th and 5th order polynomial curve fits generated smaller averages of maximum errors noted in all of the test cases. The coefficient of determination (R^2) was found to be 1 for the 4th order and higher polynomial fits. From this information, it was desired to select a polynomial curve fit that could sufficiently predict the surface heating rates while minimizing complexity. Thus, it was concluded that a 4th order polynomial would be chosen as the curve

fit to represent the non-dimensional surface heating rate results generated by the correlations developed in this research.

The 4^{th} order polynomial curve fit was implemented to generate non-dimensional heating rate results for each test case and compared with SABLE results for the same set of parameters. The maximum error was determined for each individual test scenario. The difference in maximum error between the correlations and the 4^{th} order polynomial curve fit was also computed. Refer to Appendix D for the maximum error analysis for the analytical method and the polynomial curve fit. From this analysis, it was found that the highest error noted in all of the test cases (using the curve fit) was 14.2%. This is only 1.67% higher than the maximum error calculated using the correlations developed in this research. Since the results generated using the polynomial fit produced a maximum error lower than 15% (as set in the user requirements), the 4^{th} order fit was deemed as an acceptable fit to predict the heating rates over the surface of a parabolic geometrical configuration.

Chapter 7

Conclusions and Recommendations

As a part of this research, mathematical relations to predict the convective heating rate over a paraboloid have been derived. The results obtained from these correlations have been validated using approximate engineering codes BLUNT2D and SABLE. The method developed has been confirmed successful and effective over a range of freestream velocities, altitudes, and nose radius lengths for an ideal gas chemistry. This chapter will discuss conclusions made as a result of this research as well as recommendations for future projects within a related field of study.

7.1 Conclusions

A method to evaluate non-dimensionalized laminar convective heating rates for a paraboloid has been developed. The surface heating along the surface of a parabolic-shaped geometry can be computed using the following correlation,

$$\frac{\dot{q}_w}{\dot{q}_{w,0}} = \frac{F(\theta)}{\sqrt{-\left[\frac{1}{\gamma M_\infty{}^2}\right]\left[1+\frac{(\gamma-1)}{2}M_\infty{}^2\right]\left[\frac{-8}{a^2}\cdot\left(1-\frac{1}{\gamma M_\infty{}^2}\right)\right]}} \tag{7.1}$$

where F(θ) can be evaluated using the following expressions,

$$F(\theta) = \frac{\left(\frac{1}{\sqrt{2}}\right)\left(\frac{p}{p_{0,2}}\right)\left(\frac{u_e}{u_\infty}\right)}{\left[\int_{90}^{\theta} -\left(\frac{p}{p_{0,2}}\right)\left(\frac{u_e}{u_\infty}\right)\frac{a}{2\sin^3\theta}\,d\theta\right]^{1/2}} \tag{7.2}$$

$$\frac{p}{p_{0,2}} = \sin^2\theta + \frac{1}{\gamma M_\infty{}^2}\cos^2\theta \tag{7.3}$$

$$\frac{u_e}{u_\infty} = \sqrt{\left[1 + \frac{1}{M_\infty{}^2}\cdot\left(\frac{2}{\gamma - 1}\right)\right]\left[1 - \left(\frac{p}{p_{0,2}}\right)^{\frac{(\gamma-1)}{\gamma}}\right]} \tag{7.4}$$

Refer to Section 5.2.3 for more details regarding the development of these correlations. Many test cases were compared against approximate engineering codes BLUNT2D and SABLE by varying altitude, freestream velocity, and nose radius length to validate the newly developed method. Based on the observations noted during the validation process, two 4th order polynomial curve fits were derived as a function of the non-dimensional surface location. The form of the polynomial curve fits and the values of the coefficients are provided below.

$$\frac{\dot{q}_w}{\dot{q}_{w,0}} = A\cdot\left(\frac{s}{R_o}\right)^4 + B\cdot\left(\frac{s}{R_o}\right)^3 + C\cdot\left(\frac{s}{R_o}\right)^2 + D\cdot\left(\frac{s}{R_o}\right) + E \tag{7.5}$$

Table 7.1 - Coefficients of 4th Order Polynomial Curve Fit

Sec.	$\frac{s}{R_o}$ Range	Coefficients of Polynomial				
		A	B	C	D	E
I	$0 < \frac{s}{R_o} \leq 1.5$	-2.87E-01	1.10E+00	-1.28E+00	-1.14E-02	1.00E+00
II	$1.5 < \frac{s}{R_o} \leq 4.0$	3.70E-03	-5.26E-02	2.96E-01	-8.16E-01	1.07E+00

The analytical method developed in this research and the polynomial curve fit correlations are valid for the below set of conditions,

1. $0.5 \text{ ft} \leq R_o \leq 10 \text{ ft}$
2. $10{,}000 \text{ ft/s} \leq V_\infty \leq 26{,}000 \text{ ft/s}$
3. $150{,}000 \text{ ft} \leq \text{alt} \leq 250{,}000 \text{ ft}$
4. Perfect gas chemistry

The method generated surface heating rate results within 15% accuracy to BLUNT2D and SABLE, while eliminating extended computational time and cost. The method can be utilized during early stages of design when considering a parabolic geometrical configuration for a hypersonic vehicle.

7.2 Recommendations

Several recommendations are discussed in this section for future projects in similar research areas. These suggestions were gathered after the completion of this project and reflect the lessons learned during the research process. A summary of the recommendations is presented first and a discussion of each suggestion listed is subsequently provided.

1. Automate the validation process for BLUNT2D and SABLE.
2. Validate heating rate results with a higher fidelity computational model.
3. Compare the derived relations with experimental results.
4. Develop relations considering equilibrium air chemistry.
5. Consider other parameters within the study.
6. Develop similar correlations for other geometries.

One of the challenges discovered during the validation process is the manual procedure required with running BLUNT2D and SABLE. Both approximate engineering codes involved altering inputs by hand for each test case. Additionally, it was necessary to obtain and transfer several outputs from BLUNT2D into SABLE before conducting a run in SABLE. Although both of these engineering codes did not involve heavy run times (the codes generated results with a few seconds), a considerable amount of time was expended to alter inputs and relocate outputs from one file to another during validation.

To eliminate time required to change inputs and outputs, a scripted code could be written to automate the process. Automating the validation process would significantly expedite the generation of results and require minimal efforts by the user to run a large number of test cases. Due to the time constraints for the project, the researcher did not generate a test automation script.

The results generated with the derived correlations were compared against approximate engineering codes. It would be advantageous to validate the results against another form of computational method. A higher fidelity computational model than BLUNT2D and SABLE could be implemented to generate results for a similar type of flow model and geometrical configuration. In the earlier sections (Section 3.4), other types of numerical methods are discussed. An aerothermodynamic simulation code named LAURA uses a similar approximation method to SABLE to compute higher fidelity heating rate results over the surface of a paraboloid. However, higher fidelity models are associated with greater costs and lengthy run times. In addition, the ability to acquire higher fidelity codes at an academia level can be challenging. For this reason and the availability of the approximate codes, BLUNT2D and SABLE were utilized as the codes to validate results.

Another form of validation within the engineering research field is experimental methods. It was desired to compare the derived relations to an experimental method in this research. An investigation of currently existing experimental methods to evaluate heating rates over a paraboloid did not yield any results. Experimental methods do, however, exist for computing heating rates for other types of geometries. For this reason and the usage of previously proven engineering codes for validation, it was deemed unnecessary to gather experimental results to compare with the developed analytical method. Though for a future research project, an experimental method could be developed and tested for evaluating heat transfer rates for a parabolic shaped geometrical configuration.

The analytical method derived is valid for an ideal gas chemistry. Lees developed a similar method for evaluating the surface heat transfer rates for spherical-nosed and blunted-nosed cone geometries. As discussed in the *Jet Propulsion* journal article, his approach is only conclusive for an ideal gas chemistry[3]. The objective of this research required establishing a method similar to Lees' to predict heating rates over the surface of a paraboloid. Thus, the method developed in this research focuses on ideal gas chemistry as the gas model. Due to

the assumptions associated with the perfect gas model, this gas model becomes invalid for extreme temperatures experienced during hypersonic flight. Equilibrium air chemistry allows simulating real gas effects at extremely high temperatures. A similar method could be developed incorporating equilibrium air chemistry and thus, yielding higher accuracy results for surface heat transfer rates.

The derived correlations in this research are valid for a range of specific parameters. These parameters include freestream velocity, altitude, and nose radius lengths. Many other variables were not considered within the study. Parameters such as angle of attack, wall temperature, turbulent heating, and effects of radiating heating could also be incorporated into the correlations. The addition of these parameters would produce results that more accurately represent the thermodynamic environment experienced by a hypersonic vehicle.

Lastly, other geometrical configurations could be investigated. As stated by Trench, one of the objectives desired by Dr. Fred DeJarnette is to establish a set of correlations that can accurately predict the thermodynamic properties of a hypersonic vehicle, regardless of the geometrical shape. Other geometries to be considered are sharp-nosed cone, bi-conic shaped geometry, and non-axisymmetric configuration. An axisymmetric geometrical configuration allows simplifying the correlations significantly. Thus, a non-axisymmetric geometry would require a great deal of further investigation. The analytical method developed in this research and other techniques detailed in previous chapters can be utilized to further the progress of such a development.

References

[1] Bertin, John J., *Hypersonic Aerodynamics.* AIAA Education Series, Washington, DC, 1994.

[2] Dobrowski, A. D., and J. Rowe. ""Command" Analysis of the Shuttle Orbiter Thermal Protection System Tiles." MSC 1981 World Users' Conference Proceedings (1981): N. pag. Web. 11 Oct. 2013. <http://web.mscsoftware.com/support/library/conf/wuc81/p01581.pdf>.

[3] Lester, Lees. "Laminar Heat Transfer over Blunt-Nose Bodies at Hypersonic Flight Speeds." *AIAA Journal Special Supplement: Centennial of Powered Flight (Jet Propulsion)* 26.4 (1956): 356-366. Print.

[4] Hamilton, H H., D R. Millman, and R B. Greendyke. "Finite-Difference Solution for Laminar and Turbulent Boundary Layer Flow over Axisymmetric Bodies with Ideal Gas CF4, or Equilibrium Air Chemistry." *NASA Technical Paper 3271*, 1992.

[5] "Returning From Space: Re-entry." FAA.gov. Web. 17 Oct. 2013. <http://www.faa.gov/other_visit/aviation_industry/designees_delegations/designee_types/ame/media/Section%20III.4.1.7%20Returning%20from%20Space.pdf>.

[6] Griffin, Michael D., and James R. French. *Space Vehicle Design*, 2nd Ed. American Institute of Aeronautics and Astronautics Inc., Reston, VA. 2004.

[7] Jeff, Scott. "Atmosphere & Spacecraft Re-entry." Aerospaceweb. N.p., 6 Mar. 2005. Web. 22 Oct. 2013. <http://www.aerospaceweb.org/question/spacecraft/q0218.shtml>.

[8] Anderson, John. *Hypersonic and High-Temperature Gas Dynamics*. Reston, VA: American Institute of Aeronautics and Astronautics, 2006.

[9] Anderson, John D., Jr. *Introduction to Flight*, 6th Ed. McGraw-Hill, New York, 2005.

[10] Bertin, John J., and Russell M. Cummings. "Critical Hypersonic Aerothermodynamic Phenomena*." *Annual Review of Fluid Mechanics* 36(2006): 129-157. Print.

[11] Ernst, Hirschel H. *Basics of Aerothermodynamics.* Reston, VA: American Institute of Aeronautics and Astronautics, Inc., 2005.

[12] Tauber, Michael E., Gene P. Menees, and Henry G. Adelman. "Aerothermodynamics of Transatmospheric Vehicles."*Journal of Aircraft* 24.9 (1987): 594-602. Print.

[13] Fay, J A., and F R. Riddell. "Theory of Stagnation Point Heat Transfer in Dissociated Air." *Journal of Aeronautical Sciences* 25.2 (1958): 73-85. Print.

[14] Detra, R W., N H. Kemp, and F R. Riddell. "Addendum to Heat Transfer to Satellite Vehicles Reentering the Atmosphere." *Jet Propulsion* 27.12 (1957): 1256-1257. Print.

[15] Scott, C.D., Ried, R. C., Maraia, R.J. Li, C.P. and Derry, S.M., "An AOTV Aeroheating and Thermal Protection Study," H. F. Nelson (ed.), *Thermal Design of Aeroassisted Orbital Transfer Vehicles*, Vol. 96 of Progress in Astronautics and Aeronautics, AIAA, New York, 1985, pp. 198-229.

[16] Cheatwood, F M., and Peter A. Gnoffo. "User's Manual for the Langley Aerothermodynamics Upwind Relaxation Algorithm (LAURA)." NASA Technical Memorandum 4674, April 1996.

[17] Hamilton, H H., and J R. Spall. "Time-Dependent Solution for Axisymmetric Flow over a Blunt Body with Ideal Gas, CF4, or Equilibrium Air Chemistry." *NASA Technical Paper 327*, July 1986.

[18] Trench, Brian Patrick. “Laminar Convective Heating Rate Correlations for Blunted Sphere Cones with Equilibrium Air Chemistry.” MS thesis North Carolina State University, 2012. *Theses and Dissertations.* Web. 23 Aug. 2013

[19] Hamilton, H. H., DeJarnette, F. R., and Weilmuenster, K. J., “Application of Axisymmetric Analog for Calculating Heating in Three-Dimensional Flows,” *Journal of Spacecraft and Rockets* 24.4 (1987): 296-302. Print.

[20] Hamilton, H. H., Greene, F. A., and DeJarnette, F. R., “Approximate Method for Calculating Heating Rates on Three-Dimensional Vehicles,” *Journal of Spacecraft and Rockets* 31.3 (1994): 345-354. Print.

[21] Hamilton, H. H, Weilmuenster, K. J., DeJarnette, F. R., “Improved Approximate Method for Computing Convective Heating on Hypersonic Vehicles Using Unstructured Grids” AIAA-2006-3394, June 2006.

[22] Cooke, J. C., “An Axially Symmetric Analogue for General Three-Dimensional Boundary Layers,” Reports and Memoranda No. 3200, British Aeronautical Research

Council, 1961.

[23] Palmer, Grant E. "Construction of CFD Solutions Using Interpolation Rather than Computation with the ADSI Code."*AIAA-2009-141*, January 2009.

[24] Whittington, Kurt Thomas. “A Tool to Extrapolate Thermal Reentry Atmosphere Parameters Along a Body in Trajectory Space.” MS thesis North Carolina State University, 2011. *Theses and Dissertations.* Web. 30 Oct. 2013

[25] Romanishin, William. "Wednesday August 31 2011." *DrBill's Astronomy Web Site*. N.p., n.d. Web. 1 Nov. 2013. <http://hildaandtrojanasteroids.net/A2513-orbits.html>.

[26] National Aeronautics and Space Administration, *U.S. Standard Atmosphere, 1972*, NASA-TM-X-74335, Washington, DC, October 1976.

[27] Hamilton, Harris. “Blunt and Sable files for your case.” Message to the author. 6 Dec. 2013. E-mail.

Appendices

Appendix A – Development of Geometric Relations

This appendix details the process of developing geometric relations for an ogive. These relations will be necessary when determining the correlations for the heat transfer rates over the surface of the ogive. Refer to Section 5.1.1 for a figure illustrating the ogive configuration and describing the coordinate system used for the derivations below.

To determine the expression for "dr" and "dx", the derivative of Equation 5.3 was evaluated as,

$$\frac{dr}{dx}\left(r=\sqrt{ax}\right)=\frac{1}{2}\left(ax\right)^{-1/2}\cdot a=\frac{a}{2r} \tag{A.1}$$

By definition of the Pythagorean Theorem, the equation for the change in "s" can be written as Equation A.2. The equation for "ds" can be simplified by multiplying the right side of the equation by (dr/dr).

$$ds=\sqrt{\left(dx\right)^2+\left(dr\right)^2} \tag{A.2}$$

$$\begin{aligned} ds=\sqrt{\left(dx\right)^2\left(\frac{dr}{dr}\right)^2+\left(dr\right)^2\left(\frac{dr}{dr}\right)^2}&=dr\sqrt{\left(\frac{dx}{dr}\right)^2+1}\\ &=dx\sqrt{\left(\frac{dr}{dx}\right)^2+1}\end{aligned} \tag{A.3}$$

The following geometrical relation was given to the researcher for the case of the ogive,

$$ds=Rd\theta \tag{A.4}$$

where R is the radius length of the parabola at a particular point along the surface of the ogive. In order to determine the correlation for "R", the expression for "dθ" must be

evaluated. This can be accomplished by substituting the correlation for “ds” from Equation A.3.

$$\frac{d\theta}{dx} = \frac{\sqrt{\left(\frac{dr}{dx}\right)^2 + 1}}{R} \tag{A.5}$$

To further simplify this relation, the expression for (dθ/dx) must be obtained. This can be done by taking the derivative of Equation 5.4 with respect to “x”. First, the left side of Equation 5.4 will be differentiated,

$$\begin{aligned} \frac{d}{dx}\left(\tan\theta\right) &= \frac{d\left(\tan\theta\right)}{d\theta} \cdot \frac{d\theta}{dx} = \sec^2\theta \cdot \frac{d\theta}{dx} \\ &= \frac{1}{\cos^2\theta} \cdot \frac{d\theta}{dx} \end{aligned} \tag{A.6}$$

The cosine term in the above equation can be represented in terms of “x” and “r” by examining Figure 5.6 again and rewriting the angle as a cosine function.

$$\cos\theta = \frac{dx}{ds} \tag{A.7}$$

Substituting the expression for “ds” from Equation A.3 will yield,

$$\cos\theta = \frac{dx}{dx\sqrt{\left(\frac{dr}{dx}\right)^2 + 1}} \tag{A.8}$$

Squaring Equation A.8 will allow determining the expression for the cosine term in Equation A.6.

$$\cos^2\theta = \frac{1}{\left(\frac{dr}{dx}\right)^2 + 1} \tag{A.9}$$

Equation A.6 can now be simplified as,

$$\frac{d}{dx}\left(\tan\theta\right) \;=\; \frac{1}{\cos^2\theta}\cdot\frac{d\theta}{dx} \;=\; \left[\left(\frac{dr}{dx}\right)^2 + 1\right]\cdot\left(\frac{d\theta}{dx}\right) \tag{A.10}$$

Lastly, differentiating the right hand side of Equation 5.4 with respect to "x" produces a second derivative of (dr/dx). The final expressions are written below,

$$\frac{d}{dx}\left(\tan\theta = \frac{dr}{dx}\right) \;\Rightarrow\; \left[\left(\frac{dr}{dx}\right)^2 + 1\right]\cdot\left(\frac{d\theta}{dx}\right) = \frac{d^2r}{dx^2} \tag{A.11}$$

$$\left(\frac{d\theta}{dx}\right) = \frac{\frac{d^2r}{dx^2}}{\left[\left(\frac{dr}{dx}\right)^2 + 1\right]} \tag{A.12}$$

Substituting Equation A.12 into Equation A.5 yields the following result for "R",

$$\frac{1}{R} = \frac{-\frac{d^2r}{dx^2}}{\left[1 + \left(\frac{dr}{dx}\right)^2\right]^{3/2}} \tag{A.13}$$

Replacing the derivative terms with the appropriate differentials of the function "r" for an ogive (Equations A.14 and A.15) yields Equation A.16.

$$\frac{dr}{dx} = \frac{a}{2r} \tag{A.14}$$

$$\frac{d^2r}{dx^2} = \frac{-a^2}{4(ax)^{3/2}} \tag{A.15}$$

$$\frac{1}{R} = \frac{\frac{a^2}{4}}{\left[r^2 + \frac{a^2}{4}\right]^{3/2}} \tag{A.16}$$

When r = 0, the radius length (R) will be equivalent to the nose radius length (R_o). Using this boundary condition, the relationship between "a" and the nose radius can be determined,

$$a = 2R_o \tag{A.17}$$

Additionally, the term (ds/dr) can be further simplified for the ogive geometry using Equation A.3 and the above relation.

$$\frac{ds}{dr} = \sqrt{\left(\frac{dx}{dr}\right)^2 + 1} = \sqrt{\frac{r^2}{R_o^2} + 1} \tag{A.18}$$

Appendix B – Evaluation of the 2nd Pressure Derivative

This appendix describes the process of evaluating the second pressure derivative. This appendix serves as an attachment to the process detailed in Section 5.2.2. Determining the second derivative of pressure is essential in deriving an expression for the velocity derivative for the case of the ogive.

To compute the pressure derivative term in the square root, the modified Newtonian law will be implemented. The modified Newtonian law allows representing the pressure ratio for blunt-nosed bodies as,

$$\frac{p}{p_\infty} = \left(\frac{p_{0,2}}{p_\infty} \cdot \sin^2 \theta \right) + \cos^2 \theta \tag{B.1}$$

where $P_{0,2}$ denotes the stagnation pressure behind the shock wave and theta represents the angle tangential to the surface of the geometry. Differentiating Equation B.1 twice provides the following expressions,

$$\frac{d\left(p/p_\infty \right)}{d\theta} = \frac{p_{0,2}}{p_\infty}\left(2\cos\theta\sin\theta \right) - 2\cos\theta\sin\theta \tag{B.2}$$

$$\frac{d^2\left(p/p_\infty \right)}{d\theta^2} = \frac{p_{0,2}}{p_\infty}\left(2\cos\left(2\theta \right) \right) - 2\cos\left(2\theta \right) \tag{B.3}$$

Since Equation 5.17 requires the second derivative of pressure with respect to “s”, Equation B.3 must be converted using the chain rule for higher derivatives. The chain rule states that,

$$\frac{d^2\left(p/p_\infty\right)}{ds^2}=\left(\frac{d^2\left(p/p_\infty\right)}{d\theta^2}\right)\left(\frac{d\theta}{ds}\right)^2+\left(\frac{d\left(p/p_\infty\right)}{d\theta}\right)\left(\frac{d^2\theta}{ds^2}\right) \tag{B.4}$$

Note that the chain rule for higher derivatives for completed using the non-dimensional quantity (p/p_∞). The above relation requires evaluating ($d\theta/ds$) for the ogive geometry. To compute this, several equations, regarding the geometry, developed in the previous section will be utilized. Combining Equations 5.4 and A.14 yields,

$$r=\frac{a}{2}\cot\theta \tag{B.5}$$

Substituting the above equation into Equation 5.7 gives,

$$ds=\sqrt{1+\frac{\left(\frac{a}{2}\cot\theta\right)^2}{R_o^{\,2}}}\cdot\frac{a}{2}\cdot d\left(\cot\theta\right) \tag{B.6}$$

$$(1) \qquad (2)$$

The next step is to simplify the above equation to achieve a simpler relationship between ds and $d\theta$. To accomplish this, the term in the bracket (labeled as (1)) will be evaluated first. By multiplying the first term within the root by the common denominator of ($4R_o^{\,2}\cdot\sin^2\theta$), Equation B.7 was derived. This equation was further simplified by using the boundary condition ($r = 0$ and $R = R_o \rightarrow a = 2R_o$) and the geometric relation ($\sin^2\theta + \cos^2\theta = 1$). This can be seen in Equation B.8.

$$(1)\rightarrow\sqrt{1+\frac{a^2\cos^2\theta}{4R_o^{\,2}\sin^2\theta}}=\sqrt{\frac{4R_o^{\,2}\sin^2\theta+a^2\cos^2\theta}{4R_o^{\,2}\sin^2\theta}} \tag{B.7}$$

$$(1) \rightarrow \sqrt{\frac{4R_o^{\,2}\sin^2\theta + \left(2R_o\right)^2\cos^2\theta}{4R_o^{\,2}\sin^2\theta}} = \sqrt{\frac{1}{\sin^2\theta}} = \frac{1}{\sin\theta} \tag{B.8}$$

The second term in B.6 (marked as (2)) was differentiated to achieve Equation B.9. Combining Equations B.8 and B.9 provides a simplified relationship for (ds/dθ).

$$(2) \rightarrow \frac{a}{2}\left[d\left(\cot\theta\right)\right] = \frac{a}{2}\left(-\frac{1}{\sin^2\theta}\right)d\theta \tag{B.9}$$

$$\frac{ds}{d\theta} = -\frac{a}{2\sin^3\theta} \tag{B.10}$$

Now the second derivative of pressure can be evaluated using the above relation. Substituting Equations B.2, B.3, and B.10 into the formula for (d^2p/ds^2) in Equation B.4 provides,

$$\frac{d^2\left(p/p_\infty\right)}{ds^2} = \left[\frac{p_{0,2}}{p_\infty}\cdot\left(2\cos\left(2\theta\right)\right) - 2\cos\left(2\theta\right)\right]\left[\frac{4\sin^6\theta}{a^2}\right] \tag{B.11}$$

It is necessary to evaluate the above expression at the forward stagnation point, so that it can be substituted into Equation 5.17. At the stagnation point, s = 0 and θ = π/2. Using these conditions, the following expression was evaluated.

$$\left(\frac{d^2\left(p/p_\infty\right)}{ds^2}\right)_0 = \frac{-8}{a^2}\cdot\left(\frac{p_{0,2}}{p_\infty} - 1\right) \tag{B.12}$$

Appendix C – Plotted Results of Non-dimensional Heating Rates

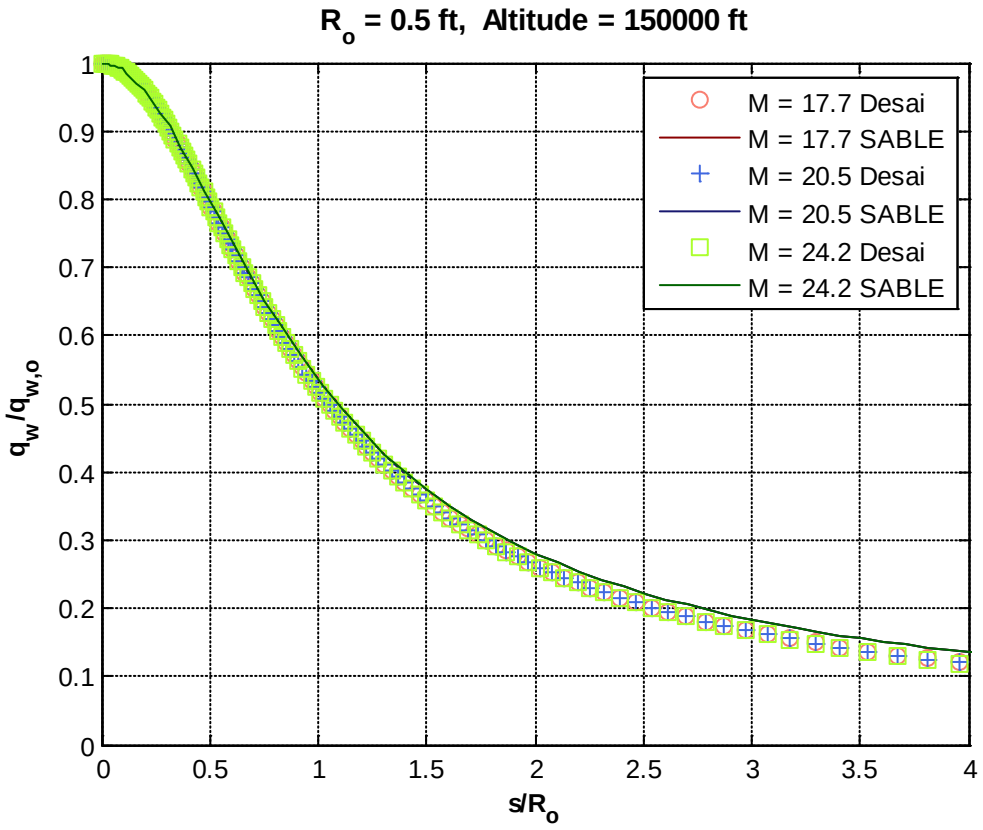

Figure C.1 - Desai vs. SABLE Results for R_o = 0.5 ft, Alt = 150,000 ft, M = 17.7 to 24.2

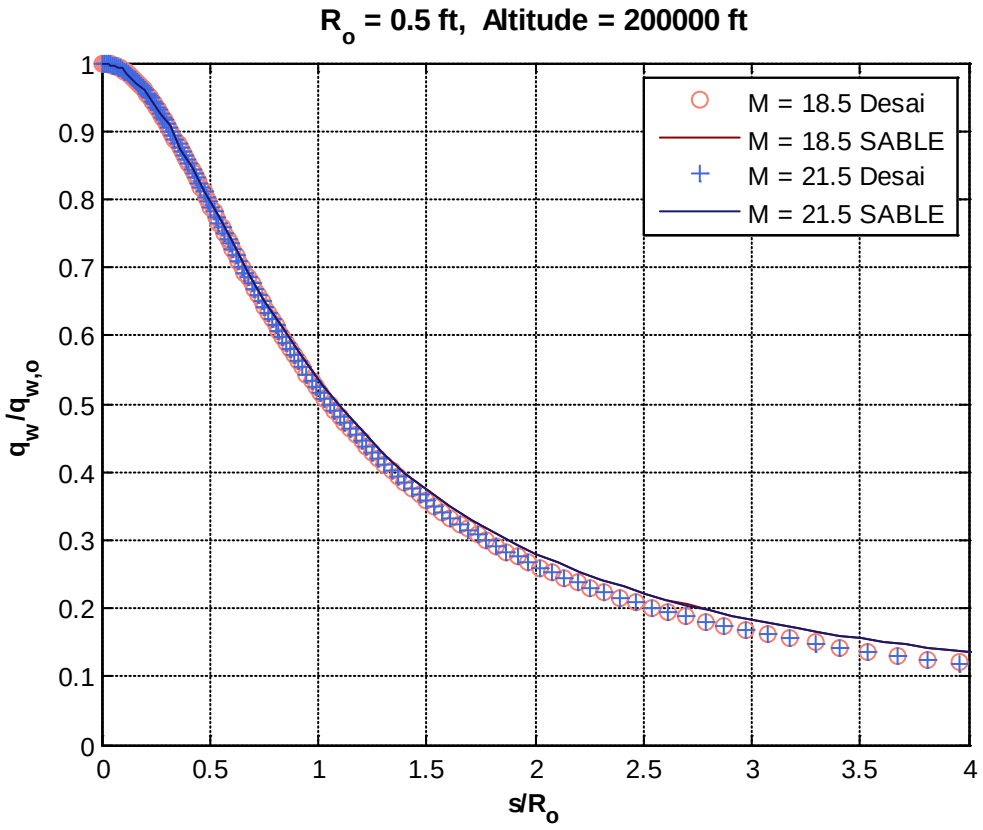

Figure C.2 - Desai vs. SABLE Results for R_o = 0.5 ft, Alt = 200,000 ft, M = 18.5 to 21.5

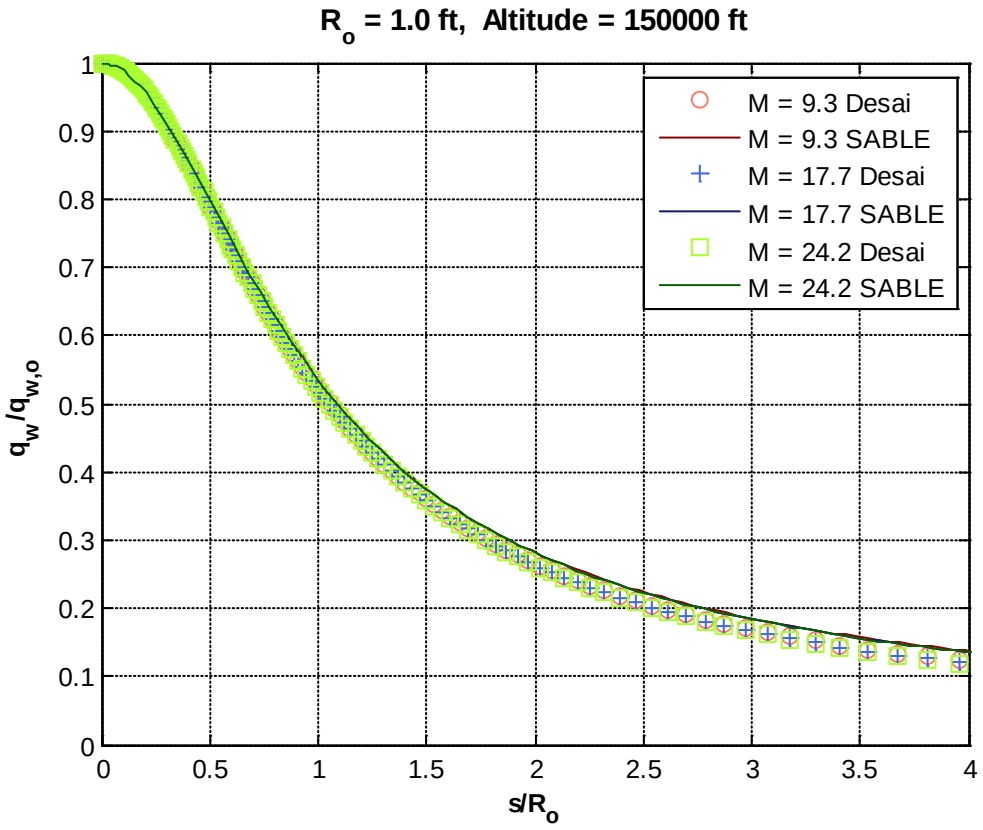

Figure C.3 - Desai vs. SABLE Results for R_o = 1.0 ft, Alt = 150,000 ft, M = 9.3 to 24.2

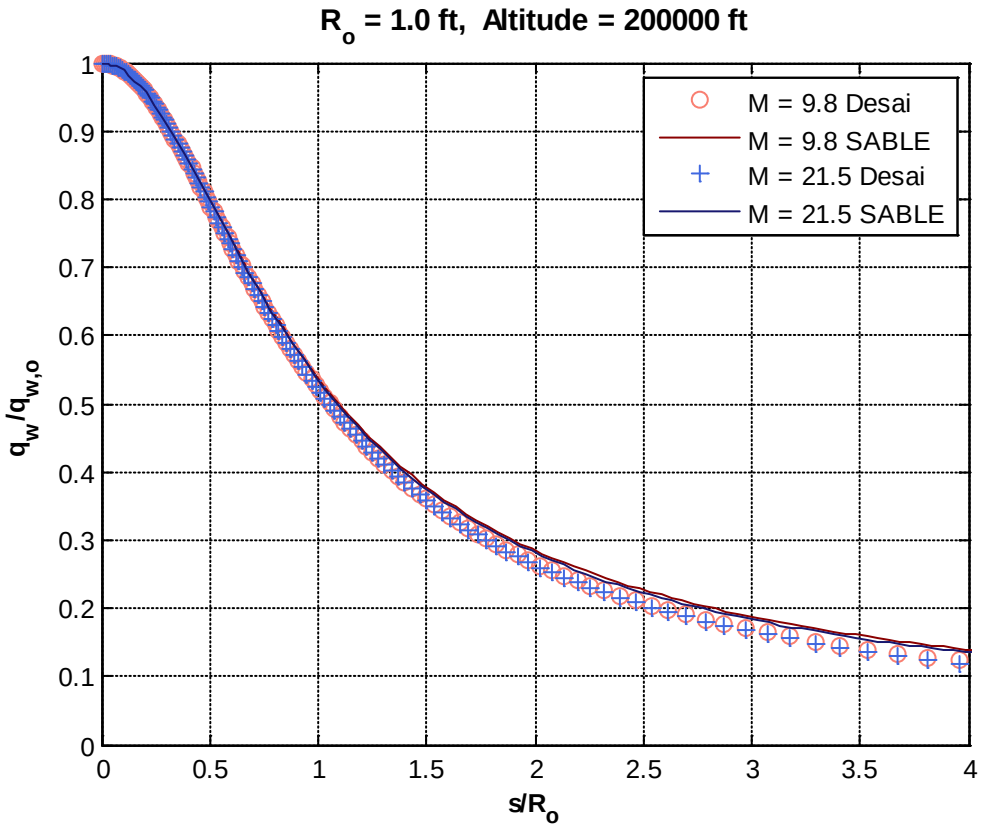

Figure C.4 - Desai vs. SABLE Results for R_o = 1.0 ft, Alt = 200,000 ft, M = 9.8 to 21.5

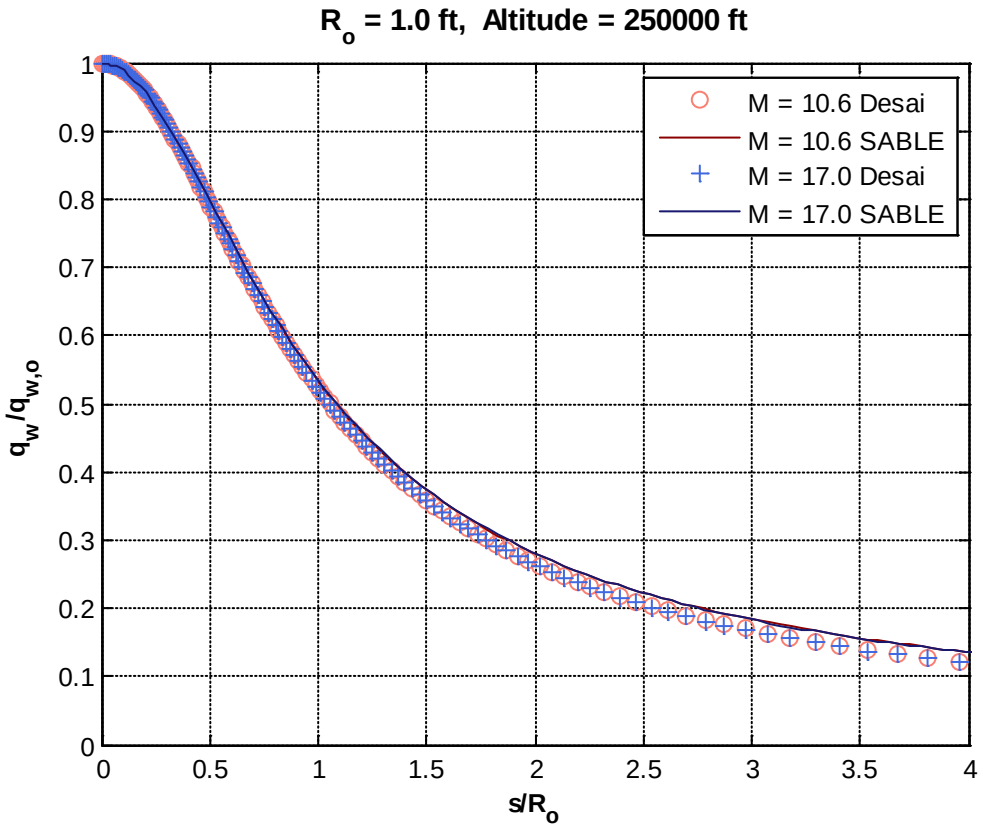

Figure C.5 - Desai vs. SABLE Results for R_o = 1.0 ft, Alt = 250,000 ft, M = 10.6 to 17.0

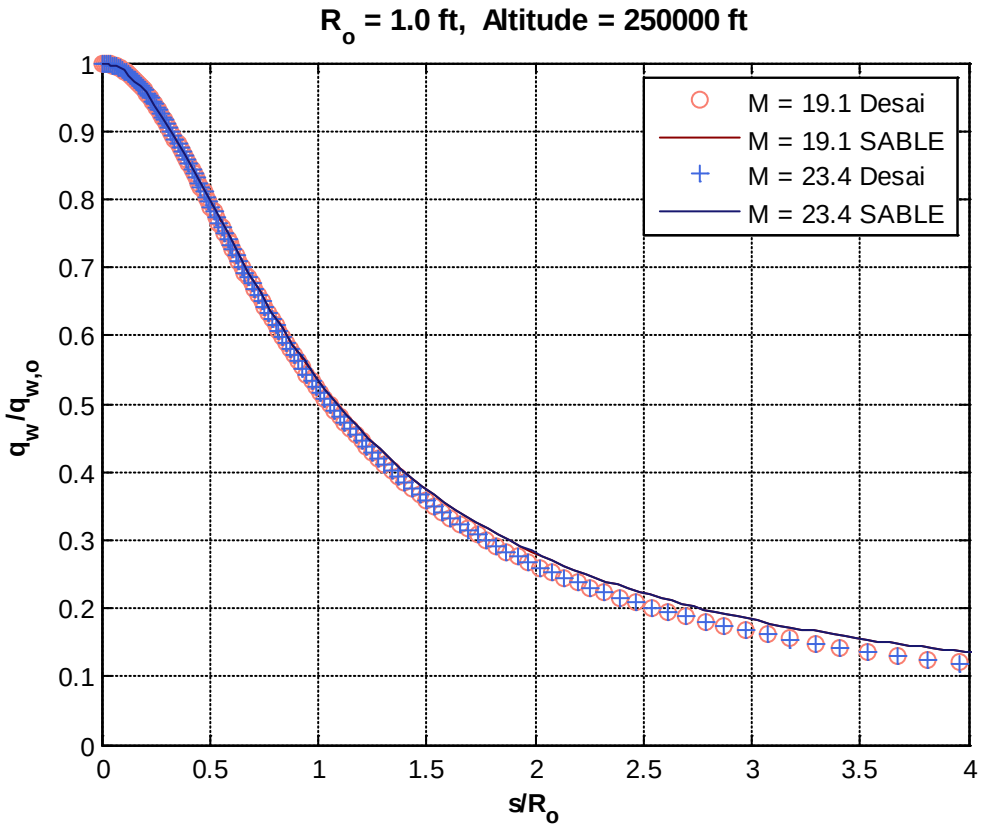

Figure C.6 - Desai vs. SABLE Results for R_o = 1.0 ft, Alt = 250,000 ft, M = 19.1 to 23.4

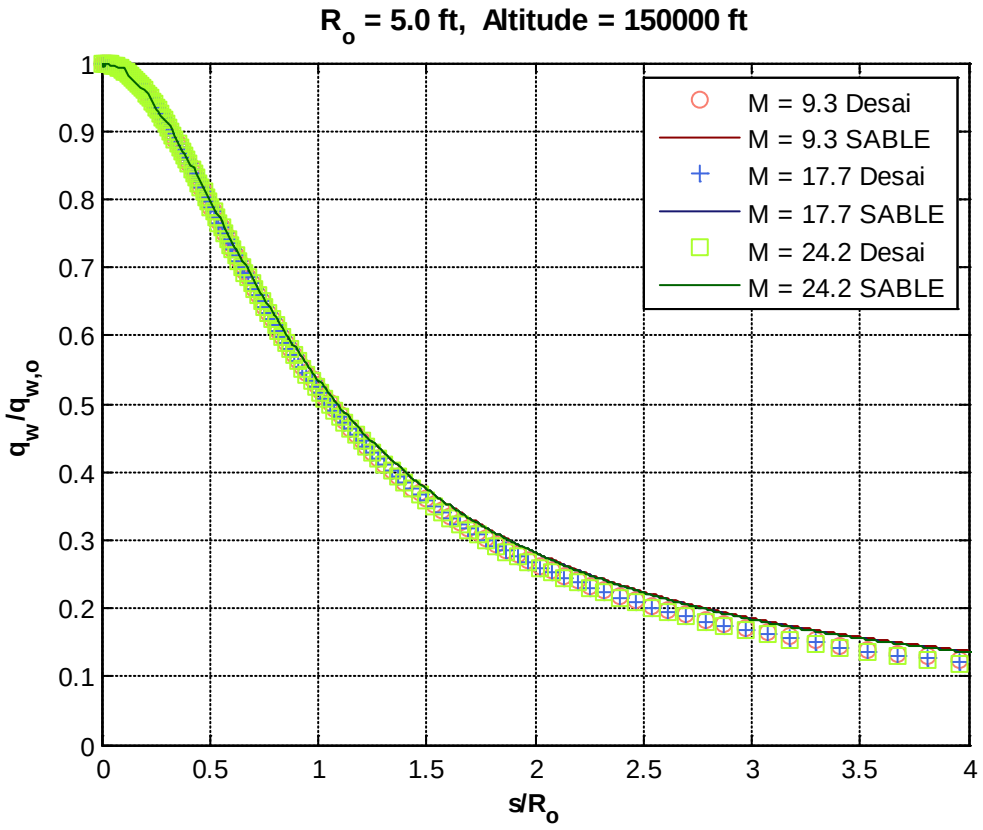

Figure C.7 - Desai vs. SABLE Results for R_o = 5.0 ft, Alt = 150,000 ft, M = 9.3 to 24.2

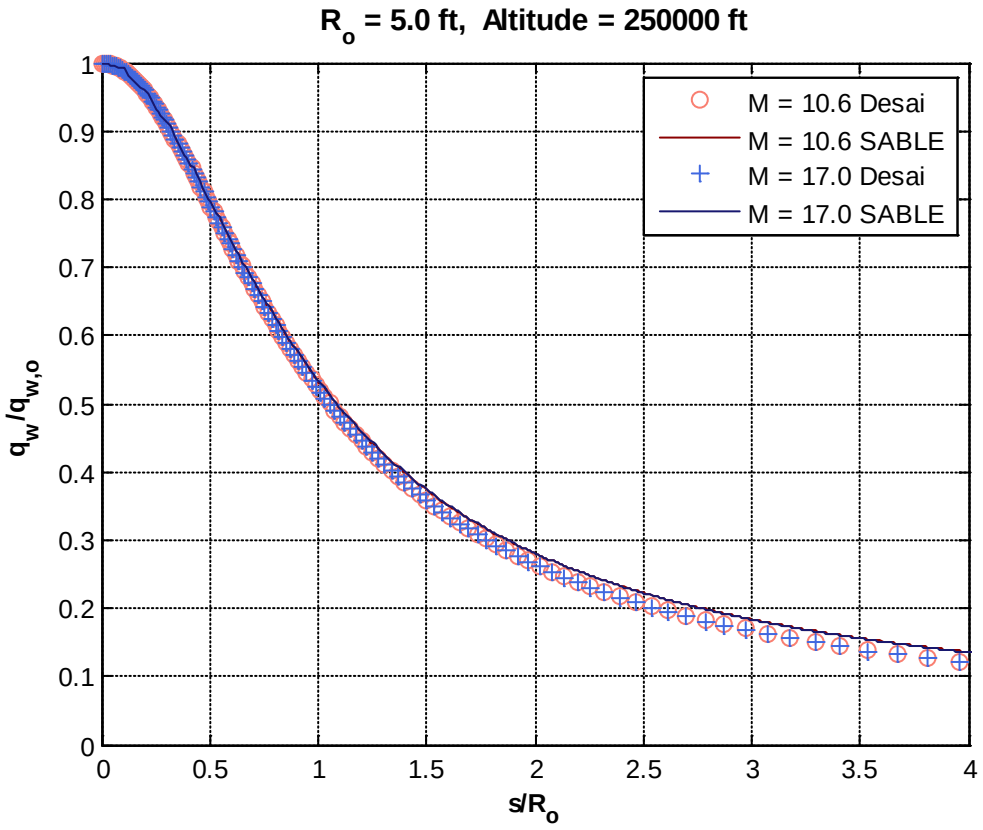

Figure C.8 - Desai vs. SABLE Results for R_o = 5.0 ft, Alt = 250,000 ft, M = 10.6 to 17.0

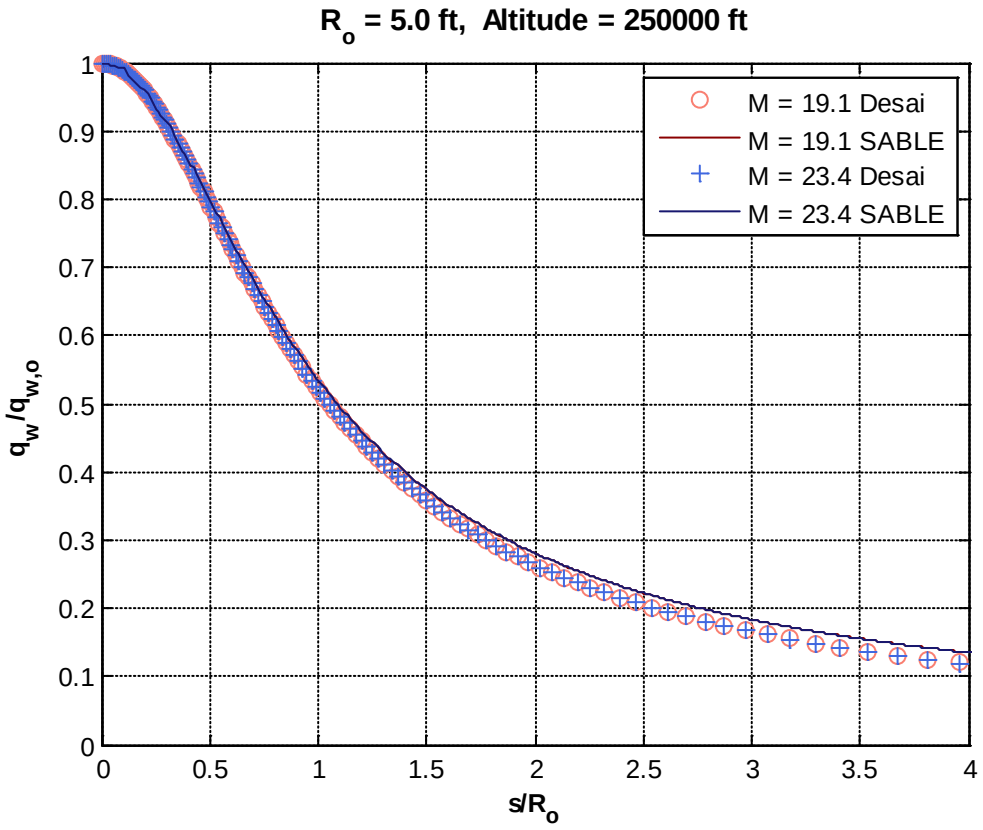

Figure C.9 - Desai vs. SABLE Results for R_o = 5.0 ft, Alt = 250,000 ft, M = 19.1 to 23.4

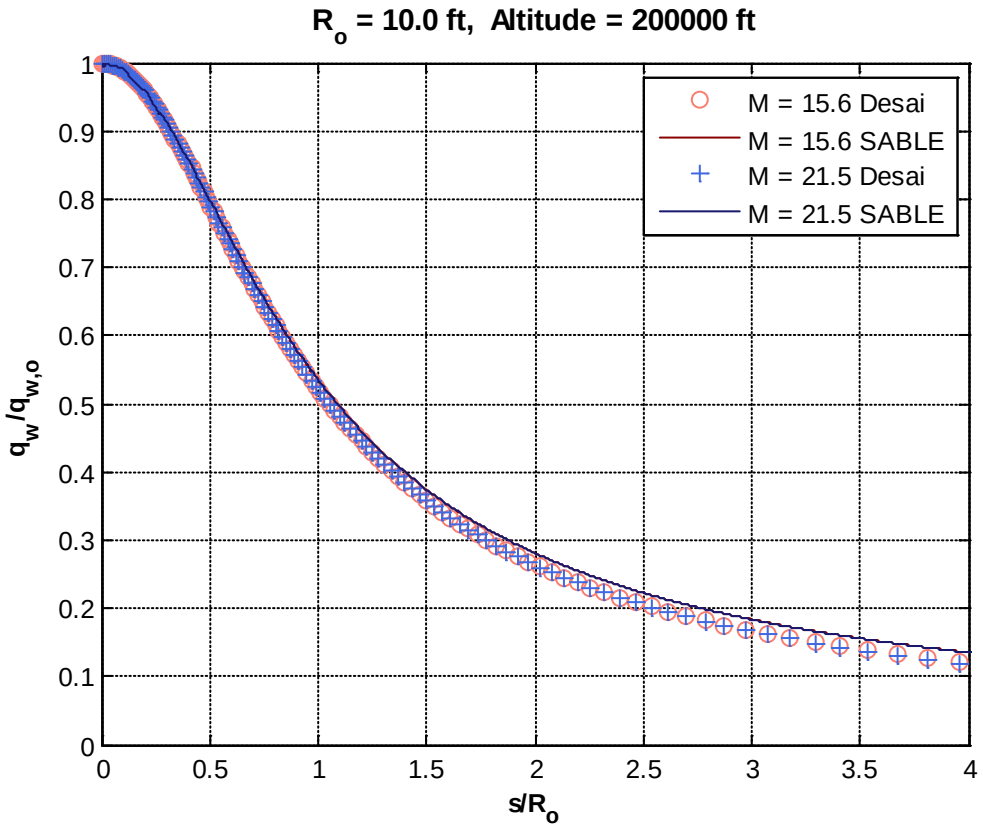

Figure C.10 - Desai vs. SABLE Results for R_o = 10.0 ft, Alt = 200,000 ft, M = 15.6 to 21.5

Appendix D – Comparison of Correlations and Curve Fit Results

Table D.1 - Maximum Error Generated Using 4th Order Polynomial Curve Fit

Test Case No.	|Max % Error|		
	Desai Compared with SABLE	4^{th} Order Curve Fit Compared with SABLE	Difference in Desai and 4^{th} Order Curve Fit Results
1	11.3	12.9	-1.6
2	11.9	12.1	-0.2
3	12.1	11.8	0.3
4	12.2	11.7	0.5
5	12.3	11.5	0.8
6	12.4	11.5	0.9
7	11.2	12.6	-1.4
8	11.9	11.9	0.0
9	12.2	11.6	0.6
10	12.3	11.5	0.8
11	11.9	11.4	0.5
12	12.1	11.4	0.7
13	12.3	11.3	1.0
14	11.3	13.0	-1.7
15	12.2	11.7	0.5
16	12.4	11.5	0.9
17	12.9	14.2	-1.3
18	12.3	11.5	0.8
19	11.1	12.0	-0.9
20	11.9	11.5	0.4
21	12.1	11.4	0.7
22	12.3	11.3	1.0
23	11.4	13.0	-1.6
24	12.2	11.7	0.5

Table D.1 Continued

25	12.4	11.5	0.9
26	11.3	12.6	-1.3
27	12.0	11.7	0.3
28	12.3	11.5	0.8
29	11.1	12.0	-0.9
30	12.0	11.5	0.5
31	12.1	11.4	0.7
32	12.3	11.3	1.0
33	11.4	13.0	-1.6
34	12.2	11.7	0.5
35	12.1	11.7	0.4
36	12.3	11.5	0.8
37	12.0	11.5	0.5
38	12.3	11.4	0.9